



Politecnico di Torino

Department of Applied Science and Technology

Ph.D. in Chemical Engineering

XXV cycle

FLUID DYNAMIC MODELLING OF BUBBLE COLUMN REACTOR

PhD Student

Khurram Imran Khan

Supervisors

Prof. Marco Vanni

Prof. Daniele Marchisio

Second Referee:

Prof. Alberto Brucato

Coordinator:

Prof. Vito Specchia

DEDICATED TO

My dearest mother, the visionary lady of our family

My strong father, my first teacher and reformer

My beloved wife, for standing with me in hard toil

Contents

Abstract	iii
Acknowledgement	122
1 Introduction	1
2 CFD methods for bubble column	6
2.1 Introduction	6
2.2 Bubble Column Reactor	7
2.2.1 Fluid dynamics and flow regimes	10
2.3 CFD methods for bubble column	12
2.4 Eulerian-Eulerian: Multifluid/two-fluid model	14
2.4.1 Local instantaneous equations and jump conditions	15
2.4.2 Averaging techniques	17
2.4.3 Closure relations	21
2.4.3.1 Viscous stress	22
2.4.3.2 Interfacial interaction terms	22
2.4.3.2.1 Drag force	23
2.4.3.2.2 Transversal or lateral force (Lift)	28
2.4.3.2.3 Virtual mass force	30
2.4.3.2.4 Basset history force	31
2.4.4 Turbulence closure	31
2.4.5 Summary of model equations	34
3 Flow simulation with fixed bubble size	35
3.1 Introduction	35
3.2 Simulation setup	36
3.2.1 Computational model	36
3.2.2 Boundary conditions	39
3.3 Gas flow rate 48 L/h	39
3.3.1 Grid dependencies	39
3.3.2 Results and discussion	41
3.3.2.1 Calculation of plume oscillation Periods	43
3.3.2.2 Liquid axial velocity and gas holdup	45
3.4 Gas flow rate 260 L/h	48

3.4.1	Results and discussion	49
3.4.1.1	Calculation of plume oscillation Periods	53
3.4.1.2	Liquid axial velocity and gas holdup	54
4	Population Balance	56
4.1	Introduction	56
4.2	Population balance equations	56
4.3	Bubble breakage and coalescence	58
4.3.1	Birth and death due to breakage	59
4.3.2	Birth and death due to coalescence	60
4.3.3	Gas Liquid system	61
4.3.3.1	Discontinuous events modelling (Coalescence and breakage)	62
4.3.3.2	Breakage frequency and daughter distribution function	63
4.3.3.3	Coalescence kernel	65
4.4	Solution methods	67
4.4.1	Quadrature method of moments	70
5	Flow Simulation with Coalescence and Breakage	73
5.1	Introduction	73
5.2	QMOM without breakage and coalescence models	74
5.2.1	Results and discussion	77
5.3	QMOM with breakage and coalescence models	81
5.3.1	Results and discussion	83
6	Mass Transfer and Chemical Reaction in Bubble Column Reactor	87
6.1	Introduction	87
6.2	Governing equations and reactions	90
6.3	Applicability of the physical data	93
6.3.1	Results and discussion	94
6.4	CFD simulation with mass transfer and chemical reaction	97
6.4.1	Simulation setup	98
6.4.1	Results and discussion	99
7	Conclusions	106
	References	109

Abstract

Numerical simulations of rectangular shape bubble column reactors (BCR) are validated starting from preliminary simulations aimed at identifying proper simulation parameters for a given system and resulting up to the numerical simulation with mass transfer and chemical reactions. The transient, three dimensional simulations are carried out using FLUENT software and the results obtained for a system with low gas flow rate (48 L/h) indicated that we need enough fine mesh grid and appropriate closure of interfacial forces to predict reliably plume oscillation period, liquid axial velocity and gas holdup profiles. In case of high flow rate (260 L/h), we compared the results for the effect of different interfacial closure forces and change in inlet boundary condition for gas volume fraction. There is no change in hydrodynamic results when there is change in gas volume fraction at inlet boundary condition. The effect of virtual mass interfacial force on the simulation results is also negligible. However, the major effects of applying lift force on results of plume oscillation period, liquid axial velocity and gas holdup is predicted. For comparable simulation results to experimental data, it is suggested that requirement of enough fine grids and appropriate correlations for interfacial forces, especially the combination of drag and lift forces is necessary.

To study the bubble size distribution in BCR the numerical simulations are carried out with QMOM population balance technique for air-water fluid system. After finalization of the generic moment boundary conditions with simulations with PBM using QMOM without breakage and coalescence phenomena, then we simulated the system with breakage and coalescence and eventually, the simulation results are compared with experimental and simulation data taken from the scientific literature. For better hydrodynamics results of BCR as compared to experimental results, the interfacial lift force with combination of drag force is predicted for QMOM. The discretization scheme for gas volume fraction and moments of first order upwind provided the expected results of bubble size distribution. The simulation result of QMOM with breakage and coalescence models were also in good agreement with hydrodynamics experimental results and simulation results of class methods and DQMOM for bubble size distribution results.

The modelling of chemical absorption of pure CO₂ gas in caustic solution is carried out in a rectangular BCR with identical simulation parameters settings of previous work. For applicability of available kinetic and physical data we developed concentration differential equations to estimate the species molar concentration with respect to time in MATLAB code. The obtained profiles of evaluation of concentration and pH were in similar fashion as compared to available CFD simulated concentration and pH profiles at a point in the bubble column with respect to time. CFD simulation taking into account the mass transfer and chemical reaction, the E-E approach is used with assumption of uniform bubble size for modelling of chemisorption of the CO₂ gas bubbles into NaOH aqueous solution. The adopted models successfully predicted the hydrodynamics results and are in good agreement with experimental and simulation results, however, reaction processes results are not as per expectation and further improvement in adopted simulation methods is required for better results.

Chapter 1

Introduction

Multiphase flow processes, particularly, bubbles and drops dispersed in some continuous phase such as liquid, are the common examples of chemical, petroleum, biochemical, pharmaceutical and food industries. Bubble column reactors (BCR) and stirred tank reactors (STR) are the traditional reactors opted for multiphase flow processes. The BCR is preferred due to easiness in operation with no moving mechanical parts, low operation and maintenance cost, good mass and heat transfer characteristics and high durability of catalyst. The disadvantage of the BCR or multiphase reactors is of their non-uniformity, for example: mixing, bubble or drop size distribution and holdups have large local diversities. The major applications of BCR are given in Table 1.1(Deckwer and Field, 1992, Fregapane et al., 1999, Ranade, 2002, Nigar et al., 2005).

The bubble column reactors have vertical cylindrical shape in which gas is sparged in bottom of column and is distributed in liquid in the form of bubble while moving upward. The motion of the liquid can be co-current or counter current to the upward gas bubbles. The back-mixing of liquid phase is the result of buoyancy driven recirculation in BCR and is sometimes considered the disadvantages of operation. In order to overcome this limitation, modifications to the design of internals of BCR are applied in the form of baffles (Deckwer and Field, 1992). The consumption of gas in the liquid phase depends on the rate of mass transfer and chemical reaction. Multiphase flows in the BCR may be classified in different flow regimes, bubbly flow, churn turbulent flow and slug flow etc. Based on the flow regimes different modelling approaches are needed. Another characteristic of multiphase flows is the degree of phase coupling, which is described by dispersed phase volume fraction in the system and Stokes number. The degree of coupling can be one-way, two- or four-way couplings. Regardless of many applications and published literature, the BCR designing and scale-up is not precise due to incomplete understandings of the complex hydrodynamics.

In case of gas-liquid systems, the interaction between phases is composed of hydrodynamics, mass transfer and chemical reaction and making it a complex physical system to be numerically solved. During the last three decades, computational fluid dynamics (CFD) developed as a numerical solution tool for the scale-up and design of multiphase reactors (Stewart and Wendroff, 1984; Crowe et al., 1996; Kuipers and van Swaaij, 1997; Jakobsen, 2008). However, applicable generalized CFD codes are not available due to inherent complexity of multiphase systems.

Table 1.1 Major Applications of the Bubble Column Reactor (Ranade, 2002)

Process	Reactants	Main Products
Oxidation	ethylene, cumene, butane, toluene, xylene, ethylbenzene, acetaldehyde, cyclohexane, cyclohexene, n-paraffins, glucose	vinyl acetate, phenol, acetone, methyl ethyl ketone, benzoic acid, phthalic acid, acetophenone, acetic acid, acetic anhydride, cyclohexanol and cyclohexanone, adipic acid, sec-alcohols, glutonic acid
Chlorination	aliphatic hydrocarbons, aromatic hydrocarbons	chloroparaffins, chlorinated aromatics
Alkylation	ethanol, propylene, benzene, toluene	ethyle benzene, cumene, iso-butyl benzene
Hydroformylation	Olefins	aldehydes, alcohols
Carbonylations	methanol, ethanol	acetic acid, acitic anhydride, propionic acid
Hydrogenation	benzene, adipic acid dinitrile, nitroaromatics, glucose, ammonium nitrate, unsaturated fatty acids	cyclohexane, hexamethylene diamine, amines, sorbitol, hydroxyl amines
Gas to Liquid Fuels	F-T synthesis, methanol from syngas	liquid fuels
Coal Liquification	coal	liquid fuels
Desulfurization	petroleum fractions	desulfurize fractions
Aerobic Bio-Chemical Processes	Molasses	ethanol

There are mainly three CFD approaches to model the multiphase flows; the front tracking models also referred, interface-tracking model (Volume of fluid) (Hirt and Nichols, 1981), Euler-Lagrange (E-L) model (discrete bubble model) and Euler-Euler(E-E) model (two fluid model) (Sokolichin and Eigenberger, 1994) (for review of these approaches, van Wachem and Almstedt, 2003). The interface-tracking model describes the evolution of interfaces between the phases with good approximation but can model few numbers of bubbles

simultaneously due to high computational cost. In the E-L approach, individual bubbles are modelled by tracking their motions in continuous phase. By using the E-L approach, modelling cost can be high if the volume fraction of dispersed phase is higher than ($>10\%$). The E-E approach is suitable for high fraction of dispersed phase or for industrial scale systems. In this approach, both gas and liquid phases are modelled with the assumption of interpenetrating continuum fluids. The drawback of E-E models is that they need complex interfacial closure relations to manipulate the interaction between the phases. The interphase momentum transfers for gas-liquid systems is composed of different forces, drag, added mass or virtual force, history or Basset force, effect of turbulent fluctuation and lift forces. Many studies have been carried out to model the interfacial exchange terms (Biesheuvel and Spoelstra, 1989; Drew and Lahey, 1987; Tomiyama et al., 1998) for gas-liquid systems. Turbulence modelling plays an important role in the simulation of the multiphase flow: Large Eddy Simulation (LES) and Direct Numerical Simulation (DNS) were successfully implemented to bubbly flows (Derksen and Van den Akker, 1999; Hartmann et al., 2004), but their computational cost is high. For this reason, the notable Reynolds-Averaged Navier-Stokes equation (RANS) approach has been used for gas-liquid systems (Lopez de Bertodano and Saif, 1997), and it is well established for the simulation of industrial scale reactors, (Zhang et al., 2006).

The dispersed phase experiences changes in the system due to coalescence and breakage that greatly affect the interfacial area and also the mass transfer and reaction rates. The prediction of bubble size distribution and bubble population may be formed by of population balance equations (PBE) generalized by Ramkrishna (2000). With the PBE, it is possible to formulate the change in the disperse phase in physical space and also in the space produced by the properties of the population normally called as internal coordinates. If the population of bubbles is described by only one internal property/coordinate, for example length of the particle, then the PBE is called monovariate, with two internal coordinates, it is called bivariate, and with more than two, it is called multivariate. However, PBE model is a form of partial integral-differential equations, and it is complicated to calculate their solutions when more than one bubble properties are studied or spatial inhomogeneities are proposed.

The solution methods for PBE can be classified based on the solution strategy adopted; mainly, there are three groups of methods for solving the PBE: classes or sectional, Monte Carlo and moment-based methods. In Classes Methods

(CM), the PBE is solved by discretizing internal coordinates space: these were initially developed for the solution of monovariate cases, in which the state of the population is characterized by one property or variable (Kostoglou and Karabelas, 1994; Vanni, 2000) and were recently extended to multivariate cases, in which two or more variables are needed to describe the disperse system (Kumar et al., 2008; Nandanwar and Kumar, 2008). The main drawback of these methods is the high computational costs to get accurate results when the inhomogeneities in the physical space are taken into account. Finite Volume Methods (Gunawan et al., 2004) and Finite Element Methods (Godin et al., 1999) belong to the group of CM and hence they, too, have the same limitations in application to the realistic inhomogeneous systems.

Monte Carlo Methods (MCM) are based on the solution of stochastic differential equations, which are able to reproduce a finite number of artificial realizations of the system (Zhao et al., 2007). However, the computational cost is also high for realistic systems with these methods, therefore; these methods are usually used for validation of simplified cases (Zucca et al., 2007).

The Method of Moments (MOM) was first formulated and applied to particulate systems by Hulburt and Katz (1964). In MOM the PBE are represented in terms of transport equations of the moments of the bubble distribution. For realistic processes, it is not always possible to write the governing equations in terms of the moments themselves, many closures were proposed in order to overcome closure problem. In order to overcome the closure problem, a different approach for computing the moment is to approximate the integrals using the numerical quadrature scheme, the quadrature methods of moments (QMOM) as suggested by McGraw (1997); Marchisio and Fox (2005) extended the method by developing the direct QMOM where the quadrature abscissa and weights are formulated as transport equations; they are solved directly using matrix operation. Methods of moments (MOM) have low computational costs as compared to others numerical methods for solving PBE and can be coupled with CFD for prediction of industrial scale systems with economical computational costs (Marchisio et al., 2003a; Zucca et al., 2007; Buffo et al., 2013).

Based on above discussion, the present dissertation is organized as follows:

- A. In Chapter 2, an overview of bubble column reactor, the probable flow regimes and different CFD methods are discussed. Moreover, the

- generalized, two fluid model (E-E) is developed for specific gas liquid systems including interfacial closure relations and turbulence treatment.
- B. In Chapter 3, the rectangular shape BCR is simulated with fixed bubble size for two different flow rates. The effect of interfacial forces on the simulation results are compared with available experimental data and finalized the geometry and simulation setup for further work.
- C. In Chapter 4, the generalized population balance mathematical framework including the bubble coalescence and breakage are discussed for gas-liquid systems. The method of moment, QMOM is presented for numerical simulation of bubble column in Chapter 5. Preliminary, the stability and accuracy of QOMOM was established and then applied with breakage and coalescence in second part.
- D. In Chapter 6, the mass transfer and chemical reaction is modelled in a rectangular bubble column reactor with example of chemisorption of pure CO_2 gas in caustic solution (aqueous NaOH).

CHAPTER 2

CFD METHODS FOR BUBBLE COLUMNS

2.1 Introduction

The Bubble column reactor (BCR) is a type of multiphase flow equipment and has wide range of applications in chemical, petroleum, bio-chemical and coal liquefaction processes. BCR has advantages as compared to others multiphase reactors in terms of easiness in operations and maintenance, has no mechanical parts, good mass and heat transfer between reactants (Deckwer and Field, 1992). The parameters that define the performance of the BCR are mainly gas holdup, liquid velocity profiles, bubble size distribution and inter-phase turbulence. Experimental studies and numerical simulations both are used to study the complex mechanism of phase interaction and mixing of phases, (Krishna and Ellenberger, 1996). Flow regimes in BCR are classified as the topology of flow: dispersed flow, separated flow and mixed flow (Ishii, 1975). In gas-liquid or gas-liquid-solid systems of BCR, normally, gas phase or bubble and solid particles are taken as dispersed and liquid phase containing this dispersed phase as continuous phase (Ranade, 2002).

Different CFD approaches for BCR have been studied during last fifteen years for different gas-liquid systems, mostly the Euler-Euler (E-E) (e.g. used by Dhotre and Joshi, 2004; Joshi, 2001; Mudde and Simonin, 1999; Pflieger et al., 1999; Sokolichin et al.; 2004, Tabib et al.; 2008) and Euler-Lagrange (E-L) approaches (Buwa et al., 2006; Delnoij et al., 1995; , Devanathan et al., 1995; Lain et al., 1999; Lapin and Lübbert, 1994). In E-L approach, the motion of the continuous phase is numerically modelled using Euler framework and the motion of the each dispersed phase bubble or particle is explicitly modelled in Lagrange framework. This approach is suitable for modelling dispersed phase with small volume fraction (<10%) as computational cost increases within increase of number of particles. In E-E approach, both continuous and dispersed phases are modelled in Euler framework with the assumption of interpenetrating continuum fluids. The E-E approach is preferable for modelling of dense

volume fraction of dispersed phase. While 2-dimensional (2-D) E-E simulations are often unable to capture the relevant features of the flow, 3-dimensional (3-D) simulations give good prediction when compared to experimental results (Bertola et al., 2002; Krishna and Van Baten, 2001; Mudde and Simonin, 1999; Pflieger et al., 1999; Sokolichin and Eigenberger, 1999). In the present work, we will numerically solve the BCR with CFD 3-D E-E approach and will compare the simulations with available experimental results in literature.

In CFD simulations, the first step is understanding the objectives of flow model, and second step is defining the numerical model to meet the defined objectives of flow model (Ranade, 2002). It is, however, necessary to get an idea about principles of numerical modelling of single phase flow systems before going on to model the complex one. In this chapter, we will discuss the modelling of multiphase and turbulent flow processes.

The chapter is divided in four sections: in first section we will discuss about bubble column basic design and scale up, flow regimes and operations. In remaining sections we will discuss governing equations, interfacial forces, and turbulence models for gas liquid systems.

2.2 Bubble Column Reactors

Bubble column reactors (BCR) are the type of multiphase reactors in which gas, named as dispersed phase/discontinuous phase, is in the form of bubbles in the continuous phase, the liquid or slurry (liquid + solid). Generally the BCR have vertical cylindrical shape in which gas is sparged in bottom of column. The schematic general BCR with basic mechanical names and their locations is shown in Figure 2.1. The net flow rate of liquid/slurry in the column is operated with zero velocity (stagnant) in batch operations, whereas in continuous operations its velocity is lower than the superficial gas velocity by an order of magnitude at least (Pino et al., 1992). The motion of the liquid can be co-current or counter current to the upward gas bubbles. The different types and mode of operation of BCR are presented in Figure 2.2.

In the simple case of BCR with no internals, the gas enters in the form of bubbles from the bottom of column through sparger/distributor and rises in the liquid up to the liquid level and then escaped from available free surface or by using phase separators when gas flow rate is high. The consumption of gas in the liquid phase depends on the rate of mass transfer and chemical reaction.

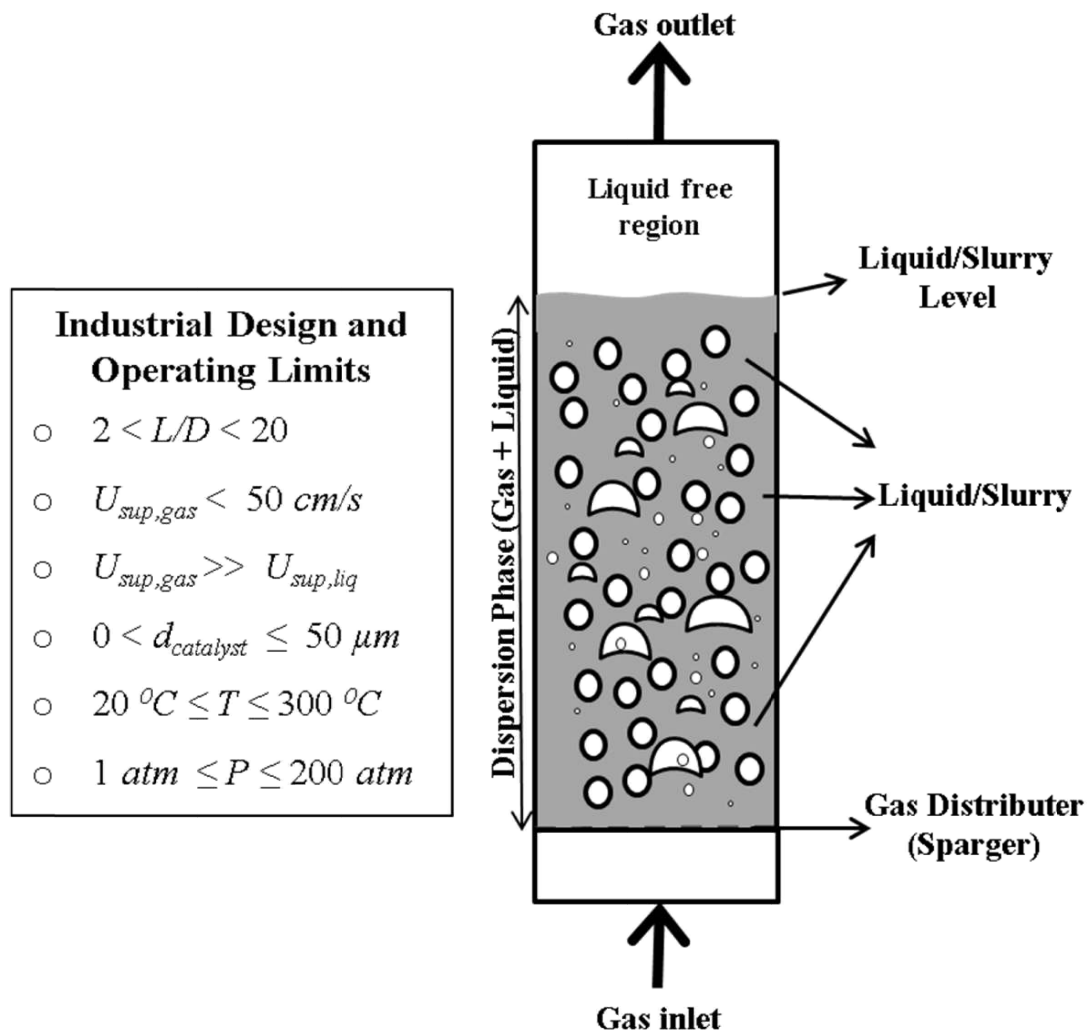


Figure 2.1 The schematic diagram of simple bubble column reactor with no internals and names of some basic parts.

The function of the sparger is to disperse the gas in the form of small bubbles and distribute uniformly in the column to create a homogeneous flow regime (Section 2.2.1). Spargers can be static or dynamic. The examples of static gas sparger are; dip tubes, perforated plates, porous plates, and perforated rings. The dynamic gas spargers are two phase jet nozzle, ejector, and venture nozzle

which use the liquid jet's power to disperse gas.

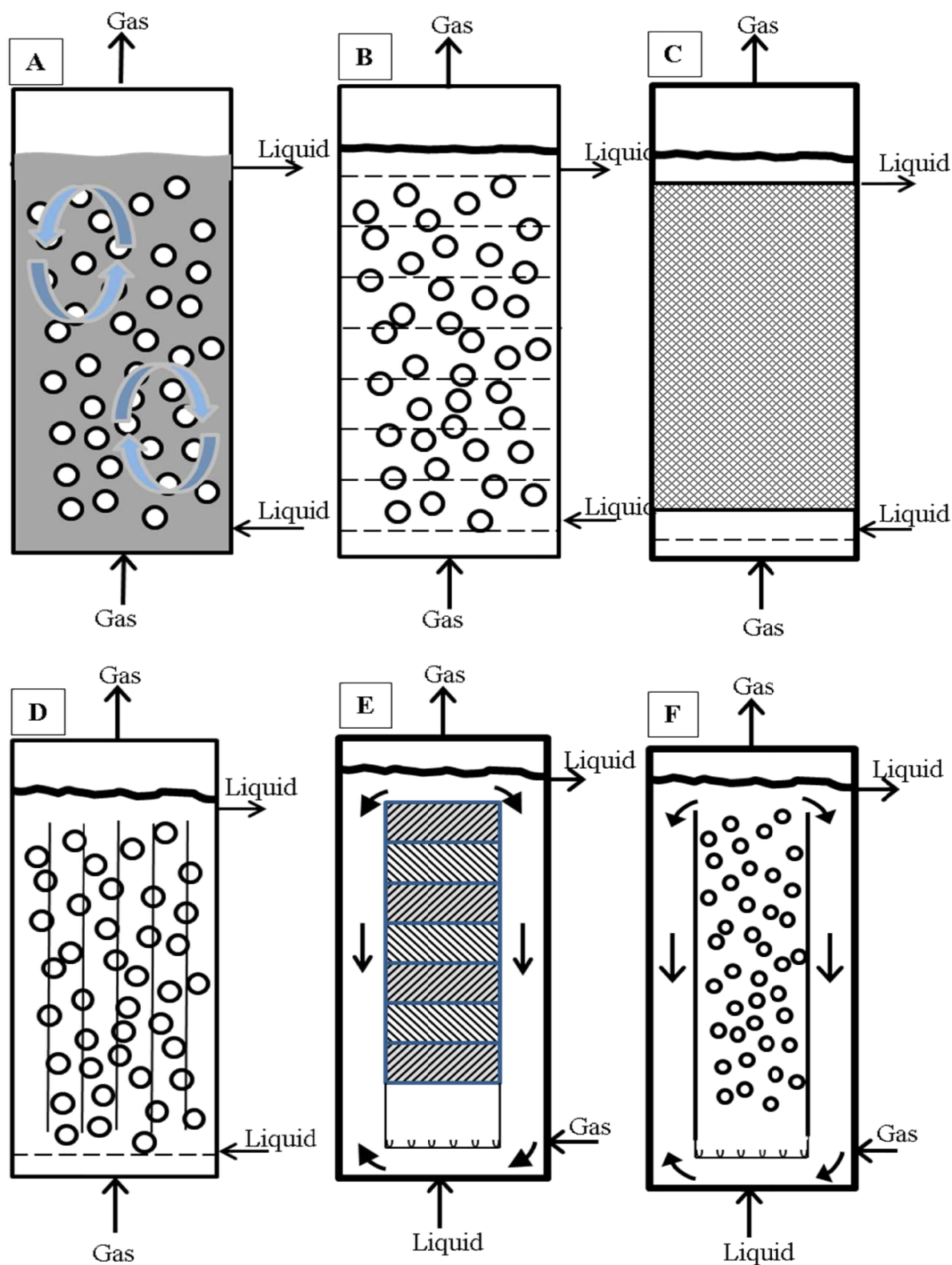


Figure 2.2 Types of bubble column reactor; A) Simple bubble column; B) Cascade bubble column with sieve trays; C) Packed bubble column; D) Multishaft bubble column; E) Bubble column with static mixers; F) Airlift loop reactor. (Deen et al., 2010).

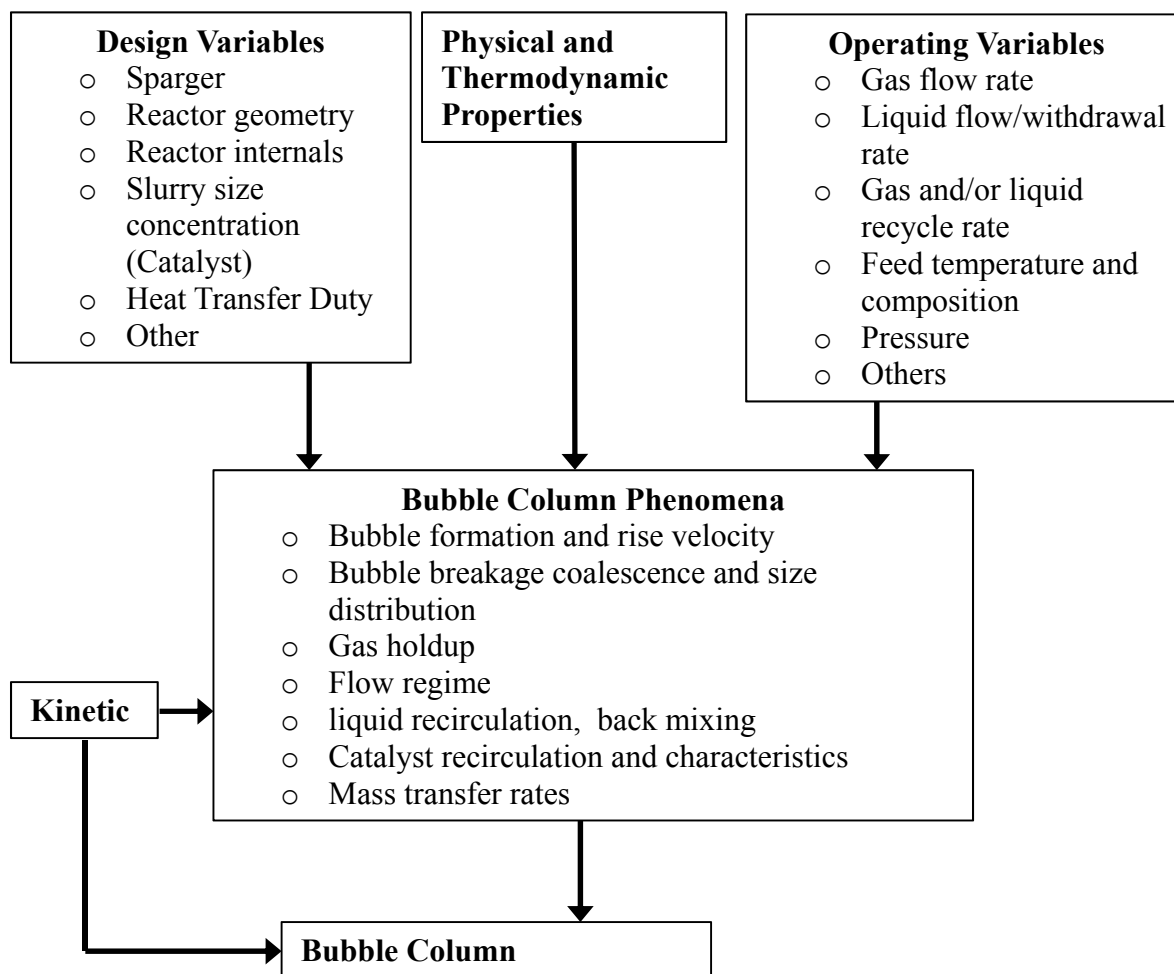


Figure 2.3 Variables affecting BCR phenomena and performance (Chen, 2004)

The internals of bubble column are the baffles in the column for preventing liquid back mixing that is also one of the disadvantages of BCR and heat exchangers for heating/cooling in case of highly exothermic or endothermic reactions. Different factors affecting the performance of the BCR are shown in Figure 2.3.

2.2.1 Fluid Dynamics and Flow Regimes

The operation and performance of BCR mainly depend on its fluid dynamics behaviour. Most studies suggested that the parameters to obtain the good performance we need to have knowledge of the flow regimes in the column (Shaikh and Al-Dahhan, 2007). Flow regime classification is characterized by the superficial gas velocity and column diameter. Normally, the flow regimes are classified in three groups; homogeneous (bubbly), heterogeneous (churn-turbulent) and slug flow regimes (Hyndman et al., 1997). The types of flow regimes in BCR and their maps are shown in Figure (2.4).

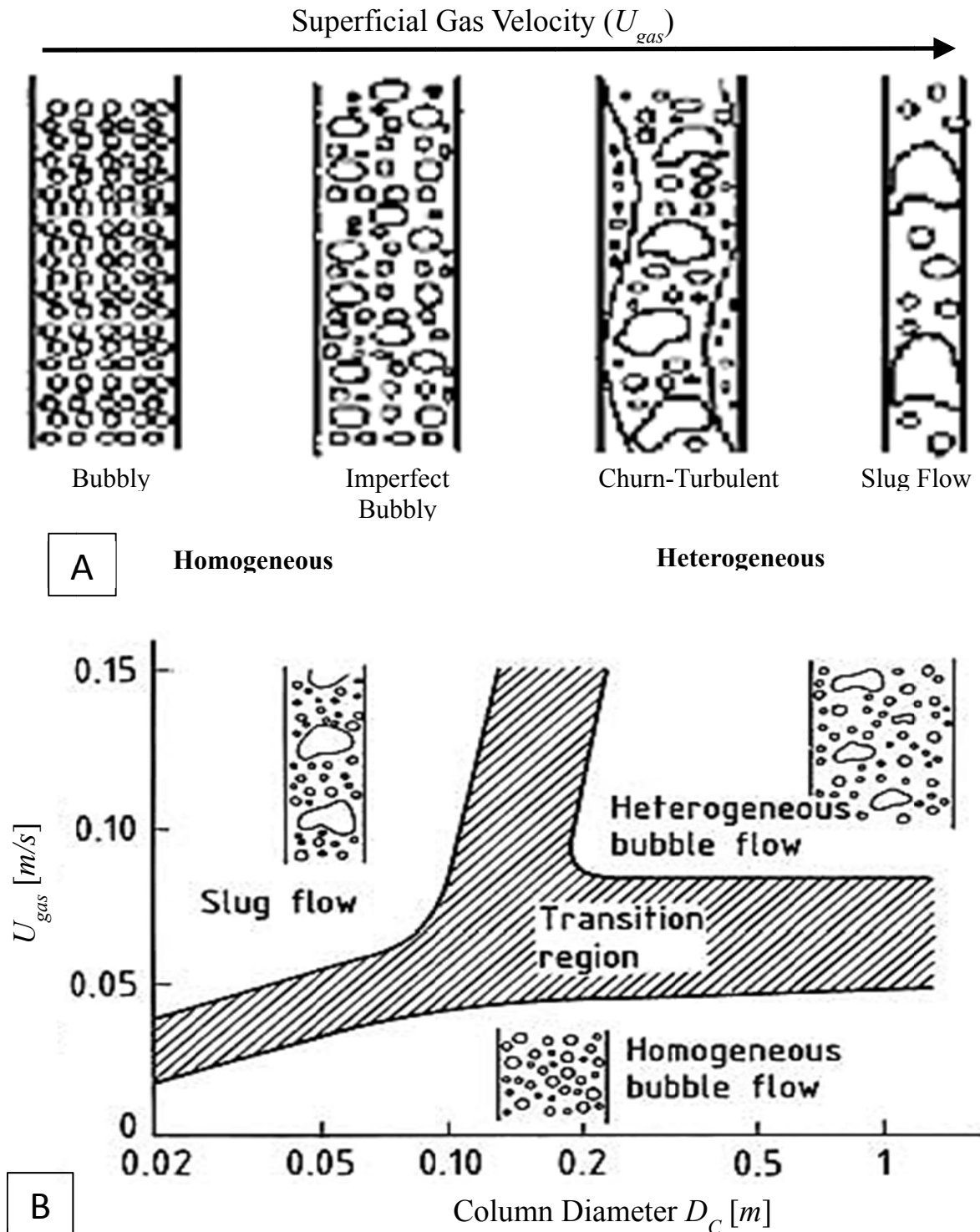


Figure 2.4 Flow Regime Classifications: A) Types of flow regimes as a function of superficial gas velocity (Bouaifi et al., 2001); B) Flow regime map as a function of superficial gas velocity and diameter of column (Shah et al., 1982).

The homogeneous flow regime or bubbly is obtained at low superficial gas velocity ($U_{gas} < 5 \text{ cm/s}$) depending on the dispersed system and sparger design (Thorat and Joshi, 2004). In this regime, the size of the bubbles is almost uniform and bubble rise velocity is also uniform (Schumpe and Grund, 1986).

With increase of the superficial gas velocity, the coalescence phenomena starts and uniformity of bubble size start to vanish. In heterogeneous flow regime, also called churn-turbulent. The size of bubbles increases due to coalescence and they travel upward with larger rise velocity. In this regime, the average bubble size is function of coalescence and breakage phenomena. The churn-turbulent flow regime is frequently observed in industrial scale columns with large bubble diameters (Hyndman et al., 1997), which have liquid circulation in centre portion in upward motion and downward near wall. The slug flow regime is observed in laboratory scales columns with small diameters and at high gas flow rates. This regime is observed in column with diameter less than 15 cm (Hills, 1976, Miller, 1980).

2.3 CFD Methods for Bubble Column

There are many computational fluid dynamics methods to study the dispersed system of BCR. They range from direct numerical simulations (DNS) to continuum based called averaged methods. The DNS is model free and represents the whole physics of the flow system. For this, special algorithms are required to trace the fluid interfaces between continuous and particle with very fine mesh grid to grab all time and length scales. Example of DNS family is volume of fluid (VOF) methods (Hirt and Nichols, 1981). In VOF approach, the motion of all phases present in the system is modelled by solving local, instantaneous conservation transport equations for mass, momentum and energy with appropriate jump boundary conditions at the interface. This approach however, has limitation as with increase in the number of dispersed phase particles the computational cost also increases. Therefore, these methods are not suitable for industrial scale dispersed systems as they need high computational resources to calculate flow process around each dispersed particle.

In the averaged methods, the motion of the interface is not explicitly modelled, but indirectly modelled to spatially larger systems. These methods may be classified in two classes: Eulerian-Lagrangian (E-L) and Eulerian-Eulerian (E-E) methods. In the E-L approach, the flow field of continuous phase (carrier, i.e. liquid/slurry) is solved using averaged Navier-Stokes equation, while each bubble's motion is solved by simulating the trajectory explicitly moving in continuous phase. In the case of simulation of a system with large number of particles, the computational cost gets very high when using this approach. Normally, this approach is suitable for dispersed multiphase system, containing

the volume fraction less than 10% of dispersed phase. The common methods in this approach are particle source in cell (PSIC) (Crowe et al., 1977; Migdal and Agosta, 1967) suitable for very low volume fractions, while for higher volume fraction discrete particle methods (DPM) (Chen and Fan, 2004; Li et al., 1999; van Sint Annaland et al., 2005) may be applied.

The E-E approach models all the phases present in the multiphase system in Eulerian framework by using the interpenetrating continuum assumption. The E-E approach is suitable for multiphase system with high volume fraction of disperse phase. The representation of coupling between different phases is possible in E-E approach by defining appropriate interphase transport models (Ranade, 2002). With this approach, calculate directly the volume fraction of each phase k , α_k in any volume of space and time. In this approach, there are two important methods: multifluid/two-fluid model and the mixture model (Drew and Passman, 1999; Hjertager, 2007; Yeoh and Tu, 2009). The difference between these two models is that in multi-fluid methods, we solve the momentum balance equations for the different phases present in the system, while in the mixture model we solve the fewer equations that describe the characteristics of the mixture as a whole. We will discuss in next section the E-E approach of multifluid/two-fluid approach in detail as our present work is based on this modelling approach.

2.4 Eulerian-Eulerian: Multifluid Model/Two-Fluid Model

The scope of the present work is the numerical solution of BCR of gas-liquid system (two phases). We will model BCR with E-E approach as we have multiphase turbulence system. The E-E modelling approach is same for a multiphase system with N number of phases or two phases. We will develop a multifluid model for N phases for multiphase system and the general procedure for formulating a multifluid model is shown in Figure 2.5. The general idea for formulating the multifluid model is to first develop the integral balance equations for mass and momentum (Our system is assumed to be isothermal so we are ignoring the energy balance equation in this and coming sections) for a control volume containing the phases. In second step, we will reduce these balances to two types of equations;

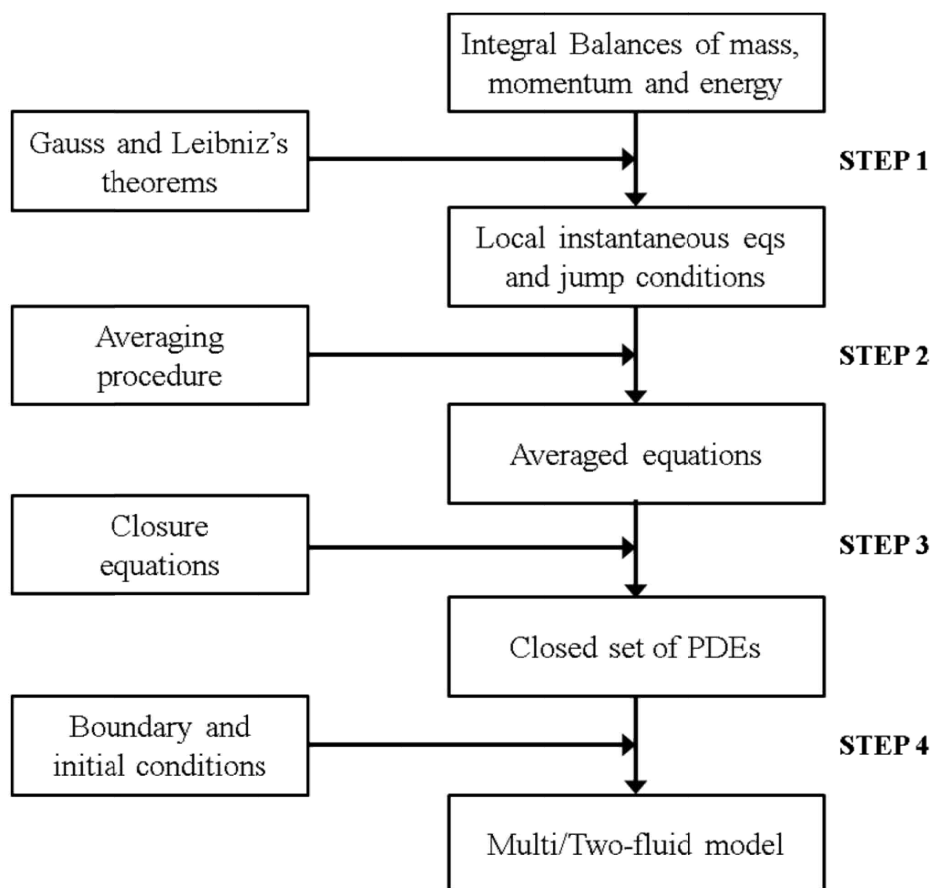


Figure 2.5 General procedures for formulating multifluid model (Enwald et al., 1996).

one is the local instantaneous equation for every phase and the other one is the expression for local instantaneous condition jump (the interaction among the phases at interface). Due to Eulerian framework, we need to average the local instantaneous equations in a suitable way Figure 2.5.

2.4.1 Local Instantaneous Equations and Jump Conditions

Suppose a general volume fixed in space and shared among N phases, each one with phase index k . The interface $A_{I,jk}(t)$ among the phases is moving with velocity \mathbf{u}_k . When a scalar or vector variable ψ that belongs to phase k is transported through the volume, the following integral balance equation for ψ on the fixed volume may be written (Hjertager, 2007; Ishii and Mishima, 1984):

$$\underbrace{\sum_{k=1}^N \left(\frac{d}{dt} \int_{V_k(t)} \rho_k \psi_k dV \right)}_{\text{Accumulation}} = \underbrace{\sum_{k=1}^N \left(\int_{V_k(t)} \rho_k \psi_k (\mathbf{u}_k \cdot \mathbf{n}_k) dA \right) - \sum_{k=1}^N \left(\int_{V_k(t)} (\mathbf{J}_k \cdot \mathbf{n}_k) dA \right)}_{\text{Net flux}} + \underbrace{\frac{1}{2} \sum_{k=1}^N \sum_{j=1}^N (1 - \delta_{jk}) \int_{A_{I,jk}(t)} \Phi_{I,jk} dA + \sum_{k=1}^N \int_{V_k(t)} \Phi_{I,jk} dV}_{\text{Source term}}, \quad (2.1)$$

where \mathbf{n}_k is the outward direction normal unit vector, \mathbf{u}_k is the velocity of phase k , \mathbf{J}_k is the flux, Φ_k is the source term and $\Phi_{I,jk}$ is the interface source term and δ_{jk} is the Kronecker delta. Location of the interface is given by the following surface:

$$\mathbf{r}_{I,jk} = \mathbf{r}_{I,jk} (x(\zeta, \eta, t), y(\zeta, \eta, t), z(\zeta, \eta, t)) \quad (2.2)$$

The velocity of the surface point (ζ, η) is defined by:

$$\mathbf{u}_{I,jk} = \left(\frac{\partial \mathbf{r}_{I,jk}}{\partial t} \right)_{\zeta, \eta = \text{const}} \quad (2.3)$$

The left hand side of (2.1) can be rewritten into a volume and surface integral by using Leibniz theorem, the convective and diffusion terms on right hand side can be transformed into sum of volume and surface integrals by using Gauss theorem:

$$\frac{d}{dt} \int_{V_k(t)} \rho_k \psi_k dV = \int_{V_k(t)} \rho_k \psi_k dV + \sum_{j=1}^N (1 - \delta_{jk}) \int_{A_{I,jk}(t)} \rho_k \psi_k \mathbf{u}_{I,jk} \cdot \mathbf{n}_{I,jk} dA \quad (2.4)$$

$$\int_{A_k(t)} \rho_k \psi_k \mathbf{u}_{I,jk} \cdot \mathbf{n}_{I,jk} dA = \int_{V_k(t)} \nabla \cdot (\rho_k \psi_k \mathbf{u}_k) dV - \sum_{j=1}^N (1 - \delta_{jk}) \int_{A_{I,jk}(t)} \rho_k \psi_k \mathbf{u}_{I,jk} \cdot \mathbf{n}_{I,jk} dA \quad (2.5)$$

$$\int_{A_k(t)} \mathbf{J}_k \cdot \mathbf{n}_k dA = \int_{V_k(t)} \nabla \cdot \mathbf{J}_k dV - \sum_{j=1}^N (1 - \delta_{jk}) \int_{A_{I,jk}(t)} \mathbf{J}_k \cdot \mathbf{n}_{I,jk} dA \quad (2.6)$$

Equation (2.1) can be rewritten after substituting (2.4), (2.5) and (2.6), as one volume integral occupied by all phases and one surface integral which represent the jump conditions at the interface:

$$\begin{aligned} & \sum_{k=1}^N \int_{V_k(t)} \left[\frac{\partial}{\partial t} (\rho_k \psi_k) + \nabla \cdot (\rho_k \psi_k \mathbf{u}_k) + \nabla \cdot \mathbf{J}_k - \rho_k \Phi_k \right] dV \\ & - \sum_{k=1}^N \sum_{j=1}^N (1 - \delta_{jk}) \int_{A_{I,jk}} \left[(\dot{m}_{I,kj} \psi_k + \mathbf{J}_k \cdot \mathbf{n}_{kj}) + \frac{1}{2} \Phi_{I,kj} \right] = 0 \end{aligned} \quad (2.7)$$

where \dot{m}_k is the mass transfer per unit area and unit time from phase k to phase j :

$$\dot{m}_{I,kj} = \rho_k (\mathbf{u}_k - \mathbf{u}_{I,kj}) \cdot \mathbf{n}_{I,kj} \quad (2.8)$$

Equation (2.7) must be valid for any $V_k(t)$ and $A_{I,kj}(t)$, since the control volume is generic. Hence, the local instantaneous balance equation reads as:

$$\frac{\partial}{\partial t} (\rho_k \psi_k) + \nabla \cdot (\rho_k \psi_k \mathbf{u}_k) + \nabla \cdot \mathbf{J}_k - \rho_k \Phi_k = 0 \quad (2.9)$$

and the local instantaneous interfacial jump condition is:

$$\psi_k \dot{m}_{I,jk} + \psi_k \dot{m}_{I,kj} + \mathbf{J}_j \cdot \mathbf{n}_{I,jk} + \mathbf{J}_k \cdot \mathbf{n}_{I,kj} = \Phi_{I,jk} \quad (2.10)$$

The local instantaneous balance equation for mass and momentum with corresponding jump conditions follow from equations (2.9) and (2.10) by setting $\psi_k = 1$ and $\psi_k = \mathbf{u}_k$, respectively, (Hjertager, 2007).

Mass balance and jump condition, respectively:

$$\frac{\partial \rho_k}{\partial t} + \nabla \cdot (\rho_k \mathbf{u}_k) = 0 \quad (2.11)$$

$$\dot{m}_{I,jk} + \dot{m}_{I,kj} = 0 \quad (2.12)$$

Momentum balance and jump condition, respectively:

$$\frac{\partial}{\partial t} (\rho_k \mathbf{u}_k) + \nabla \cdot (\rho_k \mathbf{u}_k \mathbf{u}_k) - \nabla \cdot \bar{\bar{T}}_k - \rho_k \cdot \mathbf{b}_k = 0, \quad (2.13)$$

$$\dot{m}_{I,jk} \mathbf{u}_j + \dot{m}_{I,kj} \mathbf{u}_k + \bar{\bar{T}} \cdot \mathbf{n}_{I,jk} + \bar{\bar{T}} \cdot \mathbf{n}_{I,kj} = \mathbf{m}_{jk}^\sigma \quad (2.14)$$

where $\bar{\bar{T}}_k$ is the stress tensor and \mathbf{b}_k is the sum of forces on phase k , and the \mathbf{m}_{jk}^σ is the superficial traction related with surface tension and has the dimension of stress:

$$\mathbf{m}_{jk}^\sigma = 2H_{jk} \sigma \mathbf{n}_{I,jk} - \nabla_{I,jk} \sigma, \quad (2.15)$$

where H_{jk} is the interface mean curvature, σ the interfacial tension and $\nabla_{I,jk}$ the gradient of interfacial tension. For chemical species with mass fraction Y_k , we have:

$$\frac{\partial}{\partial t} (\rho_k Y_k) + \nabla \cdot (\rho_k Y_k \mathbf{u}_k) = -\nabla \cdot \mathbf{F}_{Y,k} + \rho_k \Psi_k \quad (2.16)$$

and

$$\dot{m}_{I,jk} Y_j + \dot{m}_{I,kj} Y_k + \mathbf{F}_{Y,j} \cdot \mathbf{n}_{I,jk} + \mathbf{F}_{Y,k} \cdot \mathbf{n}_{I,kj} = \Psi_{I,kj} \quad (2.17)$$

Where $\mathbf{F}_{Y,k}$ is the molecular flux, Ψ_k is the generation rate and $\Psi_{I,kj}$ is the interface generation rate of Y_k .

2.4.2 Averaging Technique

There are difficulties in modelling the multiphase flows for the interaction between phases at interphase. If the number of dispersed particles in the continuous phase are large then an averaging operator is required acting on the local instantaneous balance equations. The averaging technique used mainly in multiphase flows are of three types: time average; spatial average or ensemble average. With ensemble averaging technique, the obtained equations are

independent of selection of control volume and do not lose information on the sub grid scales smaller than averaging scale. Therefore, we will use and give detail of ensemble averaging technique in this work.

In the Eulerian approach, a parameter, which may be a scalar, vector or tensor, at a fixed point in space, \mathbf{r} , at time t , is defined: $f = f(\mathbf{r}, t; \mu)$, the ensemble average on f is defined for events \mathcal{E} as:

$$\langle f(\mathbf{r}, t; \mu) \rangle^{\mathcal{E}} = \int_{\mathcal{E}} f(\mathbf{r}, t; \mu) dm(\mu) \quad (2.18)$$

where $dm(\mu)$ is the probability density on the set of events \mathcal{E} . For phase k the phase indicator function X_k is defined as:

$$X_k(\mathbf{r}, t; \mu) = \begin{cases} 1, & \text{if } \mathbf{r} \in k \\ 0, & \text{otherwise} \end{cases} \quad (2.19)$$

The ensemble average of the X_k is equivalent to the average occurrence of phase k :

$$\alpha_k = \langle X_k \rangle \quad (2.20)$$

where

$$\sum_{k=1}^N \alpha_k = 1 \quad (2.21)$$

The averaging procedure is supposed to have the following Reynolds rule properties:

$$\begin{aligned}
\langle f + g \rangle &= \langle f \rangle + \langle g \rangle, \\
\langle \langle f \rangle g \rangle &= \langle f \rangle \langle g \rangle, \\
\langle \text{constant} \rangle &= \text{constant}, \\
\left\langle \frac{\partial f}{\partial t} \right\rangle &= \frac{\partial \langle f \rangle}{\partial t}, \\
\langle \nabla f \rangle &= \nabla \langle f \rangle, \\
\langle \nabla \cdot f \rangle &= \nabla \cdot \langle f \rangle.
\end{aligned} \tag{2.22}$$

Using the definition (2.19) of phase indicator, with (2.22) and chain rule, the following equations can be derived (Drew and Passman, 1999):

$$\left\langle X_k \frac{\partial f}{\partial t} \right\rangle^\varepsilon = \left\langle \frac{\partial X_k f}{\partial t} \right\rangle^\varepsilon - \left\langle f_{kj} \frac{\partial X_k}{\partial t} \right\rangle^\varepsilon \tag{2.23}$$

$$\langle X_k \nabla f \rangle^\varepsilon = \langle \nabla (X_k f) \rangle^\varepsilon + \langle f_{kj} \nabla X_k \rangle^\varepsilon \tag{2.24}$$

$$\langle X_k \nabla \cdot f \rangle^\varepsilon = \langle \nabla \cdot (X_k f) \rangle^\varepsilon + \langle f_{kj} \cdot \nabla X_k \rangle^\varepsilon \tag{2.25}$$

In the averaging procedure, the first step is to multiply the (2.9) with (2.19), the phase indicator function X_k in this way, the following general form of averaged equation is obtained:

$$\begin{aligned} \frac{\partial}{\partial t} \langle X_k \rho_k \psi_k \rangle + \nabla \cdot \langle X_k \rho_k \psi_k \mathbf{u}_k \rangle = & - \langle X_k \mathbf{J}_k \rangle + \langle X_k \rho_k \Phi_k \rangle \\ & - \left\langle \left[\dot{m}_{I,kj} \psi_k + \mathbf{J}_k \cdot \mathbf{n}_{I,kj} \right] \frac{\partial X_k}{\partial n} \right\rangle \end{aligned} \quad (2.26)$$

The gradient of the X_k is represented as:

$$\nabla X_k = \left(\frac{\partial X_k}{\partial n} \right) \mathbf{n}_k \quad (2.27)$$

where

$$\frac{\partial X_k}{\partial n} = -\delta_k \quad (2.28)$$

where, δ_k is the Dirac's delta function related to phase k . The gradient of X_k is used as to segregate the mass and molecular fluxes at the interface.

The averaged interface jump condition equation can be obtained after multiplying (2.10) by the gradient of phase indicator:

$$\frac{1}{V} \int_V \left[\psi_j \dot{m}_{I,jk} + \psi_k \dot{m}_{I,kj} + \mathbf{J}_j \cdot \mathbf{n}_{I,jk} + \mathbf{J}_k \cdot \mathbf{n}_{I,kj} \right] dV = \frac{1}{V} \int_V \Phi_{I,jk} dV \quad (2.29)$$

Now we have the following averaged transport equations for mass and momentum balances (Drew and Passman, 1999):

Mass conservation:

$$\frac{\partial}{\partial t} (\alpha_k \bar{\rho}_k) + \nabla \cdot (\alpha_k \bar{\rho}_k \hat{\mathbf{u}}_k) = \Gamma_k \quad (2.30)$$

Momentum conservation:

$$\begin{aligned} \frac{\partial}{\partial t}(\alpha_k \bar{\rho}_k \hat{\mathbf{u}}_k) + \nabla \cdot (\alpha_k \bar{\rho}_k \hat{\mathbf{u}}_k \hat{\mathbf{u}}_k) = \nabla \cdot \left[\alpha_k \left(\langle \bar{\bar{T}}^T \rangle + \bar{\bar{T}}^{\text{Re}} \right) \right] \\ + (\alpha_k \bar{\rho}_k \mathbf{g}) + (\Gamma_k \hat{\mathbf{u}}_k) + \mathbf{M}_{I,k} \end{aligned} \quad (2.31)$$

One of the new terms appearing in (2.30) and (2.31), is Γ_k , the mass exchange term defined as:

$$\Gamma_k = -\frac{1}{V} \sum_{j=1}^N (1 - \delta_{jk}) \int_{A_{I,kj}} \dot{m}_{I,kj} \mathbf{dA} \quad (2.32)$$

The other new term are the interfacial forces $\mathbf{M}_{I,k}$ given as:

$$\mathbf{M}_{I,k} = -\frac{1}{V} \sum_{j=1}^N (1 - \delta_{jk}) \int_{A_{I,kj}} \left[\dot{m}_{I,kj} \mathbf{u}_k - \bar{\bar{T}}_k \cdot \mathbf{n}_{I,kj} \right] \mathbf{dA} \quad (2.33)$$

The following limitations are valid for mass exchange and momentum exchange, respectively:

$$\sum_{k=1}^N \Gamma_k = 0, \quad (2.34)$$

and

$$\sum_{k=1}^N \left[\Gamma_k \mathbf{u}_k + \mathbf{M}_{I,k} \right] = \frac{1}{2} \sum_{k=1}^N \sum_{j=1}^N \frac{1}{V} (1 - \delta_{kj}) \int_{A_{I,kj}} \mathbf{m}_{jk}^\sigma \mathbf{dA} = \mathbf{M}_\sigma \quad (2.35)$$

2.4.3 Closure Relation

The unclosed terms in averaged balance transport equations can be classified into three groups:

1. Viscous Stress Tensor, ($\overline{\overline{\mathbf{T}}}_k$);
2. Interfacial interaction terms, ($\Gamma_k, \mathbf{M}_{I,k}, \mathbf{M}_\sigma$);
3. Turbulence terms ($\overline{\overline{\mathbf{T}}}_k^T$).

2.4.3.1 Viscous Stress

The viscous stress tensor is sum of pressure term and shear stress term (Aris, 1962):

$$\overline{\overline{\mathbf{T}}}_k = -p_k \overline{\overline{\mathbf{I}}} + \overline{\overline{\boldsymbol{\tau}}}_k \quad (2.36)$$

The second term, the stress tensor, is formulated with Newtonian strain stress relation as following:

$$\overline{\overline{\boldsymbol{\tau}}}_k = \zeta_k (\nabla \cdot \hat{\mathbf{u}}_k) \overline{\overline{\mathbf{I}}} + 2\mu_k \left(\overline{\overline{\mathbf{S}}}_k - \frac{1}{3} \nabla \cdot \hat{\mathbf{u}}_k \overline{\overline{\mathbf{I}}} \right), \quad (2.37)$$

And strain rate tensor:

$$\overline{\overline{\mathbf{S}}}_k = \frac{1}{2} \left(\nabla \cdot \hat{\mathbf{u}}_k + (\nabla \cdot \hat{\mathbf{u}}_k)^T \right) \quad (2.38)$$

where $\overline{\overline{\mathbf{I}}}$ is the identity matrix and ζ_k is the bulk viscosity which is normally supposed to be zero for all phases. The dynamic viscosity μ_k is considered equivalent to laminar viscosity of the respective phases.

2.4.3.2 Interfacial interaction terms

When there is no mass transfer between the phases the term Γ_k vanishes, otherwise it must be defined from the modelling theory of mass transfer between phases.

The second term, $\mathbf{M}_{I,k}$ is the interfacial momentum transfer of phase k . This is expressed with sum of interfacial average pressure, shear stress acting on the phase k and the term for accounting the forces on dispersed phase particles:

$$\mathbf{M}_{I,k} = p_{I,k} \nabla \alpha_k - \overline{\overline{\boldsymbol{\tau}}}_{I,k} \nabla \alpha_k + \mathbf{M}_{I,k}^e \quad (2.39)$$

The right hand side of the momentum conservation averaged equation (2.31) can be written as in following way:

$$\begin{aligned} \nabla \cdot \left[\alpha_k \left\langle \overline{\overline{T}_k} \right\rangle \right] + (\alpha_k \overline{\rho}_k \mathbf{g}) + \Gamma_k \hat{\mathbf{u}}_k + \mathbf{M}_{I,k} = -\alpha_k \nabla \cdot p_k + \nabla \cdot (\alpha_k \overline{\overline{\tau}}_k) + (p_{I,k} - p_k) \nabla \alpha_k \\ - \tau_k \nabla \cdot \alpha_k + (\alpha_k \overline{\rho}_k \mathbf{g}) + \Gamma_k \hat{\mathbf{u}}_k + \mathbf{M}_{I,k}^e \end{aligned} \quad (2.40)$$

where the last term on the right hand side, $\mathbf{M}_{I,k}^e$ is the external force acting on the interface per unit volume. For gas-liquid systems we can write the external forces acting on the primary phase (liquid) as a linear sum (Ishii and Mishima, 1984):

$$\mathbf{M}_{I,1}^e = \sum_{k=2}^N \left(\mathbf{M}_{I,k}^D + \mathbf{M}_{I,k}^L + \mathbf{M}_{I,k}^{VM} + \mathbf{M}_{I,k}^B + \mathbf{M}_{I,k}^{TD} \right) \quad (2.41)$$

For the secondary phase (gas in case of gas-liquid system):

$$\mathbf{M}_{I,k}^e = -\mathbf{M}_{I,k}^D - \mathbf{M}_{I,k}^L - \mathbf{M}_{I,k}^{VM} - \mathbf{M}_{I,k}^B - \mathbf{M}_{I,k}^{TD}, \quad k = 2, \dots, N. \quad (2.42)$$

The terms on right hand side of above equations are, respectively, drag, lift, virtual mass, Basset history and turbulent dispersion forces. We will describe the first three forces, mainly drag and lift forces are modelled in numerical simulation of gas-liquid systems. $\mathbf{M}_{I,k}^e$ for gas-liquid system as per its definition; the force $\mathbf{F}_{I,k}$ per unit volume; if we assume the spherical shape bubble then $\mathbf{M}_{I,k}^e$ can be written as:

$$\mathbf{M}_{I,k}^e = \frac{6\alpha_k}{\pi \overline{d}_{b,k}^3} \mathbf{F}_{I,k} \quad (2.43)$$

We will now discuss the all interfacial forces and their modelling form.

2.4.3.2.1 Drag Force

In gas-liquid BCR, there is relative motion of gas bubbles to liquid. When the slip velocity (difference in phase velocities, $|\mathbf{u}_k - \mathbf{u}_l|$) is constant, then the force due to relative motion is the only drag force. While in non-uniform systems, it is necessary to expand the concept of interfacial forces and include others forces as well. The drag force has two sources: the surface friction on the surface of the immersed bubble and non-uniform pressure distribution due to shape of the bubble that is the result of non-uniform slip velocity between phases (Bird et al.,

2002). Assuming the single spherical bubble rising in the liquid, the drag force expression can be written as (Figure 2.6):

$$\mathbf{F}_{D,k} = C_{D,k} \left(\frac{\pi d_b^2}{4} \right) \frac{\rho_1}{2} |\mathbf{u}_k - \mathbf{u}_1| (\mathbf{u}_k - \mathbf{u}_1) \quad (2.44)$$

where $\left(\frac{\pi d_b^2}{4} \right) = A$ (projection area of the bubble)

Normally the drag coefficient $C_{D,k}$ depends on the flow regime (disperse phase Reynolds number) and the properties of the continuous phase. The disperse phase Reynolds number is:

$$\text{Re} = \frac{\rho_k d_b |\mathbf{u}_k - \mathbf{u}_1|}{\mu_1}, \quad (2.45)$$

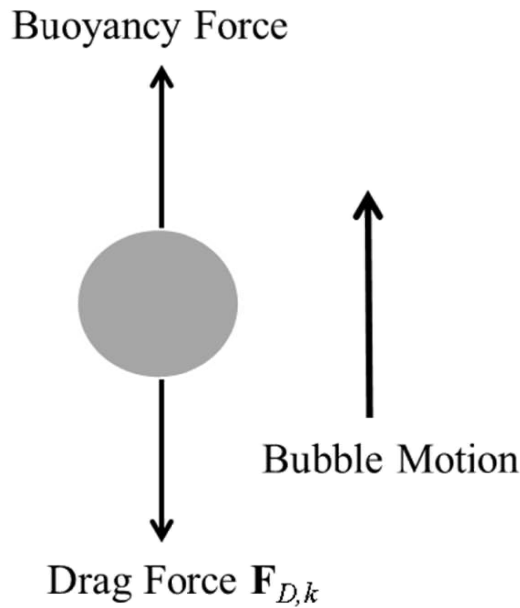


Figure 2.6 Force balance scheme for drag force for a single bubble, adapted from (Chen, 2004).

Several empirical correlations for the calculation of $C_{D,k}$, have been proposed for single bubble or particle and are given in Table 2.1. The drag coefficient can be affected by different flow regimes and can change with bubble shape, for this aspect appropriate correction factors were reported by (Clift et al., 1978). The different bubble shape regimes as function of Eötvös number (Eo) and Reynolds number (Re) are shown in Figure 2.7.

Table 2.1 Drag Coefficient correlations for single bubble/particle

Reference	Correlation
Schiller and Naumann (1935)	$C_{D,k} = \begin{cases} \text{Re}_b < 1000 \Rightarrow \frac{24}{\text{Re}} (1 + 0.15 \text{Re}^{0.687}) \\ \text{Re}_b \geq 1000 \Rightarrow 0.44 \end{cases}$ $\text{Re}_b = \frac{\rho_1 d_b \mathbf{u}_k - \mathbf{u}_1 }{\mu_1}$
Based on work of Haberman and Morton, (1956); Peebles and Garber (1953)	$C_{D,k} = \frac{4(\rho_1 - \rho_k) d_b g}{3 \rho_1 \hat{\mathbf{u}}_t},$ <p>for air-water system the terminal velocity can be calculated by Clift relation (Clift et al., 1978):</p> $\hat{\mathbf{u}}_t = \sqrt{\left(\frac{2.14\sigma}{\rho_1 d_b} + 0.505 g d_b \right)} \quad d_b \geq 1.33 \text{mm.}$
Molerus (1980)	$C_{D,k} = \frac{24}{\text{Re}} + \frac{4}{\sqrt{\text{Re}}} + 0.4$
Clift et al. (1978)	$C_{D,k} = \frac{4}{3} \left(\frac{\rho_1 - \rho_k}{\rho_1} \right) \frac{g d_{32}}{V_b^2},$ $V_b = \frac{\mu_1}{\rho_1 d_b} M^{-0.149} (J - 0.857)$ <p>with</p> $J = \begin{cases} 0.94 H^{0.751} \rightarrow 2 < H \leq 59.3 \\ 3.42 H^{0.441} \rightarrow H > 59.3 \end{cases}$ $H = \frac{4}{3} \text{EoM}^{-0.149} \left(\frac{\mu_1}{\mu_{ref}} \right)^{-0.14}, \quad \mu_{ref} = 0.0009 \text{kg m}^{-1} \text{s}^{-1}$
Johansen and Boysan (1988)	$C_{D,k} = \frac{0.622}{1.0 / \text{Eo} + 0.235} \quad \because \quad \text{Eo} = \frac{g \rho_1 - \rho_k d_b^2}{\sigma}$ <p>Valid for ellipsoidal bubble in the range, $500 < \text{Re} < 5000$</p>

Tomiyama et al., 1998	For pure systems: $C_{D,k} = \max \left[\min \left[\frac{16}{Re} (1 + 0.15 Re^{0.687}), \frac{48}{Re} \right], \frac{8}{3} \frac{Eo}{Eo + 4} \right]$
	For slightly contaminated systems: $C_{D,k} = \max \left[\min \left[\frac{24}{Re} (1 + 0.15 Re^{0.687}), \frac{72}{Re} \right], \frac{8}{3} \frac{Eo}{Eo + 4} \right]$
	For fully contaminated systems: $C_{D,k} = \max \left[\frac{24}{Re} (1 + 0.15 Re^{0.687}), \frac{8}{3} \frac{Eo}{Eo + 4} \right]$

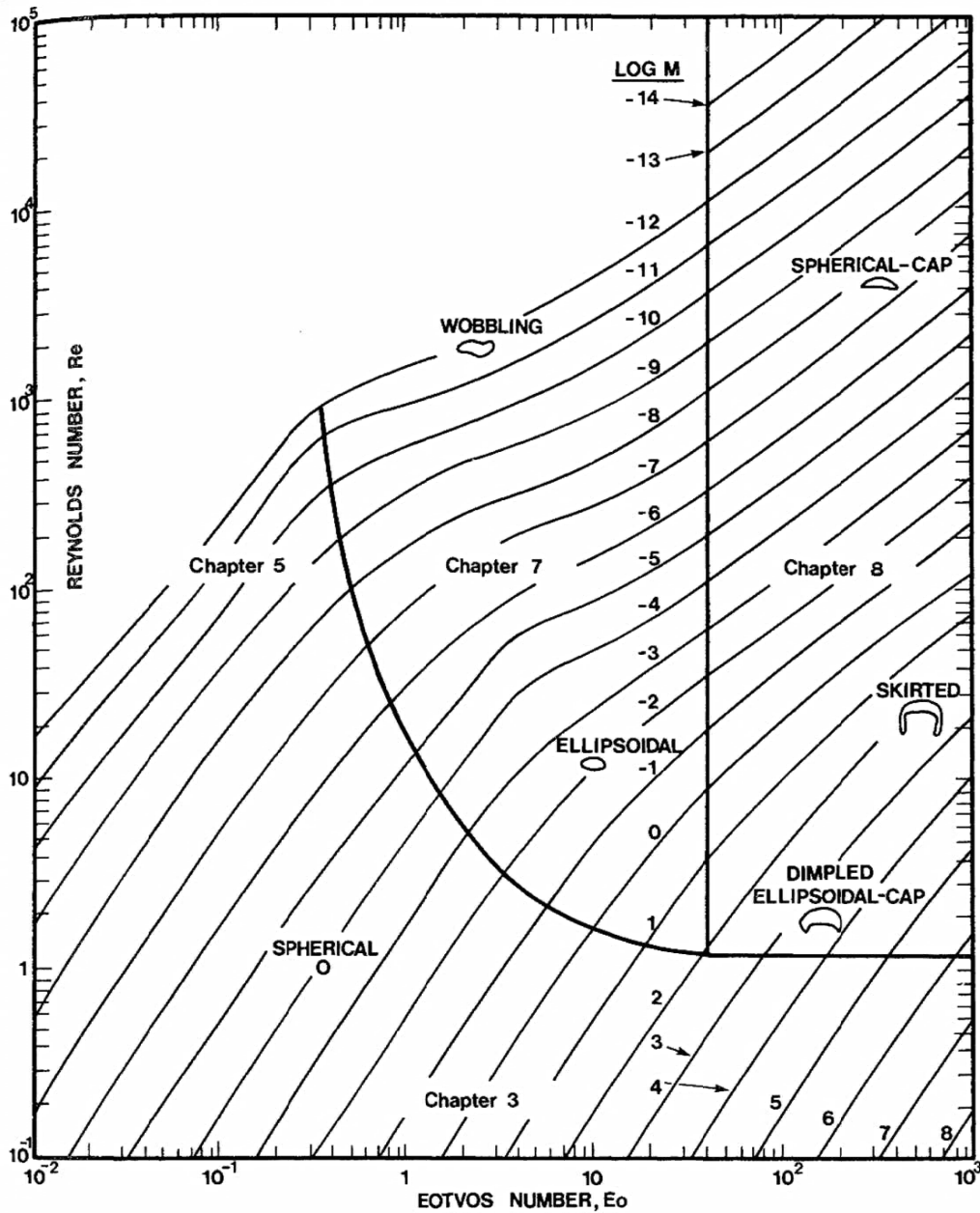


Figure 2.7 Shape regimes for bubbles and drops unhindered gravitational motion through liquids (Clift et al., 1978).

In case of swarm of bubbles, the calculation of drag coefficient becomes more complicated due to presence of nearby bubbles. For the formulation of the drag coefficient in the case of swarm of bubbles, Ishii and Zuber (1979) proposed a relation based on mixture viscosity, which take into account of the viscosity of the bubbles with additional resistance of surrounding bubbles. They proposed the following relation based on mixture viscosity identical with different flow regimes:

$$C_{D,k} = \begin{cases} \frac{24}{\text{Re}_m} & \text{Stokes Regime} \\ \frac{24}{\text{Re}_m} (1 - 0.1 \text{Re}_m^{0.75}) & \text{Undistorted Particle Regime} \\ \frac{4d_b}{6} f(\alpha_k) \sqrt{\frac{g(\rho_1 - \rho_k)}{\sigma}} & \text{Distorted Particle Regime} \\ \frac{8}{3} (1 - \alpha_k)^2 & \text{Churn Turbulent Regime} \end{cases} \quad (2.46)$$

where Re_m is defined as:

$$\text{Re}_m = \frac{d_b \rho_1 |\hat{\mathbf{u}}_1 - \hat{\mathbf{u}}_k|}{\mu_m} \quad (2.47)$$

The function $f(\alpha_k)$ is:

$$f(\alpha_k) = \begin{cases} (1 - \alpha_k)^{-0.5} & \text{for } \mu_1 \gg \mu_k \\ (1 - \alpha_k)^{-1.0} & \text{for } \mu_1 \approx \mu_k \\ (1 - \alpha_k)^{-1.5} & \text{for } \mu_1 \ll \mu_k. \end{cases} \quad (2.48)$$

Tsuji et al. (1984) proposed the following relation for two bubbles/spheres in range of Re , 100 to 500:

$$C_{D,k} = C_{(D,k)0} \left[1 - \left(\frac{d_b}{L_b} \right)^2 \right] \quad (2.49)$$

where $C_{(D,k)0}$ is the drag coefficient for a single bubble and L_b is the distance between two spheres.

For calculation of drag coefficient at interphase by using the approach of bubble velocity in swarms of bubbles, the following empirical correlation is proposed:

$$C_{D,k} = \frac{4}{3} \frac{(\rho_1 - \rho_k) g d_b}{\rho_1 V_b^2} \quad (2.50)$$

where V_b is the bubble velocity in a swarm of bubbles. For swarm of large bubbles, Krishna and Van Baten (1999) proposed the following relation:

$$V_b = V_{b\infty} \left(2.25 + 4.09 U_{\text{sup, gas}} \right) \quad (2.51)$$

where $V_{b\infty}$ is the single bubble rise velocity of and $U_{\text{sup, gas}}$ is the superficial velocity of dispersed phase. The above relation is applicable for large bubble sizes in swarm.

In work of Simonnet et al. (2007) it was suggested that, up to 15% volume fraction has hinder effect on relative bubble velocity Behzadi et al. (2004), on the other hand, found that void fraction increases the drag coefficient.

2.4.3.2.2 Transversal or Lateral Force (Lift Force)

The action of the transverse or lift force on a bubble is to govern the direction of transverse migration of the bubble in a shear field. Many experimental studies suggest that the lateral movement of the bubble depends on bubble size, as small bubbles tend to move towards the wall of the vessel and larger bubble towards the centre of the vessel. The parameters affecting the transverse acting on a spherical bubble in a shear flow are (a) relative velocity between dispersed and continuous phases; (b) shear rate of continuous phase; (c) bubble rotational speed; and (d) non-slip or slip boundary condition at bubble surface. The expression for shear-induced transverse model (Auton, 1987; Drew and Lahey, 1987; Zun, 1980) is as follows:

$$\mathbf{F}_d^L = \alpha_k \rho_1 C_L (\hat{\mathbf{u}}_k - \hat{\mathbf{u}}_1) \times (\nabla \times \hat{\mathbf{u}}_1) \quad (2.52)$$

Tomiyama et al. (2002) proposed the following relation for the lift coefficient, C_L , of a single bubble:

$$C_L = \begin{cases} \min[0.288 \tanh(0.121 \text{Re}), f(\text{Eo}_d)] & \text{for } \text{Eo}_d < 4, \\ f(\text{Eo}_d) & \text{for } 4 \leq \text{Eo}_d \leq 10.7, \end{cases} \quad (2.53)$$

The $f(\text{Eo}_d)$ in the above relation is defined as:

$$f(\text{Eo}_d) = 0.00105 \text{Eo}_d^3 - 0.0159 \text{Eo}_d^2 - 0.0204 \text{Eo}_d + 0.474, \quad (2.54)$$

and the modified Eötvös number, Eo_d , is defined as:

$$\text{Eo}_d = \frac{g(\rho_1 - \rho_k) d_H^2}{\sigma}, \quad (2.55)$$

where the d_H is the maximum horizontal dimension of the bubble.

Another relationship was proposed by Hibiki and Ishii (2007) for C_L that considers swarm bubbles effects:

$$C_L = \xi \sqrt{[C_L^{\text{low Re}_m}(\text{Re}_m, G_s)]^2 + [C_L^{\text{high Re}_m}(\text{Re}_m, G_s)]^2} \quad (2.56)$$

where Re_m :

$$\text{Re}_m = \frac{2d_b \rho_1 |\hat{\mathbf{u}}_k - \hat{\mathbf{u}}_1|}{\mu_m} \quad (2.57)$$

and G_s :

$$G_s = \left| \frac{d_b}{|\hat{\mathbf{u}}_k - \hat{\mathbf{u}}_1|} \nabla \hat{\mathbf{u}}_1 \right| \quad (2.58)$$

with:

$$\begin{cases} C_L^{\text{low } \text{Re}_m} (\text{Re}_m, G_s) = \frac{6}{\pi^2 (2 \text{Re}_m G_s)^{1/2}} \frac{2.255}{(1 + 0.1 \text{Re}_m / G_s)^{3/2}} \\ C_L^{\text{high } \text{Re}_m} (\text{Re}_m, G_s) = \frac{1}{2} \left(\frac{1 + 16 \text{Re}_m^{-1}}{1 + 29 \text{Re}_m^{-1}} \right) \end{cases} \quad (2.59)$$

The low Re_m (<1000) and coefficient ξ accounts the shape of bubbles with following relation:

$$\xi = 2 - \exp(0.136 Eo^{1.11}) \quad (2.60)$$

2.4.3.2.3 Virtual Mass Force

When a particle or a bubble accelerates in a continuous phase (liquid), it will also accelerate the neighbouring liquid around the particle or bubble. This is the induced acceleration due to bubble motion and surrounding liquid experiences an extra force which is called added mass, added inertia or virtual force. It is clear that when a bubble is rising with constant rise velocity then this phenomenon also exists but does not result in added mass force if the bubble is spherical. In such a non-uniform flow when there is the induced acceleration, this creates a resistance force on the bubble equal to the one half of mass of displaced liquid times the acceleration of the bubble (Drew et al., 1979). The general expression as developed by Drew and Lahey (1987) is given as:

$$\mathbf{F}_d^{VM} = \alpha_k \bar{\rho}_l C_{VM} \left[\left(\frac{D}{Dt} \hat{\mathbf{u}}_k - \frac{D}{Dt} \nabla \hat{\mathbf{u}}_1 \right) + (\hat{\mathbf{u}}_1 - \hat{\mathbf{u}}_k) \cdot (\nabla \hat{\mathbf{u}}_k - \nabla \hat{\mathbf{u}}_1) \right] \quad (2.61)$$

The C_{VM} is the virtual mass coefficient and it relates to the fractional volume accelerated due to the bubble and generally, it is shape (bubble shape) and gas fraction α_k dependent with range between 0.25-0.5. In case of swarm of bubbles, the following relation was suggested by van Wijngaarden (1979):

$$C_{VM} = C_{VM\infty} (1 + 2.78 \alpha_k), \quad (2.62)$$

where $C_{VM\infty}$ is the virtual mass coefficient for a single bubble.

In our present work, we will model the effect of virtual force on the gas-liquid system but will not consider it as a permanent interfacial force in modelling the

gas-liquid system along with drag force, as there are not found any significant contributions of virtual mass force on the results of local hydrodynamics of laboratory scale BCR, according to the observations of many researchers (Deen et al., 2001; Hunt et al., 1987; Sokolichin et al., 2004; Thakre and Joshi, 1999; Tabib et al., 2008; Zhang et al., 2006).

2.4.3.2. Basset History Force

The Basset history force is the viscous force due to relative acceleration between the continuous and dispersed phases, and the formation of the boundary layer around the bubble. . Basset force is named as Basset history force due to involvement of a history integral, and it is time-consuming to calculate this integral. The Basset force is relevant only for unsteady flows and in most cases its magnitude is very small as compared to the drag force. Therefore, it is often neglected while integrating the equation of motion of the bubble. Picart et al. (1982) discussed the conditions; based on them the Basset force can be ignored. The Basset force can be represented according to Drew and Lahey (1987) in following manner:

$$\mathbf{F}_d^B = \frac{9}{d_b} \alpha_1 \sqrt{\frac{\rho_1 \mu_1}{\pi}} \int_0^t \frac{a(r, t)}{\sqrt{t - \tau}} d\tau, \quad (2.63)$$

Where $a(r, t)$ is the acceleration between phases:

$$a(r, t) = \left(\frac{D}{Dt} \mathbf{u}_k - \frac{D}{Dt} \mathbf{u}_1 \right) - (\mathbf{u}_k - \mathbf{u}_1) \times (\nabla \times \mathbf{u}_1) \quad (2.64)$$

2.4.4 Turbulence Closure

Turbulence more importantly increases the rate of mixing and other transport processes with disadvantages of increase in friction and energy losses. Several different turbulence modelling approaches have been developed on the basis of, DNS (direct numerical simulation), LES (large eddy simulations) and RANS (Reynolds-averaged Navier-Stokes equation). RANS-based models are most important for reactor engineers and two-equation $k-\varepsilon$ model is the baseline for successful application in describing the main features of turbulent systems. An overview of different turbulence modelling approaches is presented in Figure 2.8. We will mainly focus on standard two-equation $k-\varepsilon$ model which allow on calculating the length scale and velocity scales of turbulence with separate transport equations (Launder and Spalding, 1974; Launder et al., 1984).

The assumption for the k - ε model is that the flow is totally turbulent and the influences of the molecular viscosity are neglected. In the standard single phase k - ε model of turbulence (Launder and Spalding, 1974), turbulent viscosity μ_{TUR} is related to k and ε with following equation:

$$\mu_{TUR} = \frac{C_\mu \bar{\rho} k^2}{\varepsilon} \quad (2.65)$$

The transport equations for k (turbulence kinetic energy) and ε (turbulence dissipation rate) can be as follows:

$$\frac{\partial(\bar{\rho}k)}{\partial t} + \frac{\partial(\bar{\rho}\hat{\mathbf{u}}k)}{\partial x_i} = \frac{\partial}{\partial x_i} \left(\frac{\mu_{TUR}}{\sigma_k} \frac{\partial k}{\partial x_i} \right) + G - \bar{\rho}\varepsilon \quad (2.66)$$

$$\frac{\partial(\bar{\rho}\varepsilon)}{\partial t} + \frac{\partial(\bar{\rho}\hat{\mathbf{u}}_i\varepsilon)}{\partial x_i} = \frac{\partial}{\partial x_i} \left(\frac{\mu_{TUR}}{\sigma_\varepsilon} \frac{\partial \varepsilon}{\partial x_i} \right) + \frac{\varepsilon}{k} (C_1 G - C_2 \bar{\rho}\varepsilon) \quad (2.67)$$

with

$$G = \frac{1}{2} \mu_{TUR} \left[\nabla \bar{\mathbf{u}} + (\nabla \bar{\mathbf{u}})^{TUR} \right]^2 \quad (2.68)$$

Kataoka and Serizawa (1989), proposed the following model for continuous phase (liquid) only. The model is the extended form of above standard k - ε model from single phase to gas-liquid (multiphase system). The model equations are given below:

$$\frac{\partial}{\partial t} (\bar{\rho}k) + \nabla \cdot (\alpha \bar{\rho} \hat{\mathbf{u}} k)_1 = \nabla \cdot \left(\alpha \frac{\mu_{TUR}}{\sigma_k} \nabla k \right) + \alpha_1 (G_1 - \bar{\rho}\varepsilon + P_{b,k})_1, \quad (2.69)$$

$$\frac{\partial}{\partial t} (\alpha \bar{\rho} \varepsilon)_1 + \nabla \cdot (\alpha \bar{\rho} \hat{\mathbf{u}} \varepsilon)_1 = \nabla \cdot \left(\alpha \frac{\mu_{TUR}}{\sigma_\varepsilon} \nabla \varepsilon \right) + \alpha_1 \left(\frac{\varepsilon}{k} (C_1 G_1 - C_2 \bar{\rho} \varepsilon) + P_{b,\varepsilon} \right)_1, \quad (2.70)$$

where G_1 is the turbulence generation term, can be written as:

$$G_1 = \bar{\tau}_1 : \nabla \bar{\mathbf{u}}_1 \quad (2.71)$$

The model constants in all above equations have the similar proposed values i.e., in the standard model and Kataoke and Serzawa extended model; (2.69) (2.70), C_μ , C_1 , C_2 , σ_k and σ_ε have default values as followed $C_\mu = 0.09, C_1 = 1.44, C_2 = 1.92, \sigma_k = 1.0, \sigma_\varepsilon = 1.3$.

The parameters $P_{b,k}$, and $P_{b,\epsilon}$, are represent as (Sato and Sekoguchi, 1975):

$$P_{b,k} = C_b \mathbf{M}_1^D \cdot (\hat{\mathbf{u}}_k - \hat{\mathbf{u}}_1) \quad C_b, \text{ Range } (0.02 - 0.75) \quad (2.72)$$

And

$$P_{b,\epsilon} = C_{be} (1 - \alpha_1) \bar{\rho}_1 \frac{k_1^{3/2}}{d_b} \quad C_{be}, \text{ Range } (0.02 - 0.2) \quad (2.73)$$

where C_b and C_{be} are constants and their ranges are given on right hand side of equations, their physical meaning are taken in percentages. For example, C_b range, (0.02-0.75) mean; (2-75%) of bubble induced turbulence drives into large eddy structure of the liquid phase. More comment on turbulent closures for multiphase systems are reported in Chapter 4.

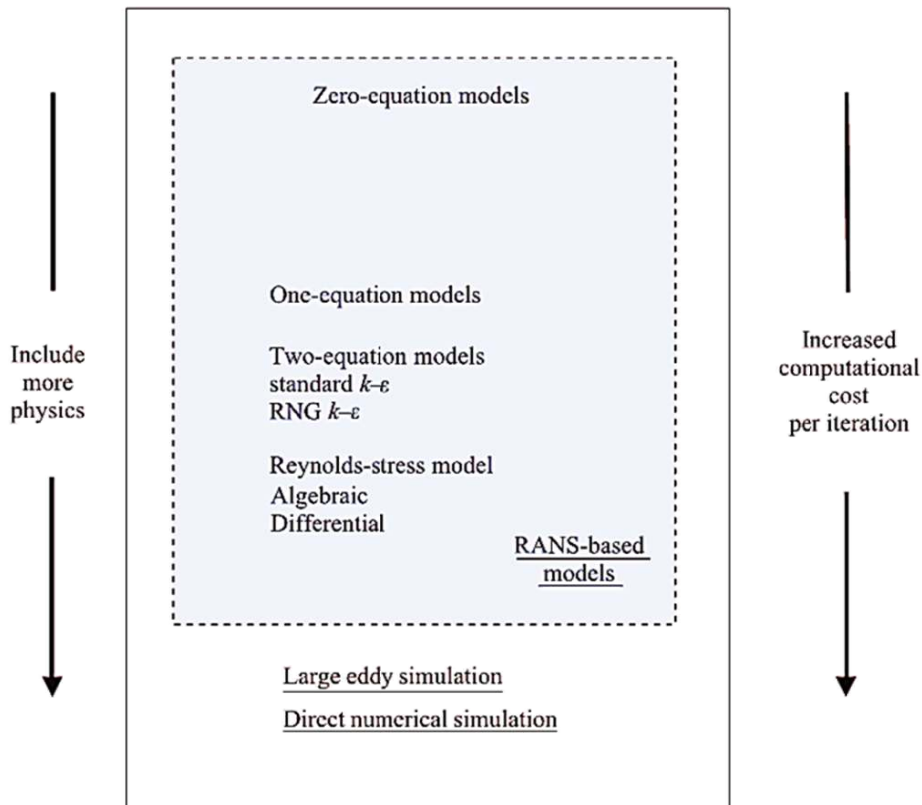


Figure 2.8 Modelling approaches for turbulent flows adapted from (Ranade, 2002)

2.4.5 Summary of Model Equations

In this section, we are presenting the summary of model equations. The terms in interphase forces only the drag coefficient we are including and ignoring the others;

i. Mass Conservation

$$\frac{\partial}{\partial t}(\alpha_k \bar{\rho}_k) + \nabla \cdot (\alpha_k \bar{\rho}_k \hat{\mathbf{u}}_k) = \Gamma_k \quad (2.74)$$

$$\sum_{k=1}^N \alpha_k = 1 \quad k = 1, 2, \dots, N \quad (2.75)$$

$$\sum_{k=1}^N \Gamma_k = 0 \quad (2.76)$$

ii. Momentum Conservation (continuous phase, $k=1$)

$$\begin{aligned} & \frac{\partial}{\partial t}(\alpha_1 \bar{\rho}_1 \hat{\mathbf{u}}_1) + \nabla \cdot (\alpha_1 \bar{\rho}_1 \hat{\mathbf{u}}_1 \hat{\mathbf{u}}_1) = -\alpha_1 \nabla p + (\alpha_1 \bar{\rho}_1 \mathbf{g}) + (\Gamma_1 \hat{\mathbf{u}}_1) \\ & + \nabla \cdot \left(\alpha_1 (\mu_1 + \mu_{TUR}) (\nabla \hat{\mathbf{u}}_1 + (\nabla \hat{\mathbf{u}}_1)^T) \right) - \nabla \cdot \left(\alpha_1 \mu_1 \left(\frac{1}{3} \nabla \hat{\mathbf{u}}_1 \bar{I} \right) \right) \quad (2.77) \\ & - \sum_{k=2}^N \frac{3}{4} \bar{\rho}_1 \alpha_k \frac{C_{D,k}}{d_b} |\hat{\mathbf{u}}_k - \hat{\mathbf{u}}_1| (\hat{\mathbf{u}}_k - \hat{\mathbf{u}}_1) \end{aligned}$$

iii. Momentum Conservation (disperse phase, ($k=2, \dots, N$))

$$\begin{aligned} & \frac{\partial}{\partial t}(\alpha_k \bar{\rho}_k \hat{\mathbf{u}}_k) + \nabla \cdot (\alpha_k \bar{\rho}_k \hat{\mathbf{u}}_k \hat{\mathbf{u}}_k) = -\alpha_k \nabla p + (\alpha_k \bar{\rho}_k \mathbf{g}) + (\Gamma_k \hat{\mathbf{u}}_k) \\ & - \frac{3}{4} \bar{\rho}_1 \alpha_k \frac{C_{D,k}}{d_b} |\hat{\mathbf{u}}_k - \hat{\mathbf{u}}_1| (\hat{\mathbf{u}}_k - \hat{\mathbf{u}}_1) \quad (2.78) \end{aligned}$$

iv. Conservation of the Chemical Species

$$\frac{\partial}{\partial t}(\alpha_k \bar{\rho}_k \hat{Y}_k) + \nabla \cdot (\alpha_k \hat{\mathbf{u}}_k \hat{Y}_k) = -\nabla \cdot \alpha_k (\hat{\mathbf{F}}_{Y,k} + \hat{\mathbf{F}}_{T,k}^T) + \hat{Y}_k \Gamma_k + \alpha_k \bar{\rho}_k \hat{\Psi}_k \quad (2.79)$$

Chapter 3

FLOW SIMULATION WITH FIXED BUBBLE SIZE

3.1 Introduction

In this chapter we will discuss the numerical simulation of rectangular shaped bubble column reactor with fixed bubble size for air-water fluid system by using Commercial FLUENT 13 package. Two different gas flow rates, 48 L/h and 260 L/h are applied and their results are compared with available experimental data. The dimensions and physical conditions of the bubble column reactor (BCR) are given in, Table 3.1 and general geometry layout is shown in Figure 3.1. For detailed experimental setup and geometry layout of column, refer to the papers (Pfleger et al., 1999; Buwa and Ranade, 2002; Buwa et al., 2006).

Table 3.1 Bubble column used in simulation: Geometry and physical conditions.

Parameter	Definition
Size of BCR	$L \times W \times H = 200 \times 50 \times 675$ (mm)
Liquid Level	450 mm
Gas Flow Rate	48 L/h and 260 L/h
Sparger and its dimensions	Plate with 8 holes with diameter 0.8 mm, installed in centre of bottom of column. Size: $L \times W = 24 \times 12$ (mm)
Phases	Continuous Phase: Liquid water Dispersed Phase: Air
Bubble Diameter	4 mm or specified

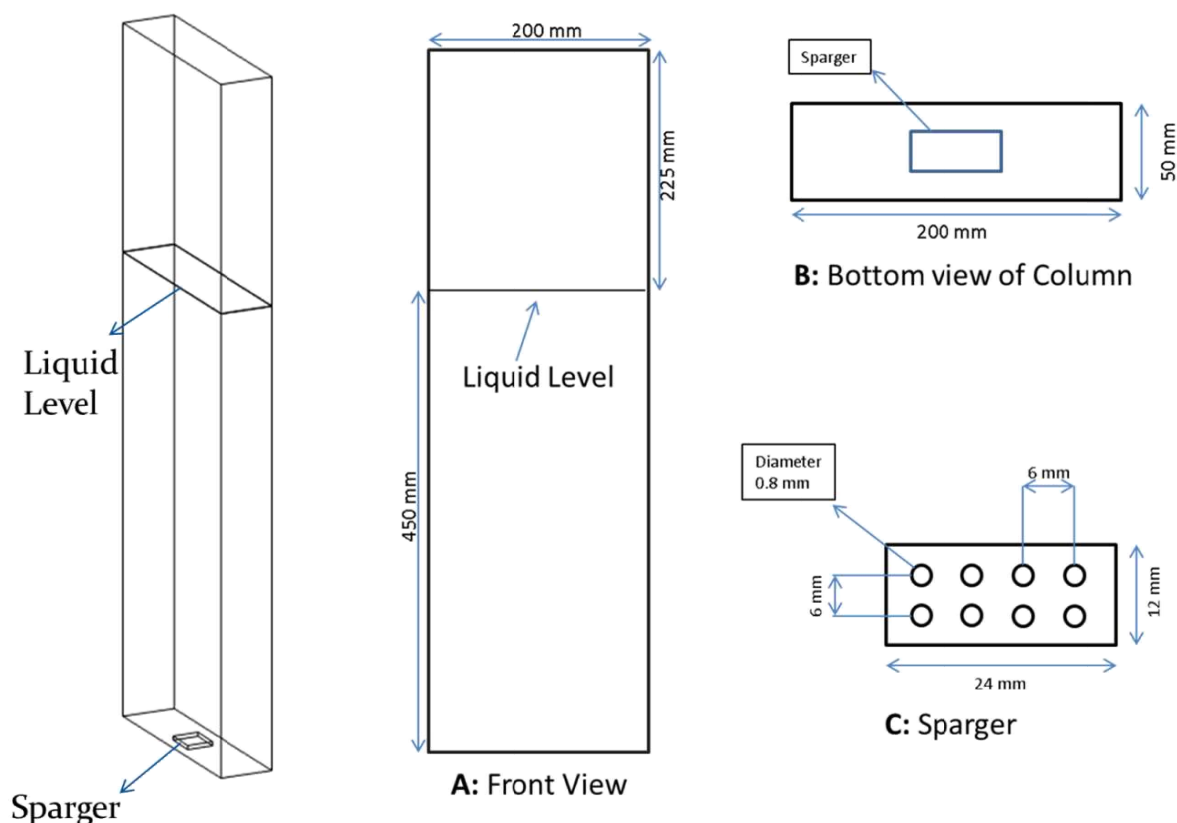


Figure 3.1 Geometric layout of the bubble column used in simulations, (A) is the front view, (B) is the bottom view of the column with sparger in middle of the base, (C) is sparger dimensions with 8 holes having diameter of 0.8 mm each.

In this chapter we will show the results obtained by assuming uniform bubble size in the simulations, while the study of the role of the actual bubble size distribution, originated by coalescence and breakage, is left to subsequent chapters.

3.2 Simulation Setup

In this section we will discuss the CFD methods used in BCR simulation of present work and will compare and discuss the results with experimental results.

3.2.1 Computational Model

The commercial CFD software FLUENT (ANSYS, Version 13) is used to numerically model the hydrodynamics of the BCR. The code technique bases on the finite volume methods with Euler-Euler (E-E) two fluid model to simulate the multiphase flows in bubble column.

With E-E approach, α_k is the volume fraction of phase k , clearly at any point of the system the volume fractions must sums to one:

$$\sum_{k=1}^n \alpha_k = 1.0 \quad (3.1)$$

where n is the number of phases.

For each phase the continuity balance equation in the absence of mass transfer and source terms can be written:

$$\frac{\partial(\alpha_k \rho_k)}{\partial t} + \nabla \cdot (\alpha_k \rho_k \mathbf{u}_k) = 0 \quad (3.2)$$

The momentum transfer equation for multiphase flows is calculated by Navier-Stokes equation for phase k :

$$\begin{aligned} & \frac{\partial(\alpha_k \rho_k \mathbf{u}_k)}{\partial t} + \nabla \cdot (\alpha_k \rho_k \mathbf{u}_k \mathbf{u}_k) \\ & = -\alpha_k \nabla p - \nabla \cdot (\alpha_k \boldsymbol{\tau}_k) + \alpha_k \rho_k \mathbf{g} + \mathbf{M}_{k,l} \end{aligned} \quad (3.3)$$

The terms on the right hand side of the equation, respectively, represent the pressure gradient shared by both phases, viscous stress, gravity and, $\mathbf{M}_{k,l}$ represents the interphase momentum forces between phase k and all other phases present in the system. $\mathbf{M}_{k,l}$ is given as with subscripts of liquid as L and of gas as G :

$$\mathbf{M}_L = -\mathbf{M}_G = \mathbf{M}_{D,L} + \mathbf{M}_{L,L} + \mathbf{M}_{VM,L} \quad (3.4)$$

where the sum of forces on right hand side are drag, lift and virtual mass forces, respectively. The drag force is given as:

$$\mathbf{M}_{D,L} = -\frac{3}{4} \frac{\alpha_G \rho_L C_D}{d_B} |\mathbf{u}_G - \mathbf{u}_L| (\mathbf{u}_G - \mathbf{u}_L) \quad (3.5)$$

Different correlations for drag coefficient are proposed in Chapter 2. In the present work, we will use the user defined function for drag coefficient based on constant terminal velocity, 20 cm/s.

Mainly, we simulated the systems with drag force only but the lift force and virtual mass forces were also occasionally used for comparison purpose. The lift force is given in (3.6) and C_L is the lift coefficient:

$$\mathbf{M}_{L,L} = -\alpha_G \rho_L C_L (\mathbf{u}_G - \mathbf{u}_L) \times \nabla \times \mathbf{u}_L \quad (3.6)$$

We applied a constant value of C_L based on the following relation (Tomiyama, 2004):

$$C_L = \begin{cases} \min \left[0.288 \tanh(0.121 \text{Re}), f(Eo_d) \right] & \text{for } Eo_d < 4, \\ f(Eo_d) & \text{for } 4 \leq Eo_d \leq 10.7, \end{cases} \quad (3.7)$$

where

$$f(Eo_d) = 0.00105 Eo_d^3 - 0.0159 Eo_d^2 - 0.0204 Eo_d + 0.474$$

and

$$Eo_d = \frac{g(\rho_L - \rho_G) d_H^2}{\sigma}$$

The virtual mass force is given as:

$$M_{VM,L} = -0.5 \alpha_G \rho_L \alpha_L \left(\frac{D\mathbf{u}_G}{Dt} - \frac{D\mathbf{u}_L}{Dt} \right) \quad (3.8)$$

In present work the standard two phase k - ε model is used as a turbulence model. In the standard single phase k - ε model of turbulence (Launder and Spalding, 1974), turbulent viscosity μ_{TUR} is related to k and ε with following equation:

$$\mu_{TUR,L} = \frac{C_\mu \rho_L k_L^2}{\varepsilon_L} \quad (3.9)$$

The transport equations for k (turbulence kinetic energy) and ε (turbulence dissipation rate) can be as follows:

$$\frac{\partial(\rho_L \alpha_L k)}{\partial t} + \nabla(\rho_L \alpha_L \mathbf{u}_L k) = \nabla \left(\alpha_L \frac{\mu_{eff,L}}{\sigma_k} \nabla k \right) + \alpha_L (G - \rho_L \varepsilon) \quad (3.10)$$

$$\frac{\partial(\rho_L \alpha_L \varepsilon)}{\partial t} + \nabla(\rho_L \alpha_L \mathbf{u}_L \varepsilon) = \nabla \left(\alpha_L \frac{\mu_{eff,L}}{\sigma_\varepsilon} \nabla \varepsilon \right) + \alpha_L \frac{\varepsilon}{k} (C_1 G - C_2 \rho_L \varepsilon) \quad (3.11)$$

where G is the turbulence generation term written as:

$$G = \frac{1}{2} \mu_{TUR} \left[\nabla \bar{U} + (\nabla \bar{U})^{TUR} \right]^2 \quad (3.12)$$

And the effective viscosity:

$$\mu_{eff,L} = \mu_{lam,L} + \frac{\mu_{TUR,L}}{\sigma_k} \quad (3.13)$$

The model constants in equations(3.9)(3.10)(3.11), C_μ , C_1 , C_2 , σ_k and σ_ϵ have default values as follows:

$$C_\mu = 0.09, C_1 = 1.44, C_2 = 1.92, \sigma_k = 1.0, \sigma_\epsilon = 1.3$$

3.2.2 Boundary Conditions

The inlet boundary is defined as velocity inlet. The inlet velocity of the gas (air) is defined as follows according to the volumetric gas flow rate (GFR):

$$V_{in} = \frac{GFR}{A_{sparger} \cdot \alpha_{sparger}} \quad (3.14)$$

$A_{sparger}$ is the inlet cross sectional area of sparger and $\alpha_{sparger}$ is the porosity of the sparger.

Inlet velocity of water was taken as zero. The initial level of pure water was always set to 450 mm.

The outlet boundary is defined as pressure outlet with back flow volume fraction of 1 of gas.

3.3 Gas Flow Rate 48 L/h

3.3.1 Grid Dependencies

For four cases, of different grid sizes, named A, B, C, and D, we studied the dynamics of multiphase flows in rectangular bubble column with E-E approach and using similar simulation parameters. Grid size picture comparison is shown in Figure 3.2. Case A is the course one and Case D is the finest one.

Three-dimensional (3-D), transient simulations were performed to calculate the liquid axial velocity profiles, gas holdup, bubble plume oscillation period. The simulation parameters are given in Table 3.2.

Table 3.2 Definition of Simulation parameters for cases of grid dependencies

Parameter	Definition
Inlet gas velocity V_{in}	3.3 m/s defined according to (3.14) with GFR 48 L/h
Gas Volume Fraction at inlet	0.014, based on sparger holes area A_p per sparger cross sectional area A_t , A_p/A_t .
Multiphase Model	Eulerian two phase
Viscous Model	Standard $k-\varepsilon$ per phase
Drag Coefficient	Defined on constant terminal velocity, 20cm/s
Lift coefficient (if applied)	Defined by Tomiyama relation with respect to bubble size, for bubble size of 4 mm, the C_L is calculated as 0.3, (Tomiyama, 2004) , (3.7)
Surface Tension	Constant: 0.071N/m
Pressure-Velocity coupling	Phase coupled SIMPLE
Discretization Scheme	QUICK
Transient formulation	First order implicit
Time Step	Based on Courant number $\left(C_o = \frac{ \mathbf{u} \cdot \Delta t}{\Delta x} < 0.5 \right)$ Case A = 0.01s, Case B = 0.009s, Case C = 0.007s, Case D = 0.006s
Grid Size (L×W×H)	Case A = 32×08×53, (coarse), Case B = 64×16×108, (semi fine), Case C = 80×19×135, (fine), Case D = 96×22×162, (finest).

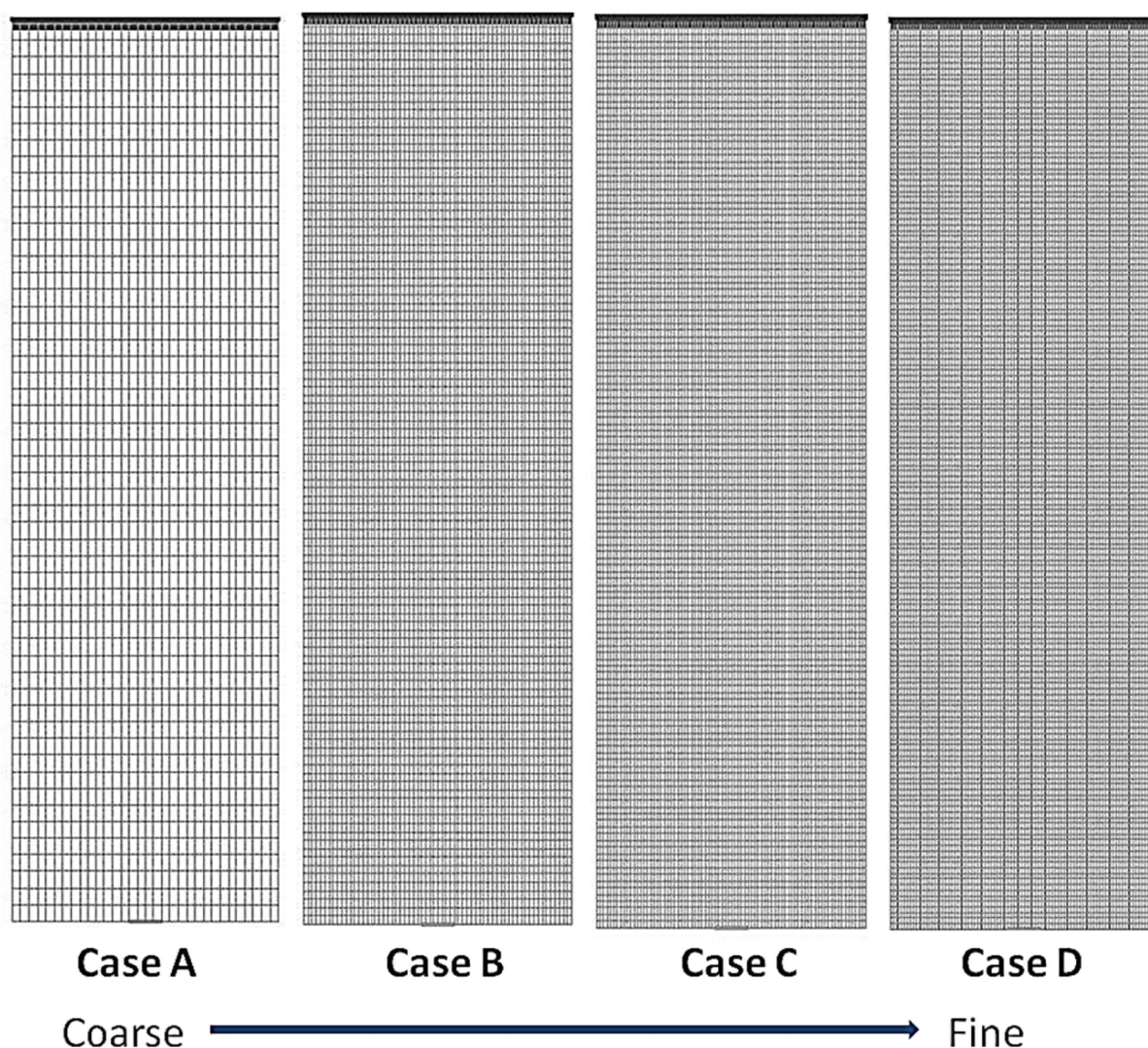


Figure 3.2 Grid pictures showing the different cases from coarse one to finest one used in present work.

3.3.2 Results and Discussion

The obtained computational results were compared with the experimental data of (Pfleger et al., 1999; Buwa and Ranade, 2002; Buwa et al., 2006). The gas holdup contours of case B, C and D are presented in Figure 3.3 and time averaged gas holdup over 120 s (for $t = 120\text{s}$ to $t = 240\text{s}$, to eliminate the effect of the transient gassing period) is shown in Figure 3.4. From the contour of cases, it is shown that bubble's plume start to oscillate around 120s of simulation. After 120s of transient simulation, we obtained the results for time averaged 120 s. Time averaged contours of gas holdup of cases of semi-fine to finest are in similar fashion while the fine case with extra interfacial lift force have different time averaged gas holdup pattern and expanded bubbles plume is observed in central part of column (Figure 3.4). In coming subsections we will

discuss the results of plume oscillation period, gas holdup and liquid axial velocity profiles.

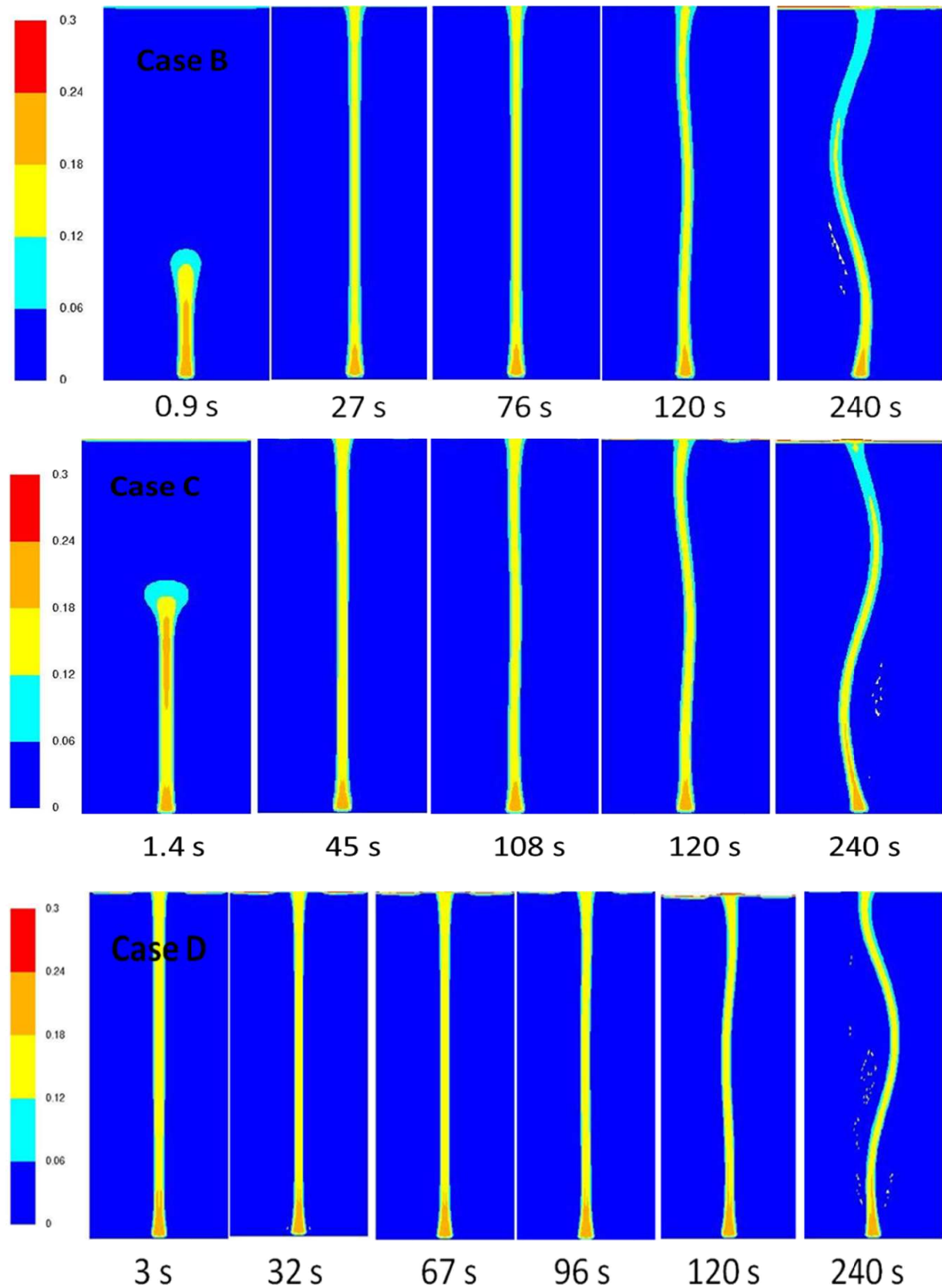


Figure 3.3 Instantaneous gas holdup contours of studied cases. The case B is coarse, D is the finest. Time is given under each of column snapshot.

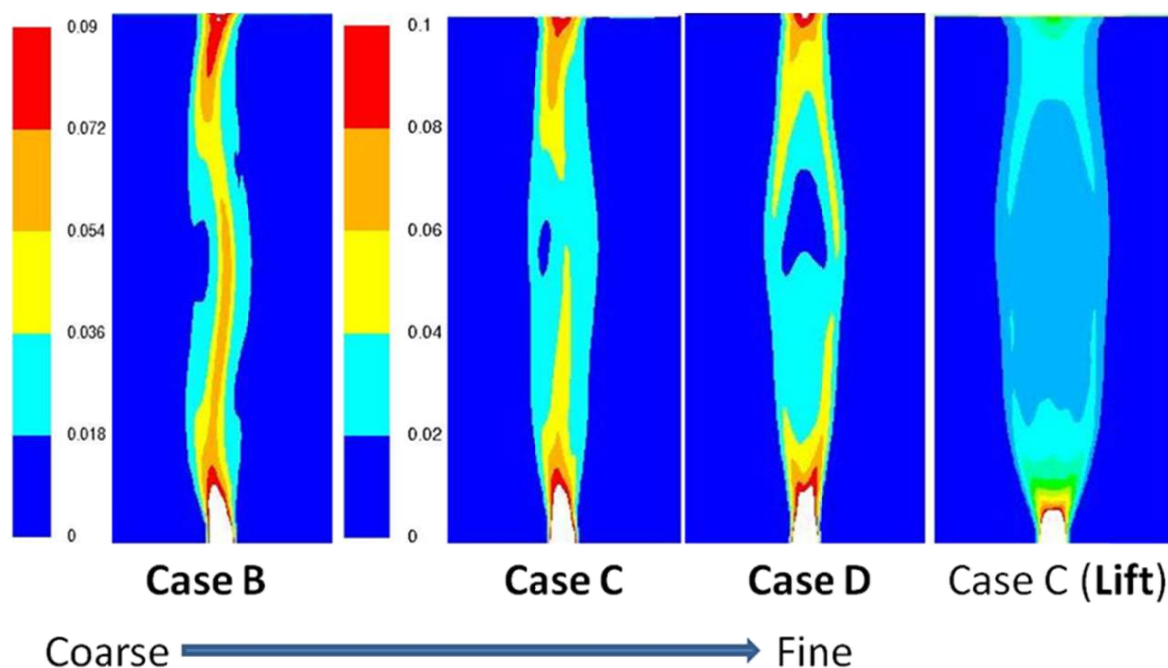


Figure 3.4 The time averaged gas holdup profile of cases from coarse to fine grid. In the left is the gas holdup profile of fine grid Case C with lift.

3.3.2.1 Calculation of Plume Oscillation Period

The bubble plume oscillation period was calculated from liquid horizontal velocity time series when the plume started to meander. The time was calculated as average of wavelength of 5-7 cycles of crest to crest or trough to trough (The length of two headed red coloured arrow of troughs or crests (Figure 3.5 upper part)). The point surface monitor was applied for this purpose at the centre of column at vertical height of 225 mm from sparger and data was taken after every time step. The horizontal velocity at the sample point for Case C is shown in Figure 4.5(a) and comparison of grids B, C and D is shown in Figure 4.5(b). The experimental average plume oscillation period as described by (Pfleger et al., 1999; Buwa and Ranade, 2002; Buwa et al., 2006) is 11-14 s. In our case we have average period time between 11-17 s. In coarse grid profile (Case A) we did not get any meandering periodic cycle, however, other grids gave good results for plume oscillation periods. We also modelled the BCR with lift for fine grid (Case C) and found excellent results for plume oscillation period, Figure 3.6. The comparison of the plume oscillation period for this section is shown in Table 3.3.

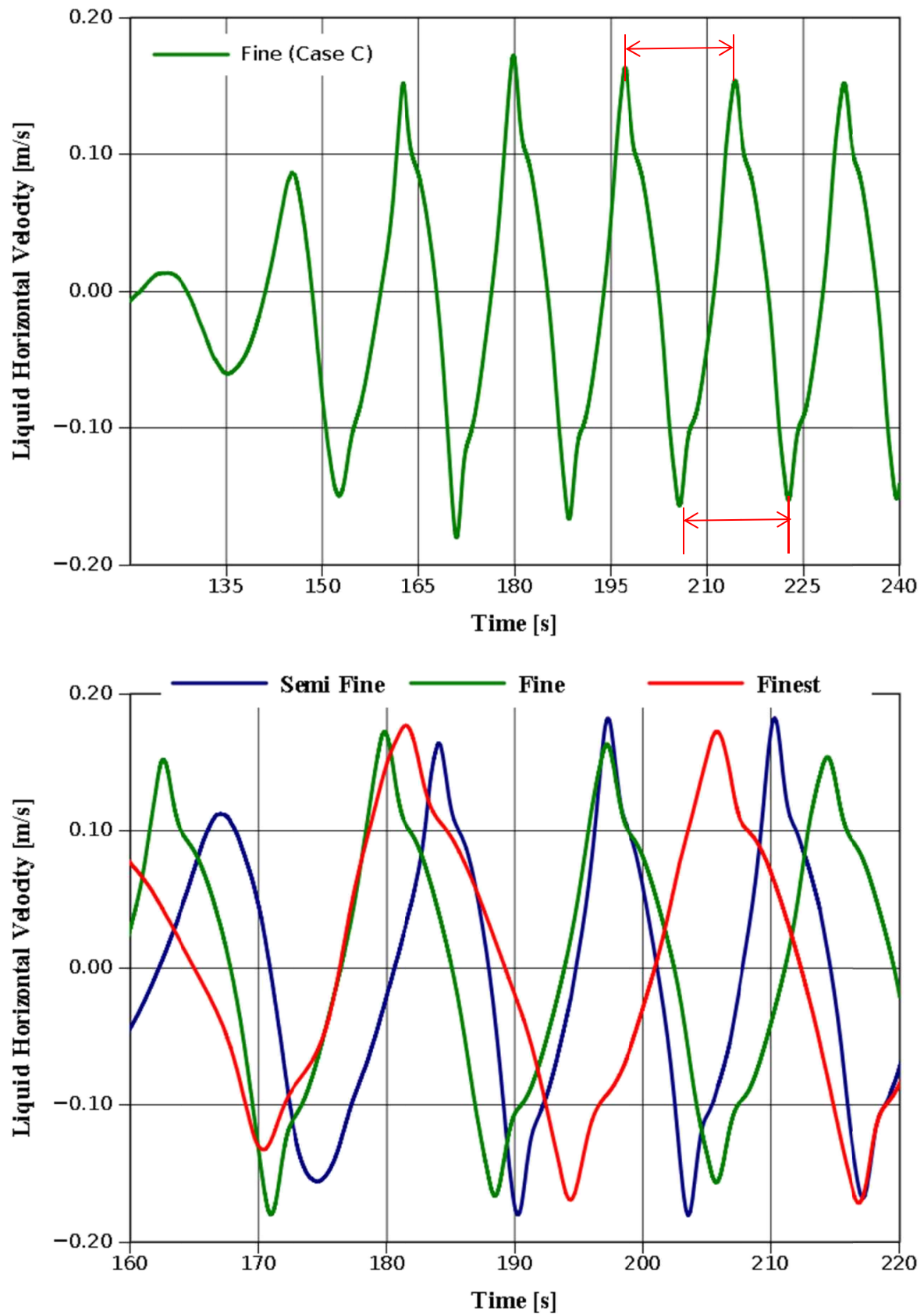


Figure 3.5 Time series of liquid horizontal velocity at centre point of column at vertical height 225 mm from sparger. Upper one is for fine grid (Case C) and is also green in lower one with other grids.

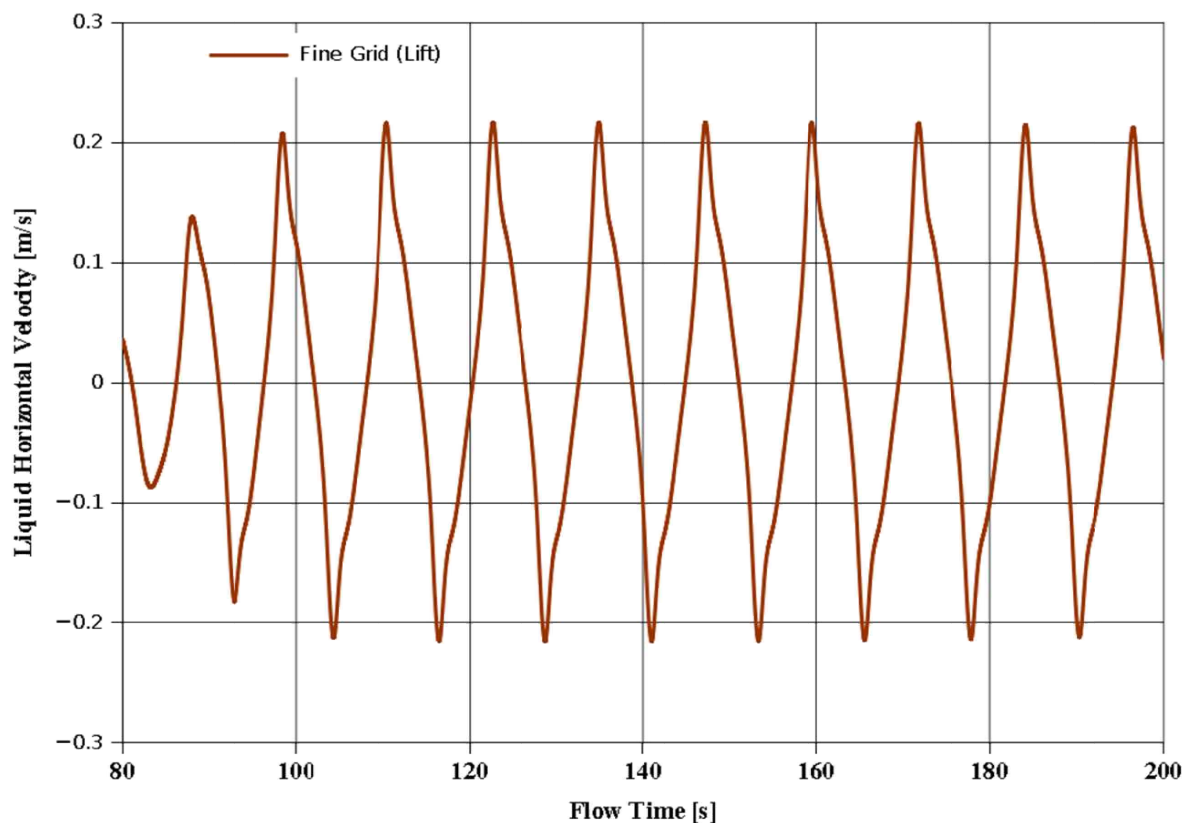


Figure 3.6 The liquid horizontal velocity time series of fine grid (Case C) with lift at centre point of column at vertical height 225 mm from sparger.

Table 3.3 Comparison of plume oscillation period of different cases with experimental simulation results.

Case	Calculated Time	Simulation (Buwa and Ranade, 2002; Buwa et al., 2006)	Experimental wall pressure fluctuation measurement (Buwa and Ranade, 2002; Buwa et al., 2006)
Semi-fine (Case B)	15 s	11 s	14 s
Fine (Case C)	17 s		
Finest (Case D)	17 s		
Fine (Case C) with extra interfacial lift force	12 s		

3.3.2.2 Liquid Axial Velocity and Gas Holdup

For all above cases, we calculated the time averaged liquid axial velocity and gas holdup profiles along on horizontal line at vertical height 370 mm from sparger, Figure 3-7 and 3.8. It is clear that our coarse grid didn't give good result at all. The remaining cases with finer grids, however, gave good results.

The experimental data for liquid axial velocity is taken from Pflieger et al. (1999) and for gas holdup from Buwa and Ranade (2002). The time averaged profiles of Case C with names 278 s and 207 s are averaged profiles of two plume oscillation periods. The time-averaged data of two plume cycles' time during the simulation are named as 207 s and 278 s is named for after the resetting the statistical data for last two cycles of simulation. The time-averaged results of these two cycles are in good agreement as compared to 120 s averaged results and the results of two plume oscillation cycles for liquid axial velocity and gas holdup profiles are shown in bottom portions of Figure 3.7 and Figure 3.8. For our proposed model, application of lift in computational model is necessary with combination of drag force to get good result with sufficient fine grid, like case C.

In order to select grid/mesh size for next sections, on the basis of results, we chose the fine grid of case C with grid size $80 \times 19 \times 135$.

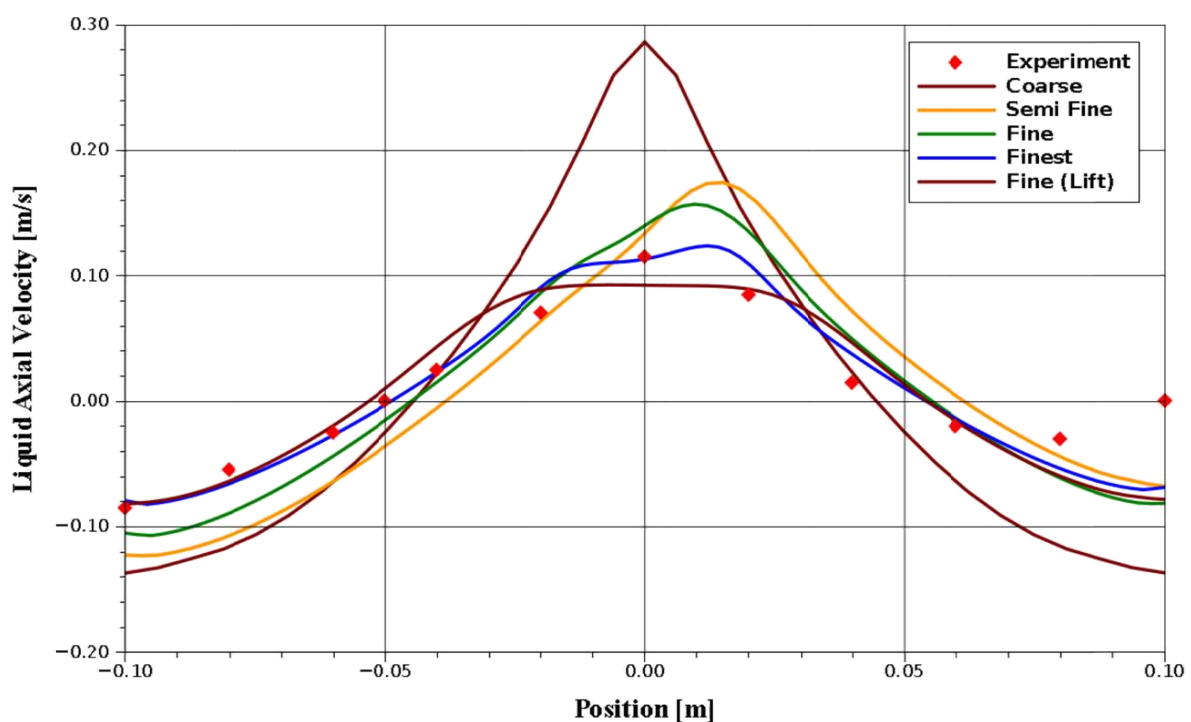


Figure 3.7 Time averaged liquid axial velocity profile at horizontal line at vertical height 0.37 m from sparger. Experimental data is taken from (Pflieger et al., 1999).

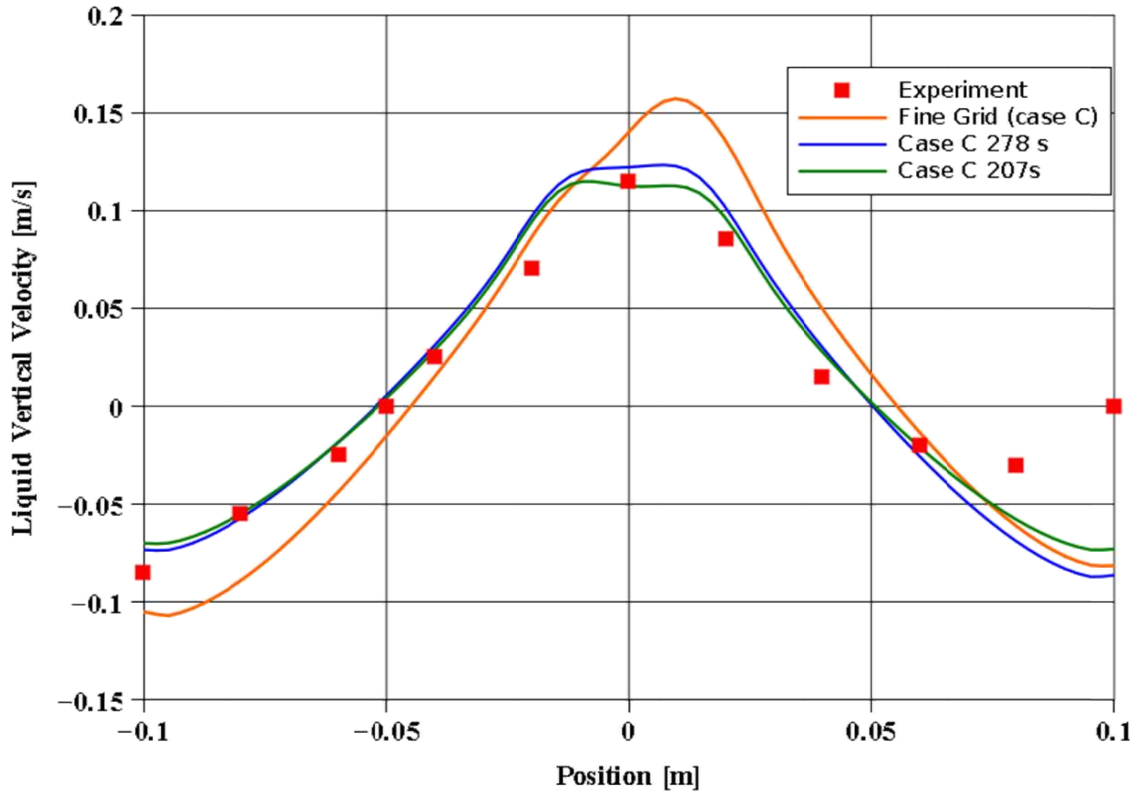


Figure 3.8 Time averaged liquid axial velocity profile at horizontal line at vertical height 0.37 m from sparger. The results are for fine grid case C with time averaged of two cycles, during the time averaged cycle and for two final periodic cycles after 240 s. Experimental data is taken from (Pfleger et al., 1999).

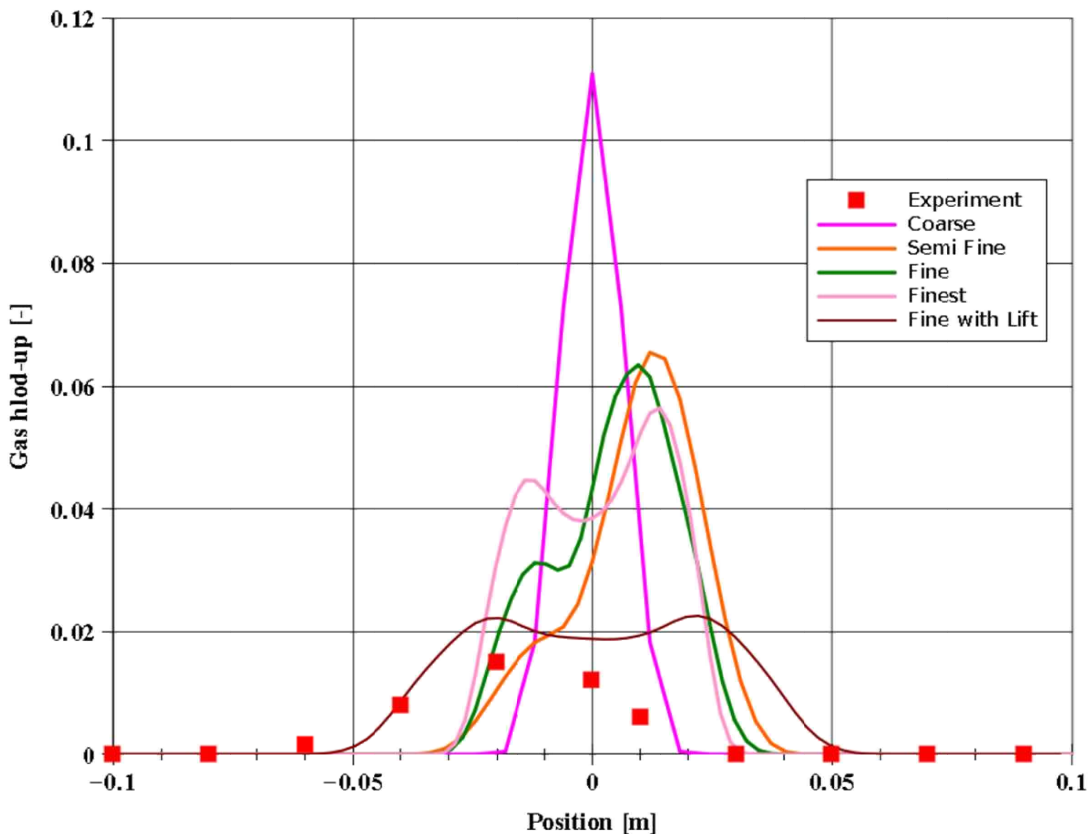


Figure 3.9 Time averaged gas holdup profile at horizontal line at vertical height 0.37 m from sparger. Experimental data is taken from (Buwa and Ranade, 2002).

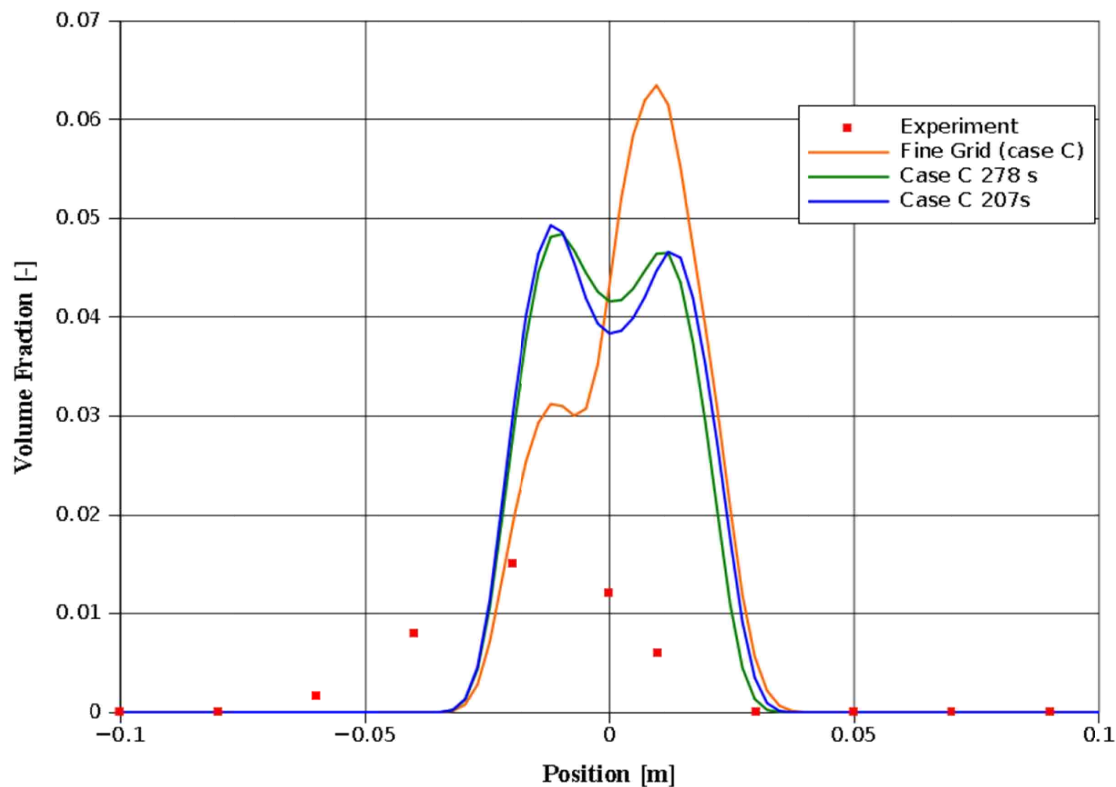


Figure 3.10 Time averaged gas holdup profile at horizontal line at vertical height 0.37 m from sparger. The results are for fine grid case C with time averaged of two cycles, during the time averaged cycle and for two final periodic cycles after 240 s. Experimental data is taken from (Buwa and Ranade, 2002).

3.4 Gas Flow Rate 260 L/h

In this section, we studied the dynamics of multiphase flows in the rectangular bubble column with gas flow rate (GFR), 260 L/h. Grid size of previous case C, (80×19×135) is chosen based on results of previous section. We have reviewed the effect of different interphase forces present in (3.4) and the effect of changed the inlet boundary condition of gas volume fraction. We have named our cases in this section with the following definitions based on case's special characteristic; drag coefficient in each case is applied with no change as defined by constant terminal velocity 20 cm/s:

1. Case **0.14**, the volume fraction at inlet is defined as 0.014.
2. Case **0.5**, the volume fraction at inlet is defined as 0.5.
3. Case **VM**, virtual mass force applied in addition with drag force and volume fraction is taken at inlet as 0.014. The virtual mass force $M_{VM,L}$ as defined by FLUENT is used (Fluent, 2009):

$$M_{VM,L} = -0.5\rho_L\alpha_G\alpha_L\left(\frac{\partial\mathbf{u}_L}{\partial t} - \frac{\partial\mathbf{u}_G}{\partial t}\right) \quad (3.15)$$

4. Case **Lift-0.3**, Lift force applied with lift coefficient (C_L) based on Tomiyama relationship (Tomiyama, 2004) (3.7). The value of C_L is taken as constant, 0.3 ($D_b = 4\text{mm}$) up to liquid level and zero in liquid free section, applied in FLUENT with user defined function.
5. Case **Lift-0.5**, traditional constant value 0.5 of C_L applied in the liquid level and zero in liquid free section, applied in FLUENT with user defined function.

The cases, 0.14 and 0.5 are with changed boundary conditions of gas volume fraction at inlet and the remaining cases are for interfacial forces. To study these implementations, the three-dimensional (3-D), transient simulations were performed to compare liquid axial velocity profiles, gas holdup, bubble plume oscillation period simulations and available experimental data. The experimental data is taken from (Buwa et al., 2006). The detailed simulation parameters are given in Table 3.4.

3.4.1 Results and Discussion

The obtained computational results are compared with the experimental data of (Buwa and Ranade, 2002; Buwa et al., 2006). The instantaneous gas holdup contours of cases 0.014, 0.5, VM, lift-0.3 and lift-0.5 are presented in Figure 3.11a and Figure 3.11b. With the change in gas volume fraction (VF) of inlet boundary condition, the difference in two gas holdup contours is in the delay of meandering behaviour of bubble hose when applied gas volume fraction is low and also in case of applied virtual mass added force as interfacial force (Figure 3.11a). On other hand, there is early meandering behaviour of bubble hose when applied gas fraction is high, as it is shown in gas holdup contour of the Case 0.5 (Figure 3.11a) and also in case of applied lift force as interfacial force (Figure 3.11b). However the gas holdup contours of case lift-0.5 are unrealistic, as we have applied larger value of lift coefficient (C_L) and bubble hose meandered towards wall more than the case lift-0.3.

The time averaged gas holdup for 120 s (120-140s) is shown in Figure 3.12. The time-averaged gas holdup contours are in similar fashion for cases in change of gas VF changes of inlet boundary condition. However, the averaged gas holdup contours with additional interfacial forces are similar with expansion of bubble

hose but high gas holdup with virtual mass along height of the column. In coming subsections we will discuss the results of plume oscillation period, gas holdup and liquid axial velocity profiles for different cases.

Table 3.4 Definition of Simulation parameters for cases for interfacial forces closure.

Parameter	Definition
Inlet gas velocity V_{in}	<ol style="list-style-type: none"> 17.86 m/s defined according to (3.14) with GFR 260 L/h and inlet gas volume fraction 0.014. 0.5 m/s defined according to (3.14) with GFR 260 L/h and assumed inlet gas volume fraction 0.5.
Gas Volume Fraction	<ol style="list-style-type: none"> 0.014, based on sparger holes area A_p per sparger cross sectional area A_t, A_p/A_t. 0.5, to study the effect of change in volume fraction at inlet.
Multiphase Model	Eulerian two phase
Viscous Model	Standard $k-\varepsilon$ per phase
Drag Coefficient	Defined on constant terminal velocity, 20cm/s
Surface Tension	Constant: 0.071N/m
Pressure-Velocity coupling	Phase coupled SIMPLE
Discretization Scheme	QUICK
Transient formulation	First order implicit
Time Step	Based on Courant number $\left(Co = \frac{ \mathbf{u} \cdot \Delta t}{\Delta x} < 0.5 \right)$ i. e. 007 s.
Grid Size (L×W×H)	Fine grid from previous section, Case C = 80×19×135.
Lift Coefficient (if applied)	<ol style="list-style-type: none"> 0.5 Defined by Tomiyama relation with respect to bubble size, for bubble size of 4 mm, the C_L is calculated as 0.3, (Tomiyama, 2004), (3.7)
Virtual mass force	As defined in FLUENT theory guide (Fluent, 2009) (3.15).

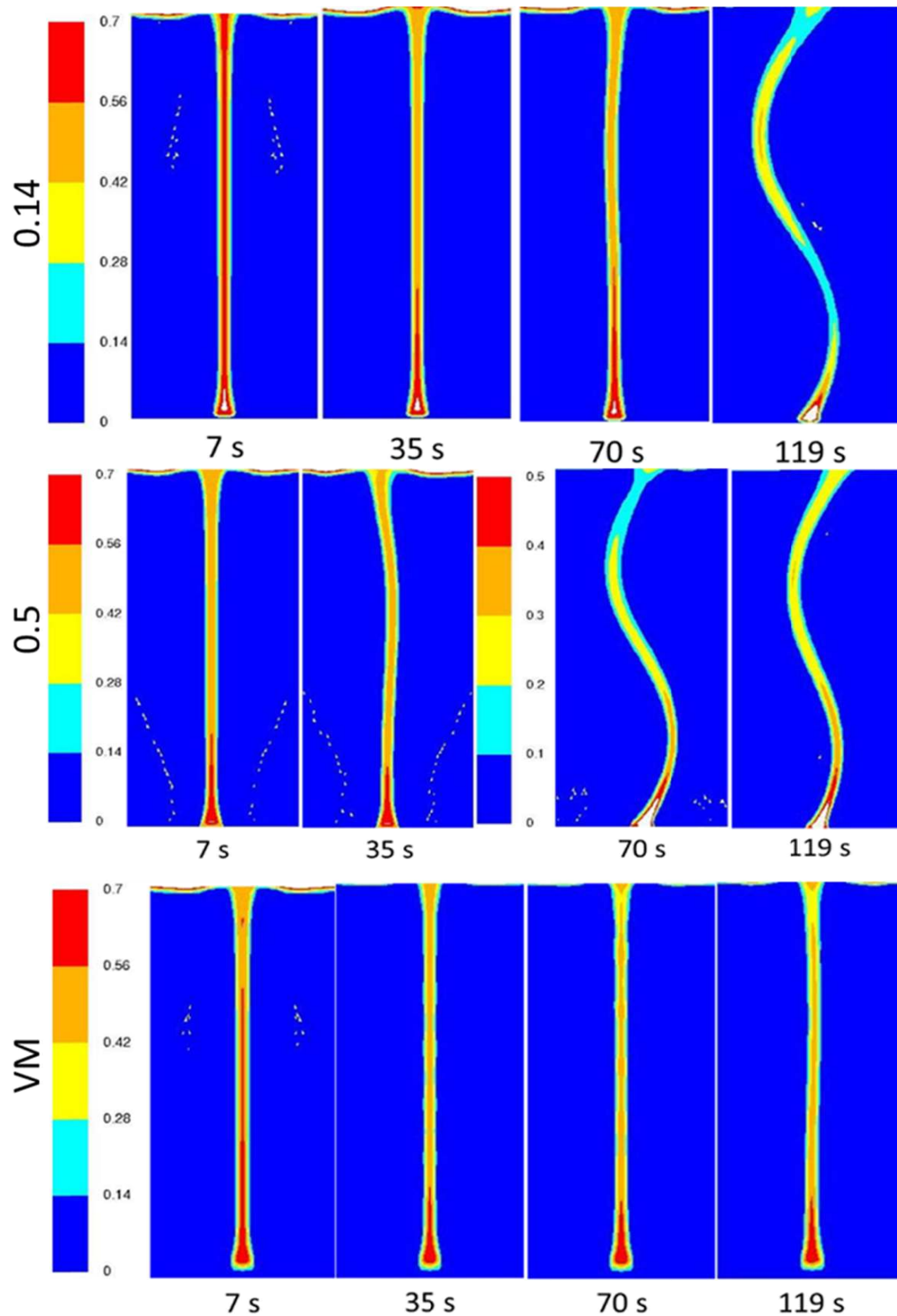


Figure 3.11a Instantaneous gas holdup contours of case studied, names are corresponding case is given on right of contour section.

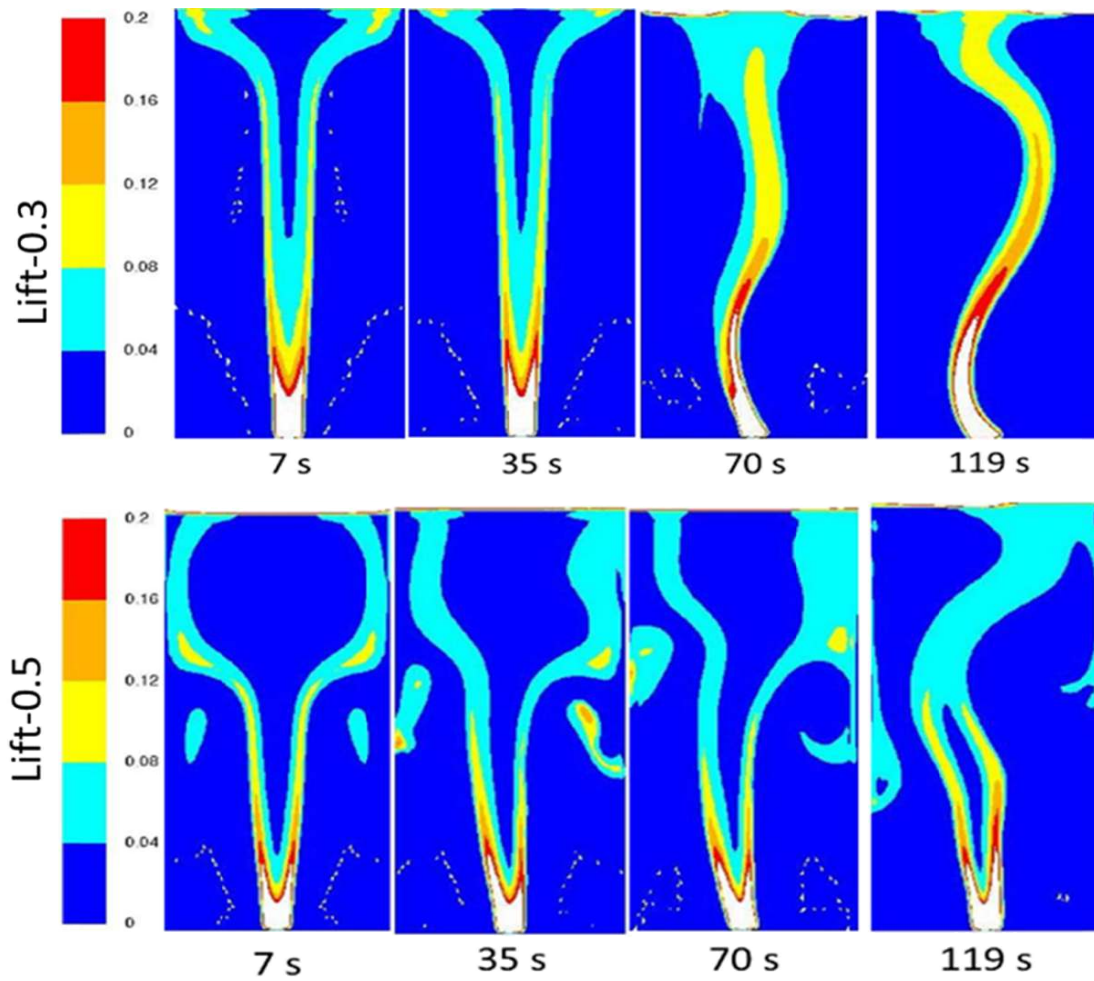


Figure 3.11b Instantaneous gas holdup contours of case studied, names are corresponding case is given on right of contour section.

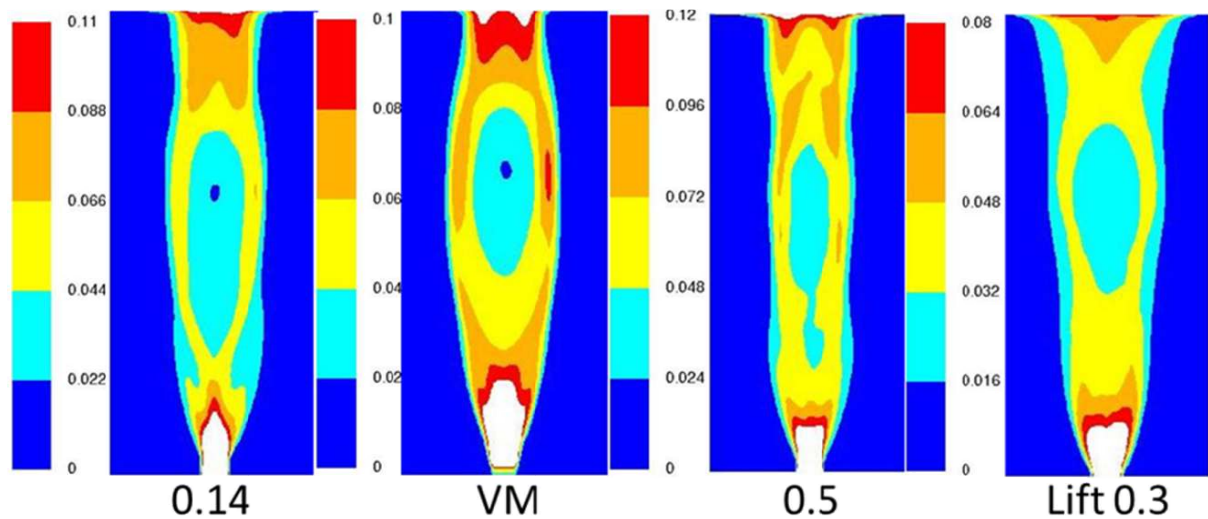


Figure 3.12 The time averaged gas holdup profile of cases, names are given in bottom of each.

3.4.1.1 Calculation of Plume Oscillation Period

The plume oscillation period is calculated from liquid horizontal velocity profile along flow time when the plume started to meander. The velocity was sampled every time step at the centre of the column at vertical height of 225 mm. The sampled liquid horizontal velocity profile of case lift-0.3 is shown in Figure 3.13(lower part) and comparison of the other three (excluding case lift-0.5) is shown in Figure 3.13(upper part). The average plume oscillation period as described by (Buwa et al., 2006) is 4-7 s. In our cases we have average time between 6-10 s (Table 3.5).

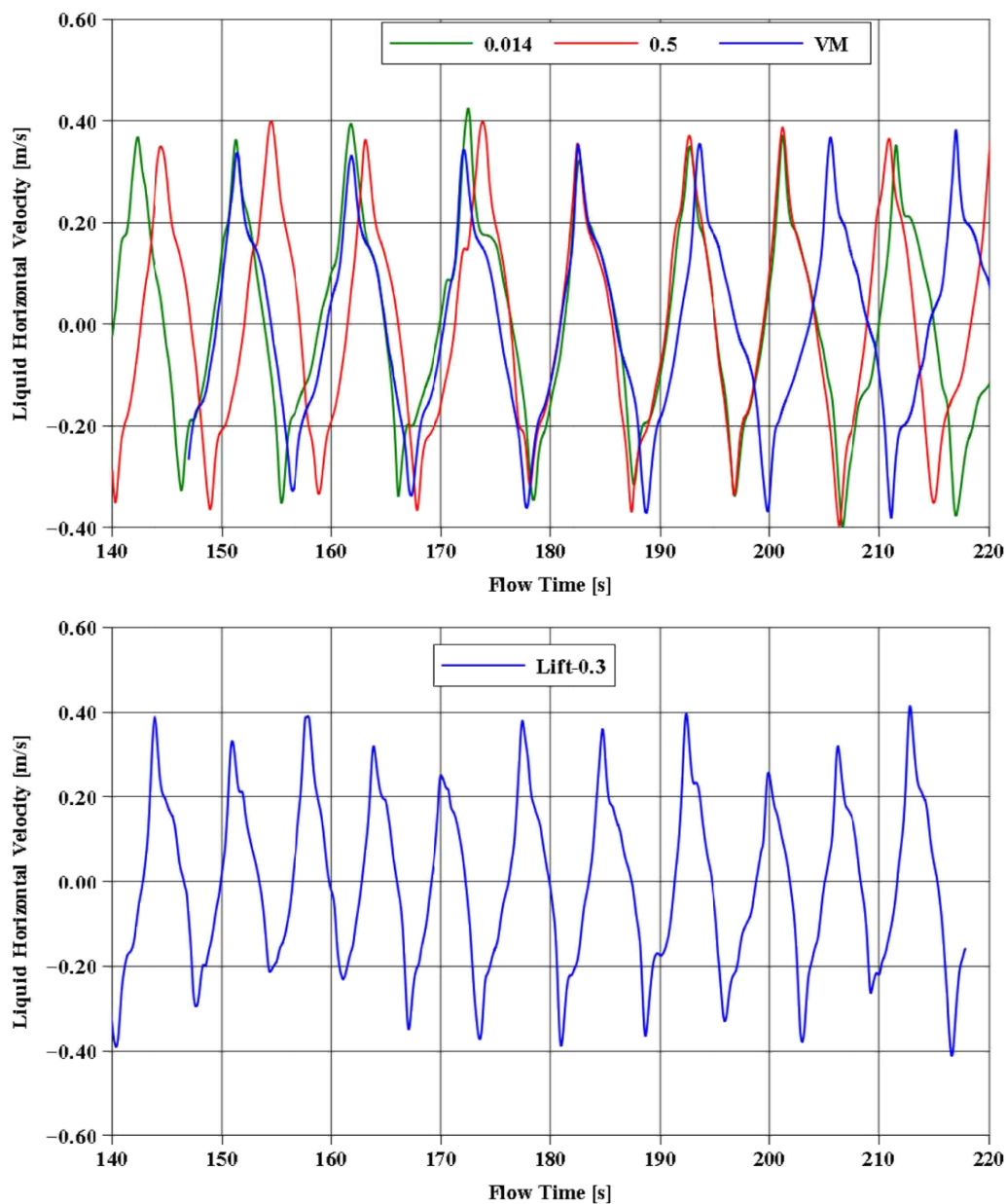


Figure 3.13 The profile of liquid horizontal velocity at centre point of column at height 225 mm from sparger. Upper one is for three cases named in legends and lower one is for case lift-0.3.

Table 3.5 Comparison of plume oscillation period of different cases with experimental and simulation results.

Case	Calculated Time	Simulation (Buwa and Ranade, 2002; Buwa et al., 2006)	Exp. wall pressure fluctuation (Buwa and Ranade, 2002; Buwa et al., 2006)
Case 0.14	10 s	5 s	7 s
Case 0.5	10 s		
VM	10 s		
Lift-0.3	6 s		

3.4.1.2 Liquid Axial Velocity and Gas Holdup

For all above cases, we calculated the time averaged liquid axial velocity and gas holdup profiles at horizontal line along width of column at vertical height of 370 mm from sparger, Figure 3.14 and 3.15. It is clear that, our first three cases 0.014, 0.5 and VM gave similar results while our case lift-0.3 gave best results as compared to experimental profile.

For our proposed model, application of lift in computational model is necessary to get good result with sufficient fine grid, like as case C grid in our case.

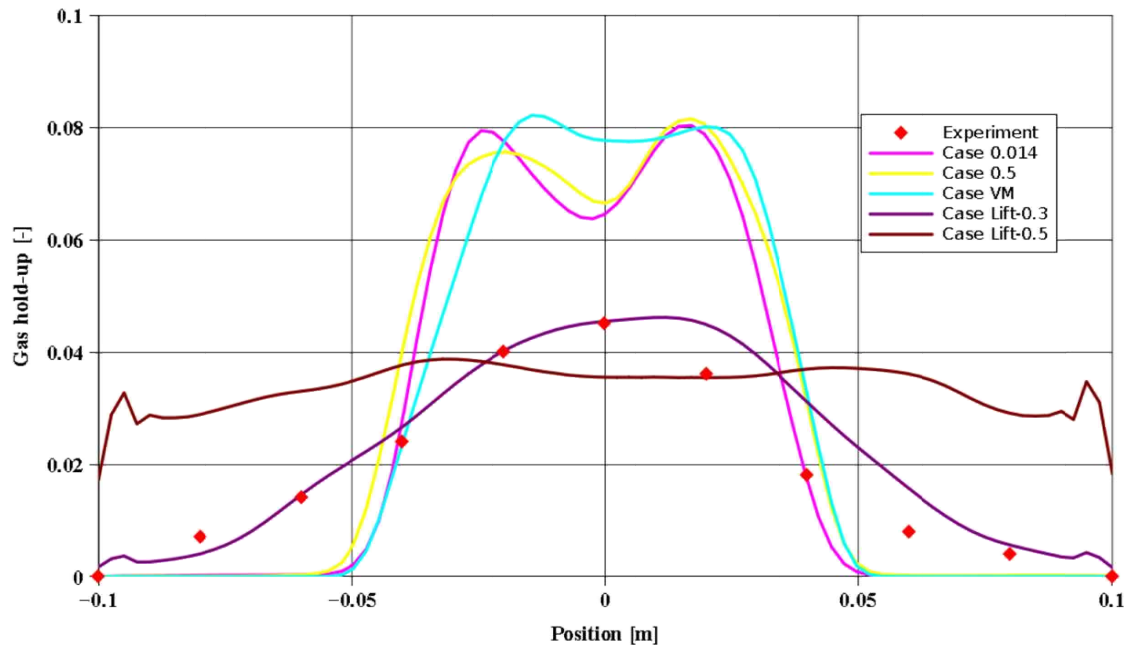


Figure 3.14 Time averaged gas holdup profile at horizontal line at vertical height 0.37 m from sparger. Experimental data is taken from (Buwa et al., 2006)

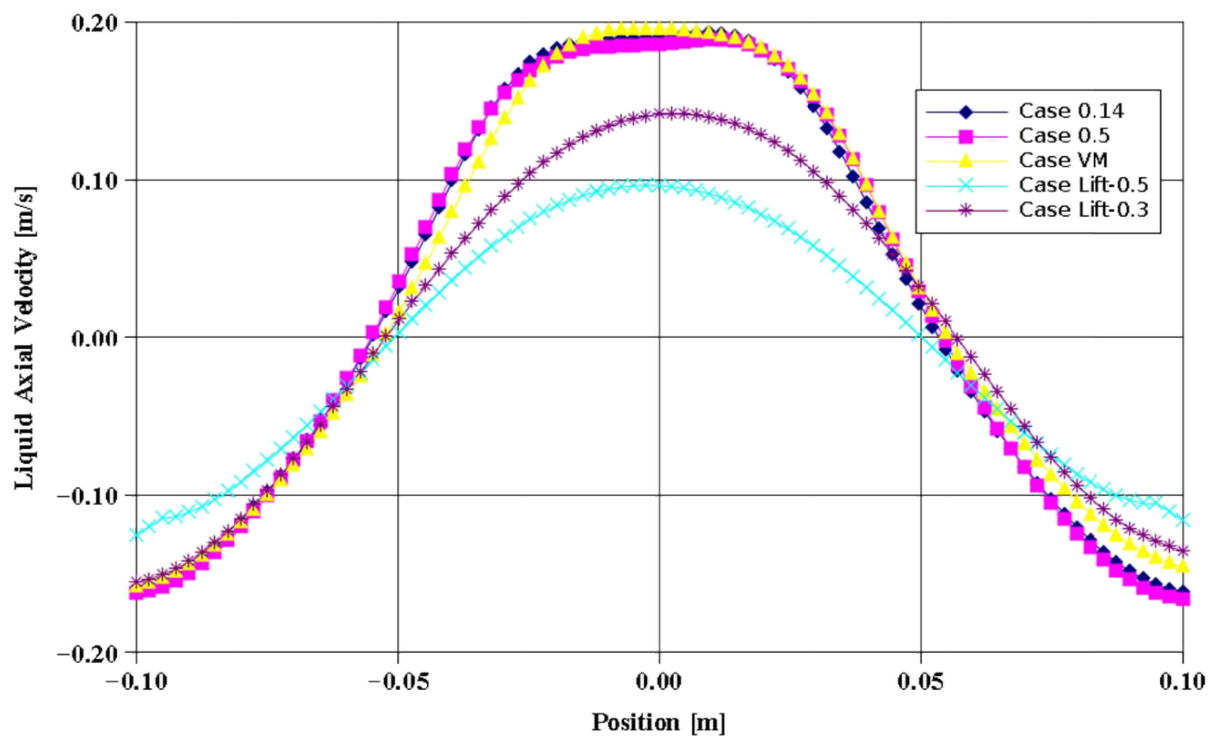


Figure 3.15 Time averaged liquid axial velocity profile at horizontal line at vertical height 0.37 m from sparger. Experimental data is not available; the profile is just for comparison purpose.

Chapter 4

Population Balance

4.1 Introduction

In previous chapters, we studied and explained numerically the hydrodynamics of bubble column reactor with fixed bubble sizes and similar shapes. In reality, there exist locally a large number of bubbles of different sizes and shapes in BCR, due to bubble-bubble interaction (gas holdup), pressure gradient (liquid-gas characteristics) and phase change (condensation or evaporation). To somehow, the study with fixed bubble size is appropriate in narrow range of operating conditions and geometry but not in all cases and we need the local bubble size information for industrial scale BCR systems. For better understanding of the BCR hydrodynamics, it is suitable to incorporate the population balance equation model in simulation with appropriate modelling of coalescence and breakage processes.

In this chapter, we will discuss the population balance equation model (PBE) with main focus on gas-liquid systems, solution methods for PBE, and the quadrature methods of moments (QMOM) in detail. For modelling of bubble distributions the number density function (NDF) is used which account for the bubble population in an infinitesimal control volume.

4.2 Population Balance Equation

The dispersed phase of BCR (for gas-liquid system) is composed of gas bubbles as discrete elements. These discrete elements may have interaction with each other or with the continuous liquid phase and each element can be identified with certain properties. In the population balance the properties are normally described by coordinates with classification into internal coordinates (ξ) for intimate properties of discrete element (volume, composition and temperature etc.), and external coordinates (\mathbf{x}) for spatial position in physical space. The NDF describes the population of all discrete elements in an infinitesimal

volume with these coordinates. The definition of NDF ($n_\xi(\xi; \mathbf{x}, t)$) is based on this expression:

$$n_\xi(\xi; \mathbf{x}, t) d\mathbf{x} d\xi, \quad (4.1)$$

which represents the number of total discrete elements inside the physical volume $d\mathbf{x}$ with internal coordinates $d\xi$ space at time t . If the population of bubbles is described by only one internal property/coordinate, for example length of the particle, (i.e., $\xi = L$), then the NDF is called monovariate. With two internal properties, it is called bivariate, and with more than two, it is called multivariate. If Ω_x represents the physical space of a generic control volume and Ω_ξ the internal coordinate space, then the population balance equation for the number density function on a defined control volume is:

$$\begin{aligned} \frac{\partial}{\partial t} \left(\int_{\Omega_x} d\mathbf{x} \int_{\Omega_\xi} d\xi n_\xi \right) + \int_{\Omega_\xi} d\xi \int_{\partial\Omega_x} (n_\xi \mathbf{v}) \cdot d\mathbf{A}_x \\ + \int_{\Omega_x} d\mathbf{x} \int_{\partial\Omega_\xi} (n_\xi \xi) \cdot d\mathbf{A}_\xi = \int_{\Omega_x} d\mathbf{x} \int_{\Omega_\xi} d\xi h_\xi \end{aligned} \quad (4.2)$$

The first term represents the accumulation rate of the number of elements in the control volume. The second term is for the net flux of the number density function due to advection in physical space and $d\mathbf{A}_x$ indicates the infinitesimal surface unit vector, \mathbf{v} is the advection velocity vector of the discrete phase, ξ is the rate of change in internal coordinate space. Explanation of third term is similar to second term, with advection in phase space. In last term, h_ξ summarises the physical phenomena for change in the number of elements. Since n is a continuous function of both \mathbf{x} and ξ , we can write the surface integrals as volume integrals by applying Reynolds-Gauss theorem [Aris, 1962] to above equation (4.2):

$$\begin{aligned} \frac{\partial}{\partial t} \left(\int_{\Omega_x} d\mathbf{x} \int_{\Omega_\xi} d\xi n_\xi \right) + \int_{\Omega_x} d\mathbf{x} \int_{\Omega_\xi} d\xi \frac{\partial}{\partial \mathbf{x}} \cdot (n_\xi \mathbf{v}) \\ + \int_{\Omega_x} d\mathbf{x} \int_{\Omega_\xi} d\xi \frac{\partial}{\partial \xi} \cdot (n_\xi \xi) = \int_{\Omega_x} d\mathbf{x} \int_{\Omega_\xi} d\xi h_\xi \end{aligned} \quad (4.3)$$

with,

$$\frac{\partial}{\partial \mathbf{x}} = \left(\frac{\partial}{\partial x_1}, \frac{\partial}{\partial x_2}, \frac{\partial}{\partial x_3} \right), \quad \frac{\partial}{\partial \xi} = \left(\frac{\partial}{\partial \xi_1}, \dots, \frac{\partial}{\partial \xi_N} \right).$$

where $\frac{\partial}{\partial \mathbf{x}}$ and $\frac{\partial}{\partial \xi}$ are the gradients in physical and internal coordinate spaces.

From equation (4.3), the population balance equation (PBE) can be derived (for detailed discussion see [Ramkrishna, 2000]):

$$\frac{\partial n_\xi}{\partial t} + \frac{\partial}{\partial \mathbf{x}} \cdot (n_\xi \mathbf{v}) + \frac{\partial}{\partial \xi} \cdot (n_\xi \xi) = h_\xi, \quad (4.4)$$

Which assume that all bubbles at a given spatial location and time have the same velocity \mathbf{v} . When the velocity of the dispersed phase is characterized as property coordinate of the NDF, $n(\xi, \mathbf{v}; \mathbf{x}, t)$ equation (4.4) becomes:

$$\frac{\partial n}{\partial t} + \frac{\partial}{\partial \mathbf{x}} \cdot (n \mathbf{v}) + \frac{\partial}{\partial \mathbf{v}} \cdot (n \mathbf{A}) + \frac{\partial}{\partial \xi} \cdot (n \xi) = h \quad (4.5)$$

Equation (4.5) is the generalized PBE (GPBE) Marchisio and Fox (2013). In equation (4.5), \mathbf{A} is the continuous rate of change of particle velocity due to external forces acting per unit mass on particles.

4.3 Bubble Breakage and Coalescence

In the previous section, we have considered a dispersed system in which the population of particles changed due to several processes and these processes can be applied through the boundary conditions of PBE with respect to property coordinates (internal). In other words, we can say that the birth of new particles or death of any particle is happened only at some boundary of internal coordinate space. These birth and death events are generally the result of breakage and/or coalescence processes. At first, we will discuss about the general nature of these breakage and coalescence processes and then apply the results to gas-liquid systems. We will follow the following relation for net rate of production of particles due to an event:

$$h_i = h_i^+ - h_i^- \quad (4.6)$$

where h_i^+ represents the rate of formation of new particles due to the i^{th} event and similarly, h_i^- represents the rate of death/disappearance.

4.3.1 Birth and Death due to Breakage

The bubble breakage probability (breakage rate) term as a first-order process is normally described as:

$$b(\xi, \xi_c; \mathbf{x}, t) dt \quad (4.7)$$

where b is a frequency with units s^{-1} and the whole term is representation of the probability that the particle with property coordinates ξ in a fluid with physical state ξ_c , experiences a breakup process in the infinitesimal time-interval dt . Then, the number of particles disappearing per unit time and volume due to breakage:

$$h_b^-(\xi, \xi_c) = b(\xi, \xi_c) n(\xi). \quad (4.8)$$

The rate of birth of new particles due to breakage can be estimated from the probability of production of daughter particles with property coordinates ξ' , from a mother particle with property coordinates ξ , $N(\xi'|\xi)$. This function for birth of new particle due to breakage depends only on state of dispersed phase [Patrino et al., 2009; Marchisio and Fox, 2013]. The conditional probability density function:

$$\int_{\Omega_{\xi'}} P(\xi' | \xi) d\xi' = 1 \quad (4.9)$$

The daughter distribution function for the conditional number density function $N(\xi'|\xi)$, is as follows:

$$\int_{\Omega_{\xi'}} N(\xi' | \xi) d\xi' = \nu(\xi), \quad (4.10)$$

where ν is the total number of new particles formed by breakage process. From equations (4.9) and (4.10), the rate of formation of new particles due to breakage is as follows:

$$h_b^+(\xi, \xi_c) = \int_{\Omega_{\xi'}} N(\xi' | \xi) b(\xi' | \xi) n(\xi') d\xi' \quad (4.11)$$

The net breakage rate $h_b(\xi, \xi_c)$ is therefore, expressed as:

$$h_b(\xi, \xi_c) = h_b^+(\xi, \xi_c) - h_b^-(\xi, \xi_c) = \int_{\Omega_{\xi'}} N(\xi' | \xi) b(\xi' | \xi) n(\xi') d\xi' - b(\xi, \xi_c) n(\xi) \quad (4.12)$$

4.3.2 Birth and Death due to Coalescence

The frequency of coalescence between particles with coordinates $(\tilde{\mathbf{x}}, \tilde{\xi})$ and particles with coordinates (\mathbf{x}', ξ') is:

$$a(\tilde{\mathbf{x}}, \tilde{\xi}; \mathbf{x}', \xi'; \xi_c) dt \quad (4.13)$$

The important assumption for this frequency is the symmetry with respect to particle permutation:

$$a(\tilde{\mathbf{x}}, \tilde{\xi}; \mathbf{x}', \xi'; \xi_c) = a(\mathbf{x}', \xi'; \tilde{\mathbf{x}}, \tilde{\xi}; \xi_c) \quad (4.14)$$

The rate of production of new particles due to coalescence is as follows:

$$h_a^+(\tilde{\mathbf{x}}, \xi, \xi_c, t) = \frac{1}{M} \int_{\Omega_{\xi'}} \alpha(\tilde{\mathbf{x}}, \tilde{\xi}, \mathbf{x}', \xi', \xi_c) n(\tilde{\mathbf{x}}, \tilde{\xi}, t) n(\mathbf{x}', \xi', t) J(\tilde{\xi}, \xi) d\xi' \quad (4.15)$$

The detail of derivation of equation (4.15) is given by Buffo (2012). In equation(4.14), $(\tilde{\mathbf{x}}, \xi)$ is the state vector of new particle produced by coalescence of particles $(\tilde{\mathbf{x}}, \tilde{\xi})$ and (\mathbf{x}', ξ') , the integer M is the symmetry factor to avoid multiple particle counting and $J(\tilde{\xi}, \xi)$ is the Jacobian of the variable transformation relating the properties coordinate space before and after coalescence, defined as:

$$J(\tilde{\xi}, \xi) = \left| \frac{\partial \tilde{\xi}}{\partial \xi} \right| = \begin{vmatrix} \frac{\partial \tilde{\xi}_1}{\partial \xi_1} & \dots & \frac{\partial \tilde{\xi}_1}{\partial \xi_N} \\ \vdots & \ddots & \vdots \\ \frac{\partial \tilde{\xi}_N}{\partial \xi_1} & \dots & \frac{\partial \tilde{\xi}_N}{\partial \xi_N} \end{vmatrix} \quad (4.16)$$

where N is the total number of properties coordinates.

The rate of loss of particles due to coalescence is:

$$h_a^-(\tilde{\mathbf{x}}, \xi, \xi_c, t) = \int_{\Omega_{\xi}} \alpha(\tilde{\mathbf{x}}, \tilde{\xi}, \xi', \xi_c) n(\tilde{\mathbf{x}}, \tilde{\xi}, t) n(\tilde{\mathbf{x}}, \xi', t) d\xi' \quad (4.17)$$

The overall coalescence rate:

$$\begin{aligned} h_a(\tilde{\mathbf{x}}, \xi, \xi_c, t) &= h_a^+(\tilde{\mathbf{x}}, \xi, \xi_c, t) - h_a^-(\tilde{\mathbf{x}}, \xi, \xi_c, t) \\ &= \frac{1}{M} \int_{\Omega_{\xi}} \alpha(\tilde{\mathbf{x}}, \tilde{\xi}, \mathbf{x}', \xi', \xi_c) n(\tilde{\mathbf{x}}, \tilde{\xi}, t) n(\tilde{\mathbf{x}}, \xi', t) J(\tilde{\xi}, \xi) d\xi' \\ &\quad - \int_{\Omega_{\xi}} \alpha(\tilde{\mathbf{x}}, \tilde{\xi}, \xi', \xi_c) n(\tilde{\mathbf{x}}, \tilde{\xi}, t) n(\tilde{\mathbf{x}}, \xi', t) d\xi' \end{aligned} \quad (4.18)$$

4.3.3 Gas Liquid System

In this subsection, we will develop the PBE for gas-liquid system and describe the details of different bubbles breakage-aggregation/coalescence models. A gas-liquid system is considered as a dispersion of bubbles and each bubble can be characterized by its size L , composition ϕ_b and velocity \mathbf{U}_b etc. Based on these characteristics, the equation (4.1) on similar grounds and definitions can be written for dispersed gas-liquid systems as follows:

$$\hat{n}(L, \phi_b, \mathbf{U}_b; \mathbf{x}, t) dL d\phi_b d\mathbf{U}_b d\mathbf{x} \quad (4.19)$$

The generic moment of number density function (NDF):

$$M_{k,l,m}(\mathbf{x}, t) = \int_{\Omega_L} \int_{\Omega_{\phi_b}} \int_{\Omega_{\mathbf{U}_b}} L^k \phi_b^l \mathbf{U}_b^m \hat{n}(L, \phi_b, \mathbf{U}_b; \mathbf{x}, t) dL d\phi_b d\mathbf{U}_b d\mathbf{x} \quad (4.20)$$

The GPBE for gas-liquid system comparable with equation (4.5) is as follows:

$$\frac{\partial \hat{n}}{\partial t} + \frac{\partial}{\partial \mathbf{x}} (\hat{n} \mathbf{U}_b) + \frac{\partial}{\partial \mathbf{U}_b} (\hat{n} \mathbf{A}_b) + \frac{\partial}{\partial L} (\hat{n} \mathbf{G}) + \frac{\partial}{\partial \phi_b} (\hat{n} \phi_b) = \hat{h}(L, \phi_b, \mathbf{U}_b; \mathbf{x}, t), \quad (4.21)$$

The definitions of different terms in equation (4.21) are similar as terms in equations (4.4) and (4.5): the left hand side represents the discontinuous events. In order to reduce the number of property coordinates, if we assume that, the bubble velocity \mathbf{U}_b does not affect advection terms of phase space then (4.21) can be written as:

$$\frac{\partial n}{\partial t} + \frac{\partial}{\partial \mathbf{x}}(n \tilde{\mathbf{U}}_b) + \frac{\partial}{\partial L}(n \mathbf{G}) + \frac{\partial}{\partial \phi_b}(n \phi_b) = h(L, \phi_b), \quad (4.22)$$

Where $\tilde{\mathbf{U}}_b$ is described as follows:

$$\tilde{\mathbf{U}}_b(L, \phi_b) = \frac{\int_{\Omega_{\mathbf{U}_b}} \hat{n}(L, \phi_b, \mathbf{U}_b; \mathbf{x}, t) \mathbf{U}_b d\mathbf{U}_b}{\int_{\Omega_{\mathbf{U}_b}} \hat{n}(L, \phi_b, \mathbf{U}_b; \mathbf{x}, t) d\mathbf{U}_b}, \quad (4.23)$$

representing the average bubble velocity with condition over the bubble size and composition. Equation (4.22) is the continuity equation for spatial inhomogeneous systems for bivariate NDF after integrating out the \mathbf{U}_b described in equation (4.20). For spatial homogeneous systems, the second term of equation (4.22) will vanish:

$$\frac{\partial n}{\partial t} + \frac{\partial}{\partial L}(n \mathbf{G}) + \frac{\partial}{\partial \phi_b}(n \phi_b) = h(L, \phi_b), \quad (4.24)$$

4.3.3.1 Discontinuous Events Modelling (Coalescence and Breakage)

In this section; we will give details of the available models for breakage and coalescence for gas-liquid systems, the right hand side term of equation (4.22). We have:

$$\begin{aligned} h(L, \phi_b) = & \frac{1}{2} \int_0^L \int_0^{\phi_b} \alpha(L^3 - \lambda^3)^{\frac{1}{3}} n \left((L^3 - \lambda^3)^{\frac{1}{3}}, \phi_b - \phi_{b,\lambda} \right) \\ & \times n(\lambda, \phi_{b,\lambda}) \frac{L^2}{(L^3 - \lambda^3)^{\frac{2}{3}}} d\lambda d\phi_{b,\lambda} - \\ & n(L, \phi_b) \int \int_0^\infty \alpha(L, \lambda) n(\lambda, \phi_{b,\lambda}) d\lambda d\phi_{b,\lambda} + \\ & \int_L^\infty \int_{\phi_b}^\infty \beta(\lambda) P(L, \phi_b | \lambda, \phi_{b,\lambda}) n(\lambda, \phi_{b,\lambda}) d\lambda d\phi_{b,\lambda} - \\ & \beta(L) n(L, \phi_b), \end{aligned} \quad (4.25)$$

The coalescence kernel, the breakage kernel and daughter bubble distribution function are represented by α , β and P , respectively.

4.3.3.1.1 Breakage Frequency and Daughter Distribution Functions

When bubbles are in turbulent dispersion, then the phenomena of bubble breakage is a balance between breakage/deformation forces and stabilization/restoration forces. The breakage models of Luo and Svendsen (1996) and Martinez-Bazan et al. (1999) are shown in figure 4.1. For liquid-liquid systems the groups of Narsimhan et al. (1979) and Lee et al. (1987), proposed the following model for drop breakage:

$$\beta(V_L) = C_1 \varepsilon^{1/3} L^{-2/3} \left[\frac{1}{L} \int_0^L 1 - F(X_c) d\lambda \right], \quad (4.26)$$

where left hand side of equation represents the breakage frequency of bubble with volume V_L and diameter L . $F(X_c)$ is Chi-squared distribution function and X_c is defined as:

$$X_c = C_2 \frac{\sigma L^2}{\rho_c \varepsilon^{2/3}} \lambda^{-11/3} \quad (4.27)$$

where parameters C_1 in equation (4.26) and C_2 in equation (4.27) are obtained through experiments.

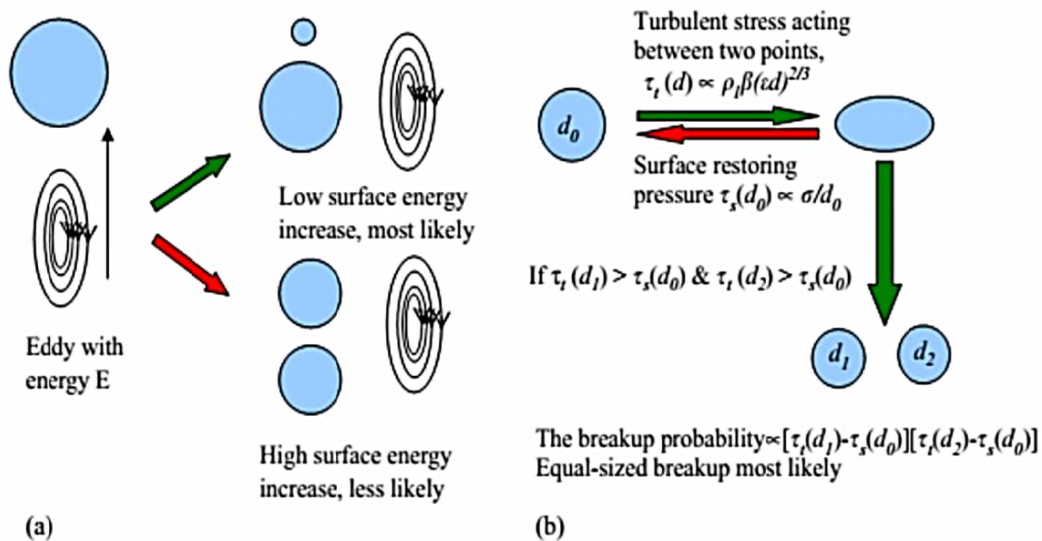


Figure 4.1 Breakage model illustrations (a) Luo and Svendsen (1996), (b) Martinez-Bazan (1999)

Alopaeus et al. (2002) and co-workers extended the model of Narsimhan, introducing a new term for considering viscous force that oppose the breakage process:

$$\beta(L) = C_1 \varepsilon^{1/3} \operatorname{erfc} \left[\sqrt{C_2 \frac{\sigma}{\rho_c \varepsilon^{2/3} L^{5/3}} + C_3 \frac{\mu_d}{\sqrt{\rho_c \rho_d} \varepsilon^{1/3} L^{4/3}}} \right] \quad (4.28)$$

where C_1 , C_2 and C_3 are fitting parameters and subscripts, c and d for for continuous phase and for dispersed phase, respectively. For gas-liquid system, Laakkonen et al. (2006) modified the above correlation for breakage kernel as follows:

$$\beta(L) = C_1 \varepsilon^{1/3} \operatorname{erfc} \left[\sqrt{C_2 \frac{\sigma}{\rho_c \varepsilon^{2/3} L^{5/3}} + C_3 \frac{\mu_c}{\sqrt{\rho_c \rho_d} \varepsilon^{1/3} L^{4/3}}} \right] \quad (4.29)$$

The breakage kernel for binary bubble breakage, formulated by Luo and Svendsen (1996):

$$\beta(V_L) = C_1 (1 - \alpha_d) \left(\frac{\varepsilon}{L^2} \right)^{1/3} \int_{\zeta_{\min}}^1 \frac{(1 + \zeta)^2}{\zeta^{11/3}} \exp \left[-\frac{C_2 \sigma C_f(f)}{\rho_c \varepsilon^{2/3} L^{5/3} \zeta^{11/3}} \right] d\zeta, \quad (4.30)$$

where α_d is the dispersed phase's volume fraction, $\zeta = \lambda_e / L$ is the ratio of the dimension of eddies large enough to break the bubble and size of bubble, the C_f is as follows:

$$C_f(f) = f^{2/3} + (1 - f)^{2/3} - 1, \quad (4.31)$$

and f describes the relation between the volumes of mother bubble and daughter bubble. The ζ_{\min} is the minimum eddies size as defined by Kolmogorov scale:

$$\zeta_{\min} = \frac{\lambda_{e,\min}}{L} = \frac{11.4}{L} \left(\frac{\mu_c^3}{\rho_c^3 \varepsilon} \right)^{1/4} \quad (4.32)$$

C_1 and C_2 are the fitting parameters calculated using experiments.

Lehr et al. (2002) proposed the following model without any fitting parameters for gas-liquid BCR:

$$\beta(L) = \frac{1}{2} \frac{L^{5/3} \rho_c^{7/5} \varepsilon^{19/15}}{\sigma^{7/5}} \exp \left(-\sqrt{2} \frac{L^3 \varepsilon^{6/5} \rho_c^{9/5}}{\sigma^{9/5}} \right) \quad (4.33)$$

Now we will present the daughter distribution function models that will describe the prediction of number of generating bubbles.

Lehr et al. (2002) proposed the following model for binary breakage:

$$P(V_L | V_\lambda) = \begin{cases} \frac{6}{\pi^{3/2} L^3} \frac{\exp\left[-\frac{9}{4} \left[\ln\left(2^{2/5} \left(\frac{L \rho_c^{3/5} \varepsilon^{2/5}}{\sigma^{3/5}}\right)\right)\right]^2\right]}{1 + \operatorname{erf}\left[\frac{3}{2} \left(2^{1/15} \left(\frac{\lambda \rho_c^{3/5} \varepsilon^{2/5}}{\sigma^{3/5}}\right)\right)\right]} & \text{with } 0 \leq V_L \leq \frac{V_\lambda}{2}; \\ P(V_L - V_\lambda, V_\lambda) & \text{with } \frac{V_\lambda}{2} \leq V_L \leq V_\lambda. \end{cases} \quad (4.34)$$

This model was successfully used with for the experimental study of BCR with breakage kernel equation (4.33), [Lehr et al., 2002].

Luo and Svendsen (1996) proposed the following model:

$$P(V_L | V_\lambda) = \frac{2 \int_{\zeta_{\min}}^1 (1 + \zeta)^2 \zeta^{-11/3} \exp(-x_c) d\zeta}{\nu_L \int_0^1 \int_{\zeta_{\min}}^1 (1 + \zeta)^2 \zeta^{-11/3} \exp(-x_c) d\zeta df} \quad (4.35)$$

Finally Laakkonen et al. (2006), proposed a simple model based on statistical distribution:

$$P(L | \lambda) = N_f \left(9 + \frac{33}{2} C + 9C^2 + \frac{3}{2} C^3\right) \left(\frac{L^2}{\lambda^3}\right) \left(\frac{L^3}{\lambda^3}\right)^2 \left(1 - \frac{L^3}{\lambda^3}\right)^C, \quad (4.36)$$

where L and λ are respectively, the size of the daughter and mother bubbles, and $N_f = 4/3 + C/3$ is a factor based on following conditions:

$$\begin{cases} \int_0^\infty P(L | \lambda) dL = N_f \\ \int_0^\infty P(L | \lambda) L^3 dL = \lambda^3. \end{cases} \quad (4.37)$$

4.3.3.1.2 Coalescence Kernel

The coalescence of two bubbles is composed of three steps; bubble approach, drainage of liquid film and breakage of liquid film. The basic mechanism is shown in Figure 2.

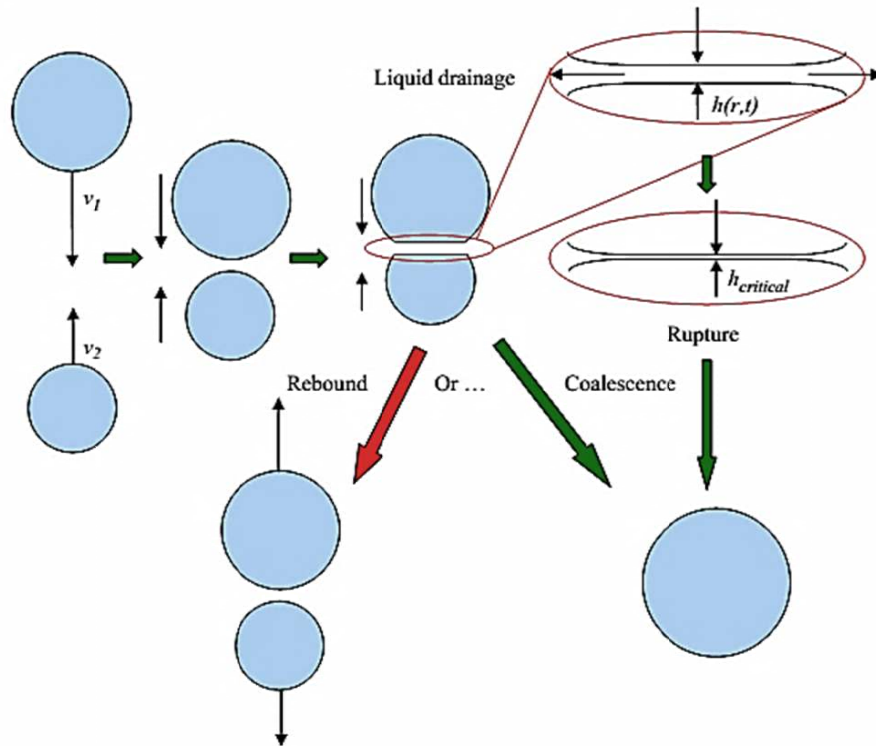


Figure 4.2 Bubble coalescence mechanisms in turbulent fluid (Chen, 2005).

The collision of bubbles is due to external forces and a layer of liquid is trapped in the form of film. The drainage of this film is the controlling step and decisive for coalescence to occur after collision. In this step drainage of liquid up to the critical thickness is must to rapture the remaining film thickness.

Bubble coalescence kernel models, must provide two pieces of information, one is the frequency of collision and the second one is the efficiency of the collision because coalescence may not occur from every collision. (Jakobsen, 2008; Marchisio and Fox, 2013).

In analogy of kinetic theory of gases (Marchisio and Fox, 2013), the coalescence kernel for two bubbles, of sizes λ and L can be given as:

$$\alpha(\lambda, L, U_r) = \frac{\pi}{4} (\lambda + L)^2 |U_r| \eta(U_r) \quad (4.38)$$

where the first term is the collision cross section, the second term quantifies the relative velocity of colliding bubbles, last term ($\eta(U_r)$) is the collision efficiency.

A coalescence kernel based on isotropic turbulence theory, was proposed by Coualoglou and Tavlarides (1977):

$$\alpha(\lambda, L) = C_1 \varepsilon^{1/3} (\lambda + L)^2 (\lambda^{2/3} + L^{2/3})^{1/2} \eta(\lambda, L), \quad (4.39)$$

where C_1 is the constant of model, ε is the local turbulent dissipation rate and coalescence efficiency is as follows:

$$\eta(\lambda, L) = \exp\left(-C_2 \sqrt{\frac{2\rho_c \varepsilon^{2/3}}{\sigma} \frac{\lambda L}{\lambda + L}}\right) \quad (4.40)$$

Prince and Blanch (1990), gave the following formulation for coalescence efficiency with assumption that during liquid drainage between bubbles, their surfaces are stationary:

$$\eta(\lambda, L) = \exp\left(-C_2 \frac{\mu_c \rho_c \varepsilon}{\sigma^2} \left(\frac{\lambda L}{\lambda + L}\right)^4\right) \quad (4.41)$$

4.4 Solution Methods

In this section we will give brief overview of the PBE solution methods and detail of quadrature methods of moments (QMOM). The solution methods for PBE can be classified based on the solution strategy adopted; mainly, there are three groups of methods for solving the PBE: classes or sectional, Monte Carlo and moment-based methods. In Classes Methods (CM), the PBE is solved by discretizing internal coordinates space: these were initially developed for the solution of monovariate cases, in which the state of the population is characterized by one property or variable (Kostoglou and Karabelas, 1994; Vanni, 2000) and were recently extended to multivariate cases, in which two or more variables are needed to describe the disperse system (Kumar et al., 2008; Nandanwar and Kumar, 2008). The main drawback of these methods is the high computational costs to get accurate results when the inhomogeneities in the physical space are taken into account. Finite Volume Methods (Gunawan et al., 2004) and Finite Element Methods (Godin et al., 1999) belong to the group of CM and hence they, too, have the same limitations in application to the realistic inhomogeneous systems.

Monte Carlo Methods (MCM) are based on the solution of stochastic differential equations, which are able to reproduce a finite number of artificial

realizations of the system (Zhao et al., 2007). However, the computational cost is also high for realistic systems with these methods, therefore; these methods are usually used for validation of simplified cases (Zucca et al., 2007).

The Method of Moments (MOM) was first formulated and applied to particulate systems by Hulburt and Katz (1964). In MOM the PBE are represented in terms of transport equations of the moments of the bubble distribution. For realistic processes, it is not always possible to write the governing equations in terms of the moments themselves, many closures were proposed in order to overcome closure problem. In order to overcome the closure problem, a different approach for computing the moment is to approximate the integrals using the numerical quadrature scheme, the quadrature methods of moments (QMOM) as suggested by (McGraw, 1997; Marchisio et al., 2003b) extended the method by developing the direct QMOM where the quadrature abscissa and weights are formulated as transport equations; they are solved directly using matrix operation. Methods of moments (MOM) have low computational costs as compared to others numerical methods for solving PBE and can be coupled with CFD for prediction of industrial scale systems with economical computational costs (Zucca et al., 2007; Buffo et al., 2013).

The general definition of generic-order moment, as expressed in equation (4.19) and (4.20):

$$M_{k,l}(\mathbf{x}, t) = \int \int_0^\infty n(L, \phi_b; \mathbf{x}, t) L^k d\phi_b^l dL d\phi_b, \quad (4.42)$$

$$M_{k,l}(\mathbf{x}, t) = \int_0^\infty \tilde{n}(L; \mathbf{x}, t) L^k dL, \quad (4.43)$$

After applying the moments transform for all the terms in equation (4.22), we have:

$$\begin{aligned} \frac{\partial M_{k,l}}{\partial t} = & -\frac{\partial}{\partial \mathbf{x}} (M_{k,l} \tilde{\mathbf{U}}_{k,l}) + \int_0^\infty kL^k G(L, \phi_b) n(L, \phi_b) dL \\ & + \int_0^\infty l\phi_b^l \dot{\phi}_b (L, \phi_b) n(L, \phi_b) d\phi_b + H_{k,l}, \end{aligned} \quad (4.44)$$

where the generic moment's velocity $\tilde{\mathbf{U}}_{k,l}$ and the collisional term $H_{k,l}$ are as follows:

$$\tilde{\mathbf{U}}_{k,l} = \frac{\int \int_0^\infty \tilde{\mathbf{U}}_b(L, \phi_b) n(L, \phi_b) L^k \phi_b^l dL d\phi_b}{\int \int_0^\infty n(L, \phi_b) L^k \phi_b^l dL d\phi_b} \quad (4.45)$$

$$H_{k,l} = \int \int_0^\infty h(L, \phi_b) L^k \phi_b^l dL d\phi_b. \quad (4.46)$$

For close spatially homogeneous system, the equation (4.44) will become after vanishing the spatial gradient:

$$\begin{aligned} \frac{\partial M_{k,l}}{\partial t} &= \int_0^\infty k L^k G(L, \phi_b) n(L, \phi_b) dL \\ &+ \int_0^\infty l \phi_b^l \dot{\phi}_b(L, \phi_b) n(L, \phi_b) d\phi_b + H_{k,l}, \end{aligned} \quad (4.47)$$

For the monivariate PBE, we can write in analogy of PBE bivariate case discussed as above: the monivariate PBE transport equation for homogeneous and inhomogeneous systems respectively:

$$\frac{dM_k}{dt} = \int_0^\infty k L^k G(L) n(L) dL + H_k, \quad (4.48)$$

$$\frac{\partial M_k}{\partial t} = -\frac{\partial}{\partial \mathbf{x}} (M_k \tilde{\mathbf{U}}_k) + \int_0^\infty k L^k G(L) n(L) dL + H_k \quad (4.49)$$

And for the monivariate systems generic moment's velocity $\tilde{\mathbf{U}}_k$ and the collisional term H_k are as follows:

$$\tilde{\mathbf{U}}_k = \frac{\int_0^\infty \tilde{\mathbf{U}}_b(L) n(L) L^k dL}{\int_0^\infty n(L) L^k dL} \quad (4.50)$$

$$H_k = \int_0^\infty h(L) L^k dL. \quad (4.51)$$

The equations (4.44), (4.47) and (4.48) are not closed as the functional form of NDF in general form is unknown. This is the inherent closure problem as discussed by Hulburt and Katz (1964). One of the closures (QMOM approach) was proposed with assumption of the functional form of the NDF as a summation of delta functions centred on nodes of Gaussian quadrature approximation (McGraw, 1997). By using this approach one can write the following expressions for bivariate case:

$$n(L, \phi_b) = \sum_{i=1}^N \omega_i \delta(L - L_i) \delta(\phi_b - \phi_{b,i}), \quad (4.52)$$

and for the monovariate case:

$$n(L) = \sum_{i=1}^N \omega_i \delta(L - L_i), \quad (4.53)$$

The quadrature approximation closure as given by equations (4.52) and (4.53), we are now in position to address the closure issue of the terms of (4.44) and (4.48) with the function of N quadrature weights and nodes. The collisional term in equation(4.25) after applying the moment transformation, we may write:

$$\begin{aligned} H_{k,l} = & \frac{1}{2} \sum_{i=1}^N \sum_{j=1}^N \alpha(L_i, L_j) \omega_i \omega_j \left[(L_i^3 + L_j^3)^{k/3} (\phi_{b,i} + \phi_{b,j})^l - L_i^k \phi_{b,i}^l - L_j^k \phi_{b,j}^l \right] \\ & + \sum_{i=1}^N \beta(L_i) \omega_i (\bar{P}_{k,l}^{(i)} - L_i^k \phi_{b,i}^l) \end{aligned} \quad (4.54)$$

The term $\bar{P}_{k,l}^{(i)}$ is the generic order term for the daughter distribution function and is as follows:

$$\bar{P}_{k,l}^{(i)} = \int_{\Omega_L} \int_{\Omega_{\phi_b}} L^k \phi_b^l P(L_i, \phi_{b,i} | \lambda, \phi_{b,\lambda}) dL d\phi_b, \quad (4.55)$$

For monovariate case on similar order as above:

$$\begin{aligned} H_k = & \frac{1}{2} \sum_{i=1}^N \sum_{j=1}^N \alpha(L_i, L_j) \omega_i \omega_j \left[(L_i^3 + L_j^3)^{k/3} - L_i^k - L_j^k \right] \\ & + \sum_{i=1}^N \beta(L_i) \omega_i (\bar{P}_k^{(i)} - L_i^k) \end{aligned} \quad (4.56)$$

4.4.1 Quadrature Method of Moments

Quadrature method of moments (QMOM) was proposed by McGraw (1997) for dispersed systems, in which the exact closure of NDF is replaced by an approximate closure condition. This is defined for a monovariate case, and given in following equation by substituting equation (4.53) in(4.43):

$$M_k = \sum_{i=1}^N \omega_i L_i^k \quad (4.57)$$

This is the k-order moment, quadrature function of N weights and nodes. The procedure, which express the quadrature weights and nodes into a function of

moments is called inversion algorithm (McGraw, 1997; Marchisio et al., 2003b), for this we have the determination procedure for weights and nodes after solving the following non-linear system:

$$\left\{ \begin{array}{l} M_0 = \sum_{i=1}^N \omega_i \\ M_1 = \sum_{i=1}^N \omega_i L_i \\ \dots \\ M_{2N-1} = \sum_{i=1}^N \omega_i L_i^{2N-1} \end{array} \right. \quad (4.58)$$

The non-linear system (4.58), can be solved with a non-linear solver but ensured convergence is needed. For this we will present following stable procedure.

The NDF, according to quadrature theory should be positive and non-zero in the integration interval and all its moments must exist (Gautschi, 2004; Press et al., 2007; Marchisio and Fox, 2013). The definition of orthogonal polynomials (Gautschi, 2004):

$$\begin{aligned} & \{P_0(L), P_1(L), \dots, P_i(L)\} \\ & \text{with } P_i(L) = k_{i,0}L^i + k_{i,1}L^{i-1} + \dots + k_{i,i} \end{aligned} \quad (4.59)$$

The equation (4.59) is orthogonal in the Ω_L (interval of integration), as per the measure function $n(L)$, if

$$\int_{\Omega_L} n(L) P_\alpha(L) P_\beta(L) dL \begin{cases} = 0 & \text{for } \alpha \neq \beta \\ > 0 & \text{for } \alpha = \beta \end{cases} \quad (4.60)$$

The outcome of this is; integration domain Ω_L and the weight function $n(L)$, define the family of orthogonal polynomials such that:

$$P_{i+1}(L) = (L - a_i)P_i(L) - b_i P_{i-1}(L) \quad \text{with } i = 0, 1, 2, \dots \quad (4.61)$$

with $P_{-1}(L) = 0$, $P_0(L) = 1$ and

$$a_N = \frac{\int_{\Omega_L} L n(L) P_i(L) P_i(L) dL}{\int_{\Omega_L} n(L) P_i(L) P_i(L) dL} \quad \text{with } i = 0, 1, 2, \dots \quad (4.62)$$

$$b_N = \frac{\int_{\Omega_L} n(L) P_i(L) P_i(L) dL}{\int_{\Omega_L} n(L) P_{i-1}(L) P_{i-1}(L) dL} \quad \text{with } i = 0, 1, 2, \dots \quad (4.63)$$

The equation (4.61) is the recurrence formula of the orthogonal polynomials and is for calculating the quadrature approximation. With this recurrence relation, it is possible to calculate the weights and nodes of quadrature (Gautschi, 2004; Wilf, 2011). The above relation, we can write in matrix form as follows:

$$L \begin{bmatrix} P_0(L) \\ P_1(L) \\ P_2(L) \\ \vdots \\ P_{N-1}(L) \end{bmatrix} = \begin{bmatrix} a_0 & 1 & & & \\ b_1 & a_1 & 1 & & \\ & b_2 & a_2 & 1 & \\ & & \ddots & \ddots & \ddots \\ & & & b_{N-1} & a_{N-1} \end{bmatrix} \begin{bmatrix} P_0(L) \\ P_1(L) \\ P_2(L) \\ \vdots \\ P_{N-1}(L) \end{bmatrix} + \begin{bmatrix} 0 \\ 0 \\ 0 \\ \vdots \\ P_N(L) \end{bmatrix} \quad (4.64)$$

And from the eigenvalues, to give the Jacobi matrix:

$$\mathbf{J} = \begin{bmatrix} a_0 & \sqrt{b_1} & & & & \\ \sqrt{b_1} & a_1 & \sqrt{b_2} & & & \\ & \sqrt{b_1} & a_2 & \sqrt{b_3} & & \\ & & \ddots & \ddots & \ddots & \\ & & & \sqrt{b_{n-1}} & a_{N-1} & \end{bmatrix} \quad (4.65)$$

The efficient methods for calculation of Jacobi matrix from moments are; the product-difference (PD) algorithm Gorden (1968) and Wheeler algorithm [Wheeler, 1974]. Although PD algorithm is efficient but the stability goes to decrease as the number of quadrature nodes N increases Marchisio and Fox (2013), on the other hand, the Wheeler algorithm is more stable than PD algorithm. The detail of Wheeler algorithm can be found in Wheeler (1974).

Chapter 5

Flow Simulation with Coalescence and Breakage

5.1 Introduction

CFD modelling of rectangular bubble columns to describe its hydrodynamics is normally carried out using the assumption of bubble population with fixed bubble size, as a parameter to estimate the global gas holdup (Pfleger and Becker, 2001). Bubble size distribution locally changes as a result of coalescence and breakup of bubbles and varies the values of gas-liquid interfacial area. The examples of recent study of coupled CFD-PBM approaches are: Buwa and Ranade (2002) who have used FLUENT for PBM by user-defined functions (UDF), Diaz et al. (2008) by using the commercial code CFX using the built-in population balance module including the non-uniform multi-group model, and recently Gupta (2012) by using FLUENT 14 with QMOM. Quadrature-Based Moment Methods have the advantage of reducing the computational cost as compared with other available solution methods.

In the present work we will discuss the numerical simulation of rectangular shaped bubble column reactor with QMOM population balance technique for air-water fluid system by using FLUENT 13 package. Two different gas flow rates, 48 L/h and 260 L/h are applied and their results are compared with available experimental data. The physical conditions and general geometry layout of the bubble column reactor (BCR) are same as used in Chapter 3, (Figure 3-1) with grid size $80 \times 19 \times 135$ (L \times W \times H). The chapter is divided in two sections; in the first section we carry out simulations with PBM using QMOM without breakage and coalescence phenomena. In second section we simulate system with breakage and coalescence and eventually, the simulation results are compared with experimental data taken from the scientific literature.

5.2 QMOM without Breakage and Coalescence Models

In this section, the bubble column was simulated with implementation of QMOM without breakage and coalescence. The main objectives in this section are the finalization of the boundary conditions for moments and assessment of the applicability of the adopted method for next section.

Four moments of the Bubble Size Distribution were calculated (m_0 , m_1 , m_2 and m_3) and these moments describe the following properties of population of particles per unit volume of mixture, defined as follows;

$$\begin{aligned} m_0 &= N_{\text{total}} \\ m_1 &= L_{\text{total}} \\ m_2 &= A_{\text{total}} / K_a \\ m_3 &= V_{\text{total}} / K_v \end{aligned} \quad (5.1)$$

and

$$d_{32} = \frac{m_3}{m_2},$$

where K_v and K_a are the area and volumetric shape factors equal to π and $\pi/6$ for a sphere, respectively and d_{32} is the Sauter mean diameter defined by ratio of third order and second order moment and used as mean of particle sizes. The inlet boundary condition for the Bubble Size Distribution was calculated by assuming a log-normal distribution as used by Petitti et al. (2010). The k -th order moment was calculated as follows:

$$m_k = m_0 \exp\left(k\mu + \frac{k^2\sigma^2}{2}\right) \quad (5.2)$$

where m_0 is the moment of order zero as defined in (5.1), the total number of bubbles per unit volume and μ and σ are the two parameters of the log-normal distribution.

The log-normal distribution parameters given in (5.2) can be calculated by adopting the method as used by Laakkonen et al. (2007); Petitti et al. (2010). Considering the mean m of the bubble distribution equal to the mean bubble diameter calculated near the sparger from the correlation of Geary and Rice (1991) and the standard deviation \sqrt{v} of the distribution equal to 15% of the mean, m , we can calculate μ and σ with the following relations:

$$\mu = \log\left(\frac{m^2}{\sqrt{\nu + m^2}}\right) \quad (5.3)$$

and

$$\sigma = \sqrt{\log\left(\frac{\nu}{m^2} + 1\right)} \quad (5.4)$$

The value of the moment of order zero m_0 can be calculated by considering the following equality:

$$\text{Gas vol.fraction} = k_v m_3 = k_v m_0 \exp\left(3\mu + \frac{9\sigma^2}{2}\right) \quad (5.5)$$

For this we defined three boundary conditions for moments with aim of obtaining uniform bubble size throughout the column from the simulation, due to the absence of coalescence and breakage. These boundary conditions are given in Table 5.1.

Table 5.1 Difference in boundary conditions for air moments

Name	Definition
Case 1	Moments flow through column defined based on inlet volume fraction as per (5.5). Inlet and outlet boundary conditions for moments, same values applied.
Case 2	Inlet and outlet boundary conditions for air moments values defined based on volume fraction of inlet and outlet (5.5).
Case 3	Inlet boundary condition for moments defined on volume fraction (5.5) and outlet boundary condition is taken as zero flux/value.

The simulation parameters are given in Table 5.2. Bubble column hydrodynamics was compared with experimental work and already modelled system in Chapter 3. We have following available experimental hydrodynamics data of used BCR geometry and flow rates:

1. Liquid axial velocity profile (Pfleger et al., 1999)
2. Plume oscillation period (Buwa and Ranade, 2002)
3. Gas holdup profile (Buwa et al., 2006)

Table 5.2 Definition of Simulation parameters for QMOM cases without coalescence and breakage models

Parameter	Definition
Inlet gas velocity V_{in}	Defined according to <i>GFR</i> 48 L/h or 260 L/h.
Gas Volume Fraction at inlet	0.014, based on the ratio of sparger holes area A_p per sparger cross sectional area A_t , A_p/A_t .
Bubble diameter at Sparger	Defined by Geary and Rice, (1999) Model <ul style="list-style-type: none"> • 6.06 mm for 48L/h • 8.49 mm for 260L/h
Inlet liquid velocity	0.0 m/s, the stagnant liquid level is maintained up to 450 mm.
Multiphase Model	Eulerian two phase
Viscous Model	Standard $k-\varepsilon$ per phase
Drag Coefficient	Defined on constant terminal velocity, 20cm/s or specified
Surface Tension	Constant: 0.071N/m
Pressure-Velocity coupling	Phase coupled SIMPLE
Discretization Scheme	QUICK or specified
Moments	First order upwind scheme, and at inlet BSD defined based on log-normal distribution. Four or six as will be specified, generic number of moments applied.
Transient formulation	First order implicit
Time Step	0.001 s and after 30s, 0.01s.
Grid Size (L×W×H)	80×19×135

5.2.1 Results and Discussion

Our simulations shows that in case of just transportation of moments without breakage and coalescence of bubbles through stagnant liquid, the suitable boundary condition for moments is the type of case 3, in which we have defined the moments order values at inlet with volume fraction and at outlet with zero gradient. The instantaneous contours of different cases for gas holdup, generic moments, (m_2 and m_3) and Sauter mean bubble diameter, d_{32} , are shown in Figure 5.1-5.3 for the boundary conditions of Table 5.1. It is clear from the contours that we have uneven profiles for higher gas flow rate (260 L/h) and for lower gas flow rate (48 L/h), there is not uniform Sauter mean diameter for all cases. For case 1 and case 2, the bubble size is larger near the walls of the column as compared to case 3. We adopted different simulation techniques to get our goal of uniform bubble size and will be explained after these results. The plume oscillation period was calculated by profile of liquid horizontal velocity at centre point of column at height 0.225 m from bottom. There is not much change in hydrodynamics of bubble column with bubble distribution function. However, as we have observed in results of Chapter 3, the interfacial lift force in combination of drag force is important and necessary for better hydrodynamics results. In these results, the applied different discretization scheme is giving non-uniform distribution for Sauter mean diameter. As we have already explained, there should be uniform bubble size in contours of Sauter mean diameter when we are applying just transport of moments but in the simulations of Figure 5.1-5.3, there is larger bubble size near the wall in the upper part of the column. In initial cases, we used the QUICK discretization scheme for momentum, volume fraction, turbulent kinetic energy and turbulent dissipation rate. In order to get uniform mean bubble size in the column, we checked and applied different simulation parameters but similar results obtained. In the end, we reached to final conclusion that change in the discretization scheme from QUICK to first order upwind provided the expected results. These results are shown in Figure 5.4 and for these cases we also changed the applied numbers of generic moments in the QMOM from 4 to 6.

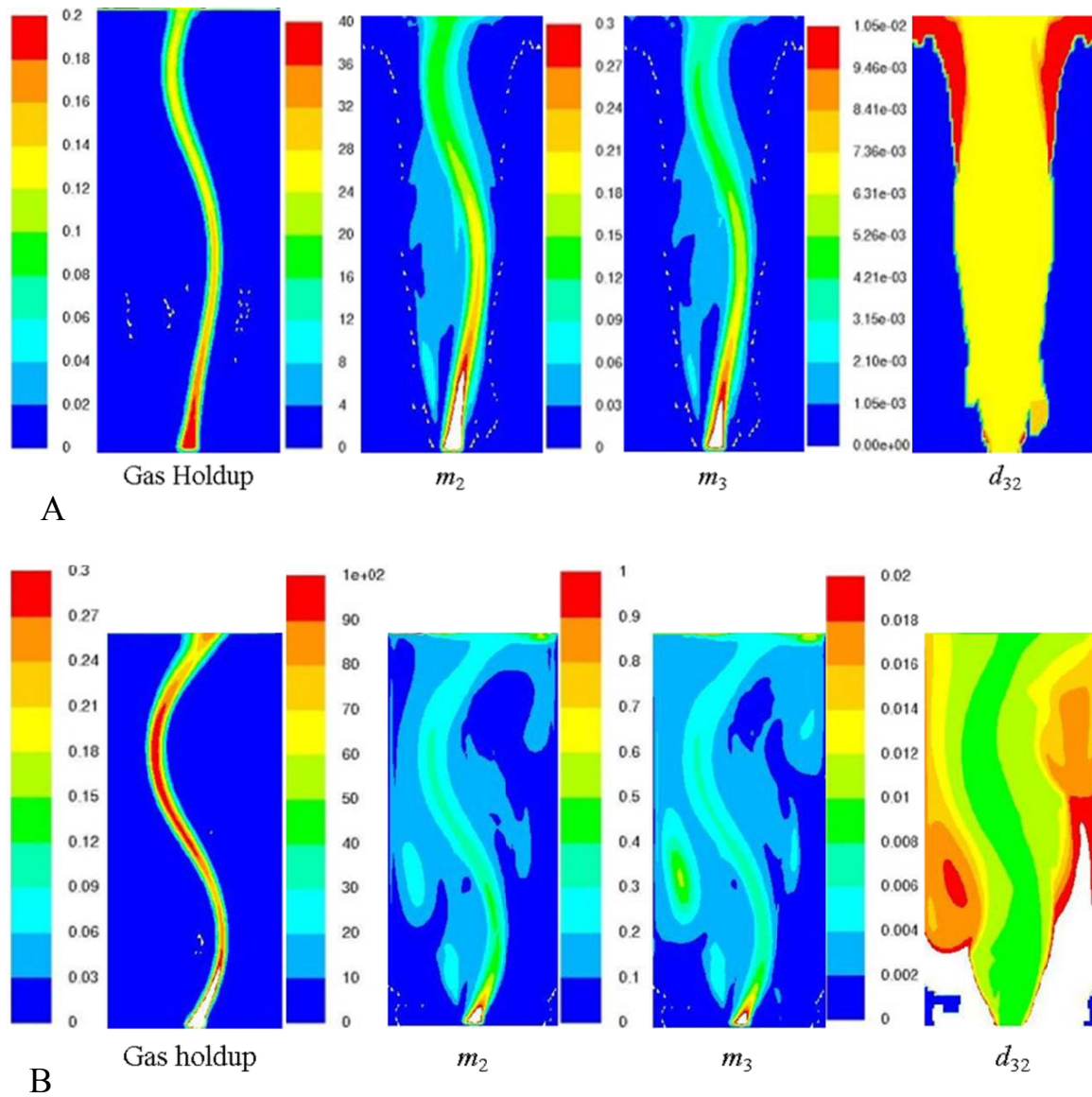


Figure 5.1 The instantaneous contours of gas holdup, generic moments m_2 , m_3 and Sauter mean diameter. Inlet and outlet's generic moments boundary conditions are defined as for Case 1 (Table 5.1). A) Gas flow rate 48 L/h; B) Gas flow rate 260 L/h.

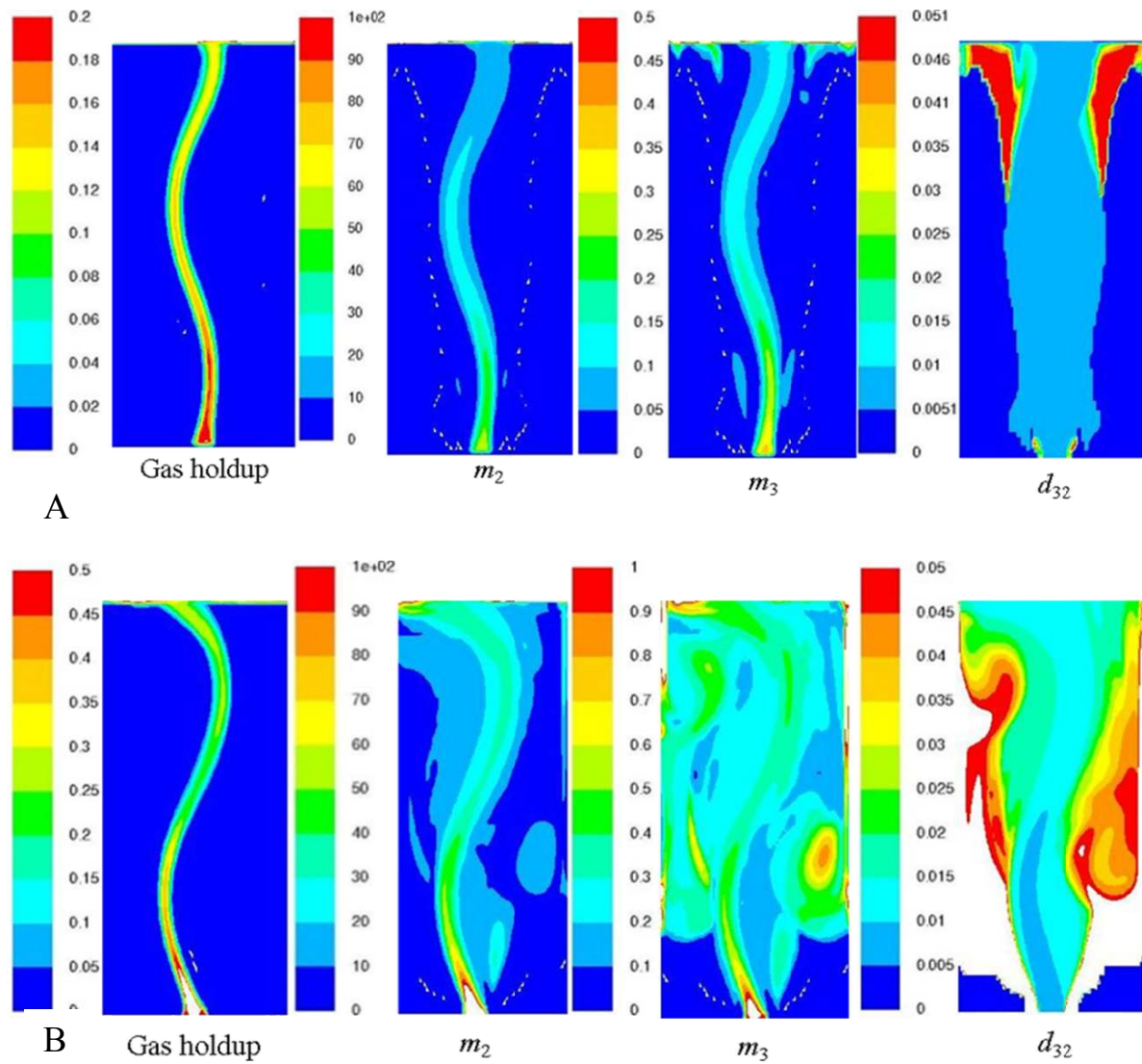


Figure 5.2 The instantaneous contours of gas holdup, generic moments m_2 , m_3 and Sauter mean diameter. Inlet and outlet's generic moments boundary conditions are defined as for Case 2 (Table 5.1). A) Gas flow rate 48 L/h; B) Gas flow rate 260 L/h.

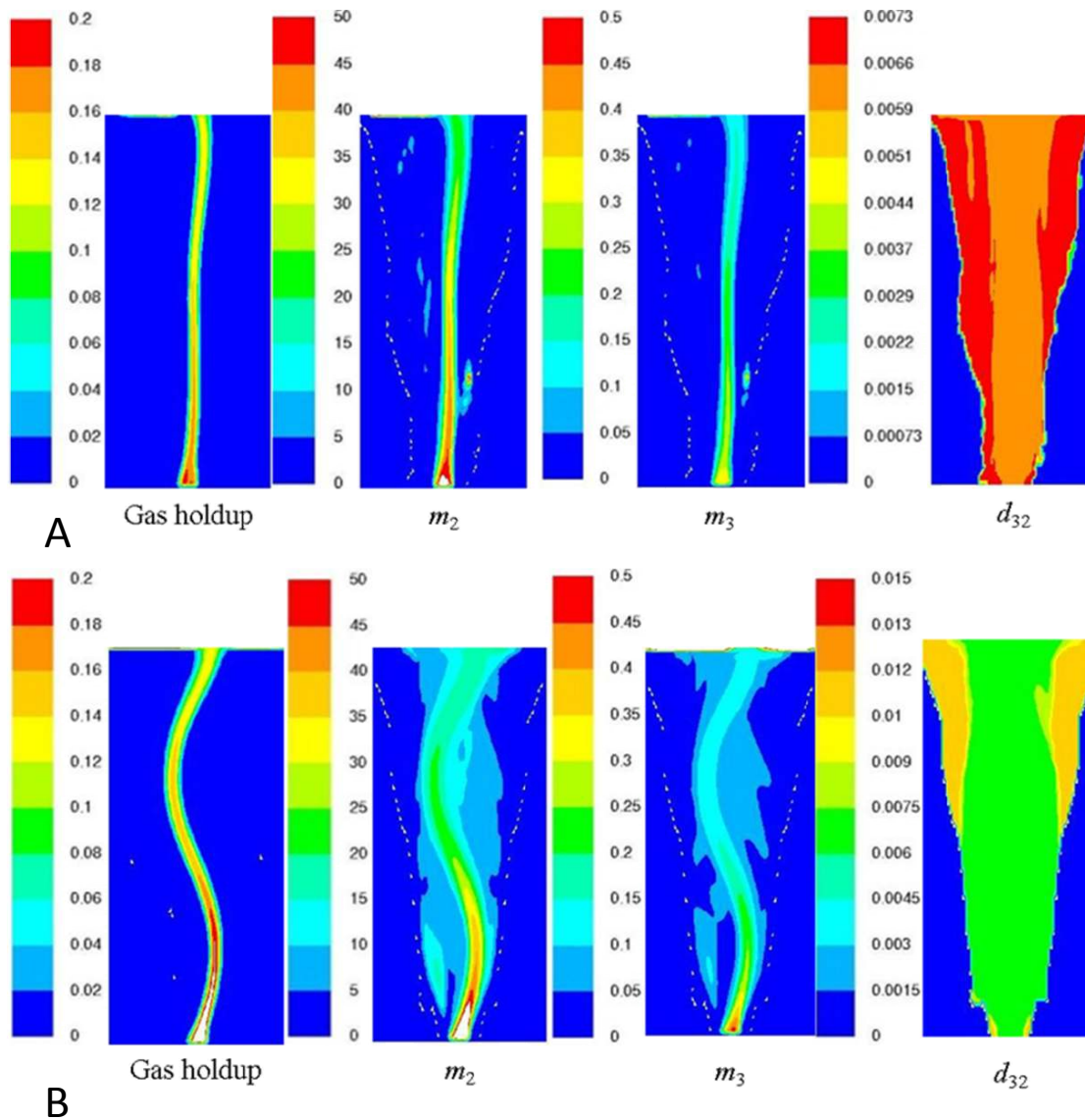


Figure 5.3 The instantaneous contours of gas holdup, generic moments m_2 , m_3 and Sauter mean diameter. Inlet and outlet's generic moments boundary conditions are defined as for Case 3 (Table 5.1). Gas flow rate is 48 L/h. A) With different turbulence model, the k- RNG per phase and number of generic moments are also change from 4 to 6. B) Change in applied number of moments from 6-8 others simulation parameters are same.

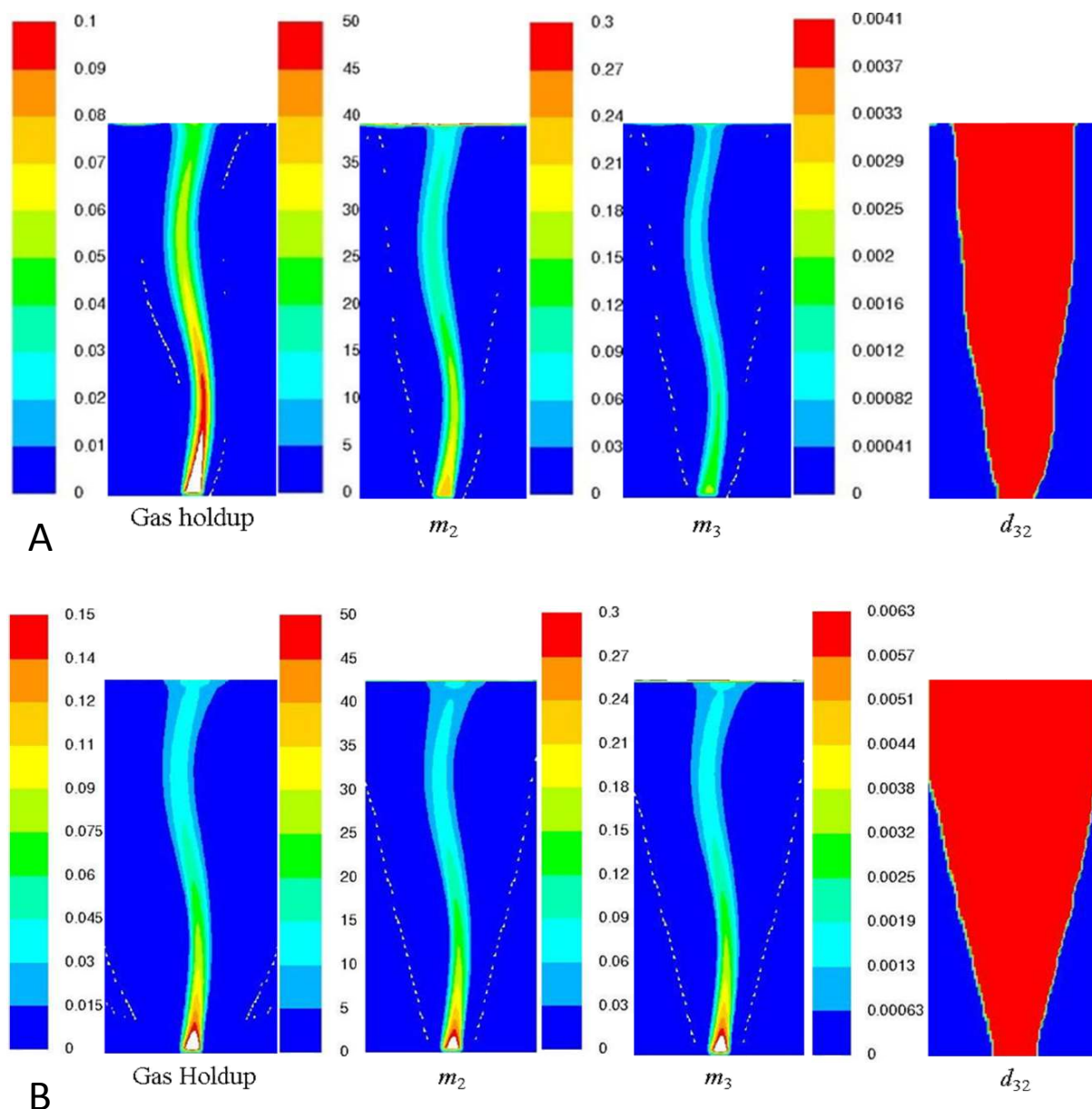


Figure 5.4 The instantaneous contours of gas holdup, generic moments m_2 , m_3 and Sauter mean diameter. Inlet and outlet's generic moments boundary conditions are defined as for Case 3 (Table 5.1) and discretization scheme of first order upwind applied. Gas flow rate is 48 L/h. A) Change from previous systems; the drag Coefficient correlation of Schiller and Naumann (1935) was used and the number of generic moments were also changed from 4 to 6. B) Lift interfacial force was applied and lift coefficient value was defined by Tomiyama et al, (2002) and change in applied number of moments from 4 to 6. Others simulation parameters were kept same.

5.3 QMOM with Breakage and Coalescence Models

In the previous section we have finalized the boundary conditions and simulations parameters for the hydrodynamics of rectangular bubble column reactor of generic moments for QMOM. In this section, we will simulate the BCR with the finalized moments boundary conditions and with breakage and

coalescence of bubbles. The bubble coalescence and breakage models used in this work are of built in models provided in FLUENT 13 package; the model by Luo and Svendsen (1996) was used for coalescence rate while the model by Laakkonen et al. (2006) was used for breakage frequency and fragment distribution function. The detail of simulations parameters for this section are given in Table 5.3 and in addition of finalized boundary conditions for moments we have also modelled the BCR using case 2 boundary conditions to observe the effect on the profile of Sauter mean diameter (Figure 5.9) Selma et al. (2010).

Table 5.3 Definition of Simulation parameters for QMOM cases with coalescence and breakage of bubble models.

Parameter	Definition
Inlet gas velocity V_{in}	Defined according to <i>GFR</i> 48 L/h or 260 L/h.
Gas Volume Fraction at inlet	0.014, based on Sparger: sparger holes area A_p per sparger cross sectional area A_t , A_p/A_t .
Bubble diameter at Sparger	Defined by Geary and Rice, (1999) Model <ul style="list-style-type: none"> • 6.06 mm for 48L/h • 8.49 mm for 260L/h
Inlet liquid velocity	0.0 m/s
Multiphase Model	Eulerian two phase
Viscous Model	Standard $k-\varepsilon$ per phase or specified
Drag Coefficient	Defined on constant terminal velocity, 20cm/s or specified.
Surface Tension	Constant: 0.071N/m
Pressure-Velocity coupling	Phase coupled SIMPLE
Discretization Scheme	QUICK or First Order upwind
Moments	First order upwind scheme, and at inlet BSD defined based on log-normal distribution. The six numbers of generic moments applied.
Breakage kernel	Breakage frequency and PDF: Laakkonen model

Coalescence kernel	Luo Model
Transient formulation	First order implicit
Time Step	0.001 s and after 30s, 0.01s.
Grid Size (L×W×H)	80×19×135

5.3.1 Results and Discussion

The instantaneous contours of different cases for gas holdup, generic moments, (m_2 and m_3) and Sauter mean bubble diameter, d_{32} , are shown in Figure 5.5 and 5.6. The Figure 5.5 A and 5.6 are the example for case 2 and Figure 5.5 B is example of case 3. The results of simulations with case 3 are better than case 2 as former case gave unexpected coalescence of bubbles in the upper part and near walls of column. The Figure 5.5B shows the contours of the average Sauter mean diameter of four files, it results that near the walls, the bubble size tends to decrease because of breakage phenomena dominates on coalescence, and in the central region of bubble column the bubble size tend to increase due to the large number of bubbles, in this region the coalescence phenomena dominates and therefore results in larger bubble sizes. We can say that population balance of the bubble size distribution gives better results than uniform bubble size application. The time averaged profiles of liquid axial velocity and gas holdup are better than without breakage and coalescence (Figure 5.7-5.8). Therefore the proposed simulation model with coalescence and breakage have provided good results and in agreement with experimental and others simulation models proposed by Selma et al. (2010).

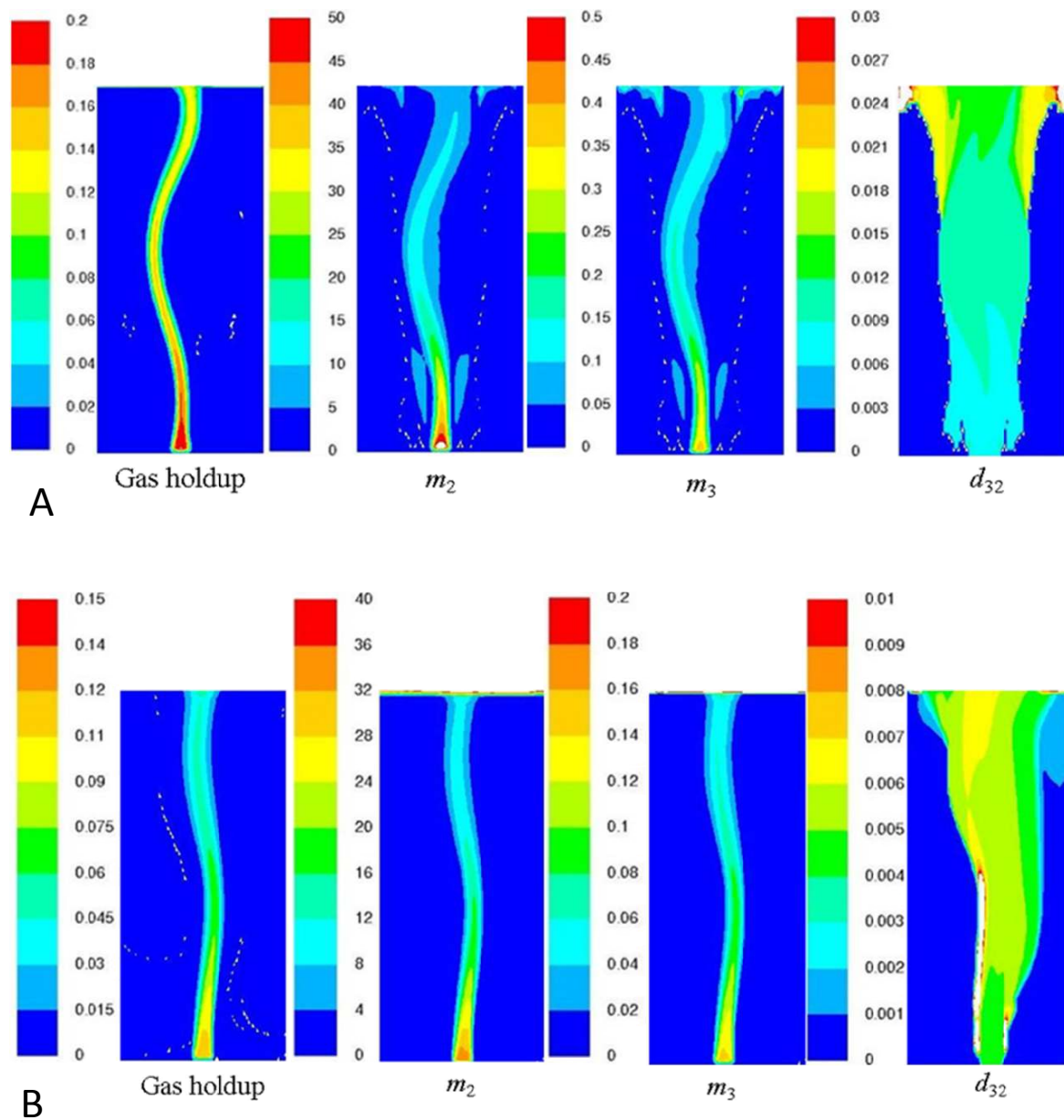


Figure 5.5 The instantaneous contours of gas holdup, generic moments m_2 , m_3 and Sauter mean diameter. Inlet and outlet's generic moments boundary conditions are defined as per Case 2 (upper A) and Case 3 (lower B) (Table 5.1), respectively. Gas flow rate is 48 L/h. A) Example of Case 2; B) Example of Case 3, Change from previous systems; drag Coefficient correlation was used of Schiller Naumann.

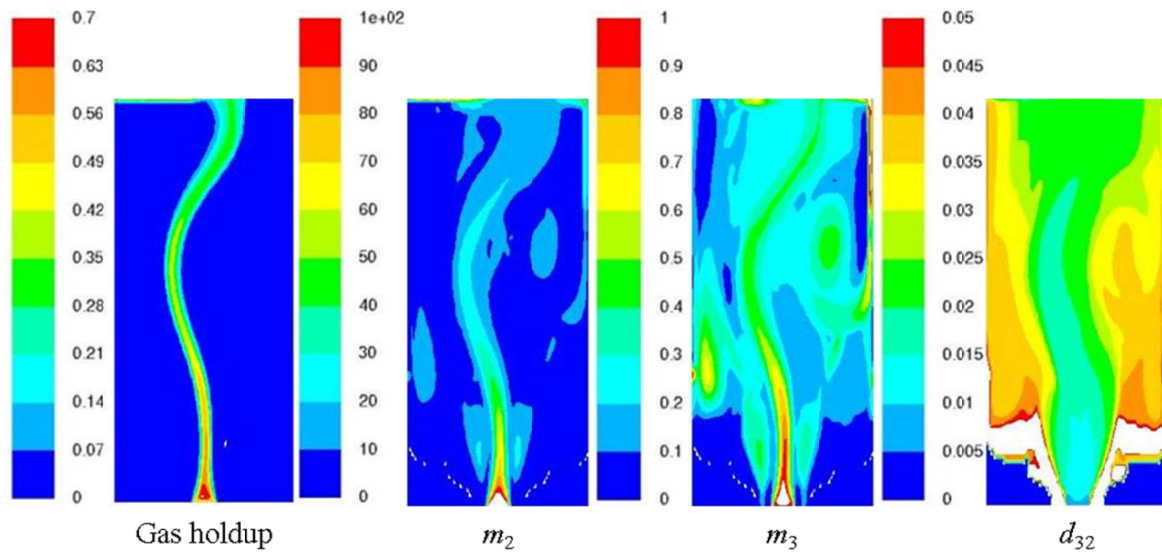


Figure 5.6 The instantaneous contours of gas holdup, generic moments m_2 , m_3 and Sauter mean diameter. Inlet and outlet's generic moments boundary conditions are defined as per Case 2 (Table 5.1). Gas flow rate is 260 L/h.

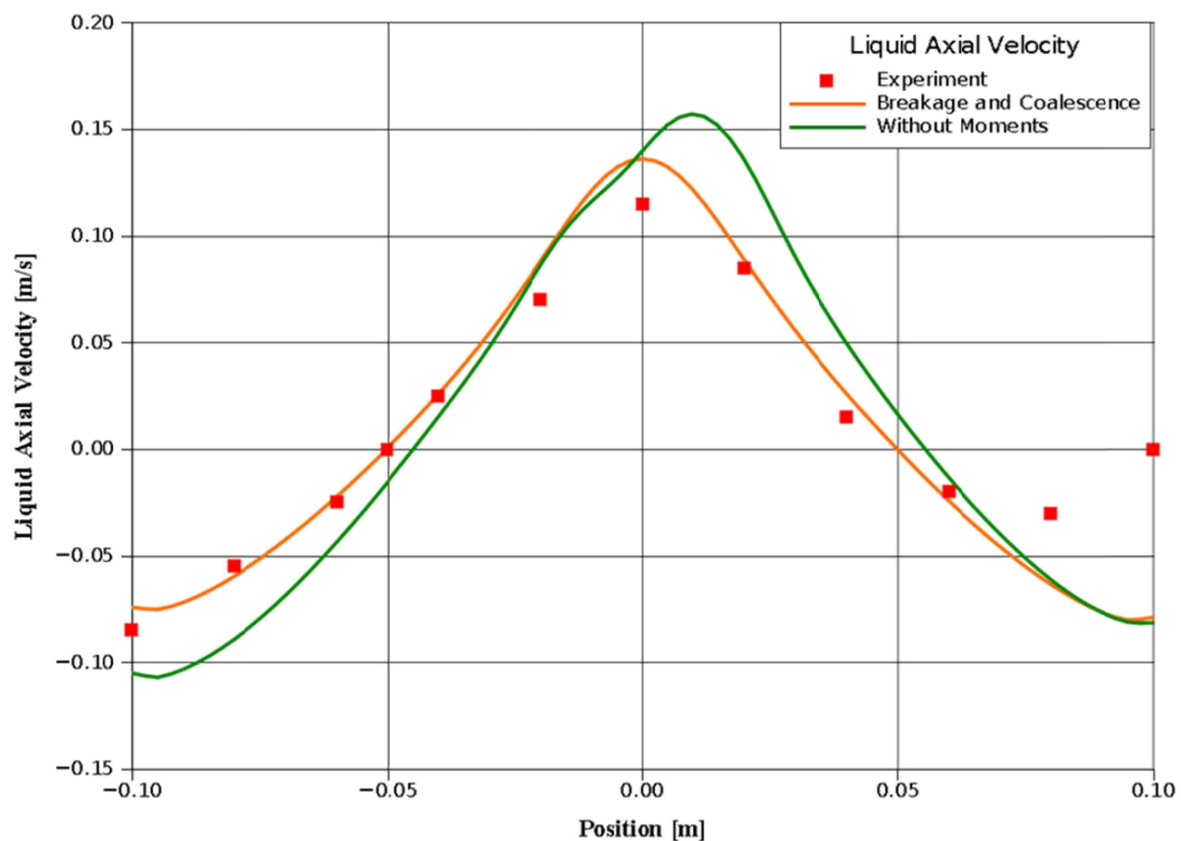


Figure 5.7 Time averaged liquid axial velocity profile along horizontal line in centre of column at height 0.37m from bottom (gas flow rate 48L/h).

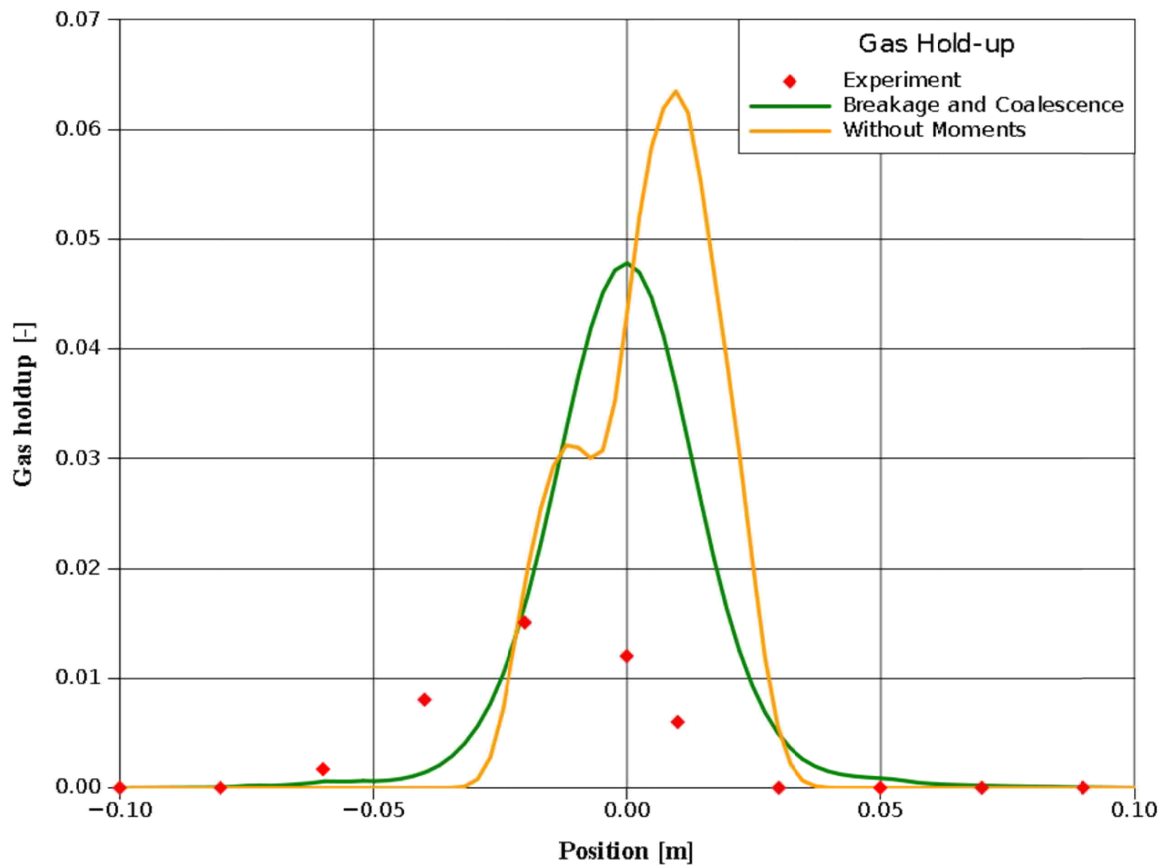


Figure 5.8 Time averaged gas holdup profile along horizontal line in centre of column at height 0.37m from bottom (gas flow rate 48L/h).

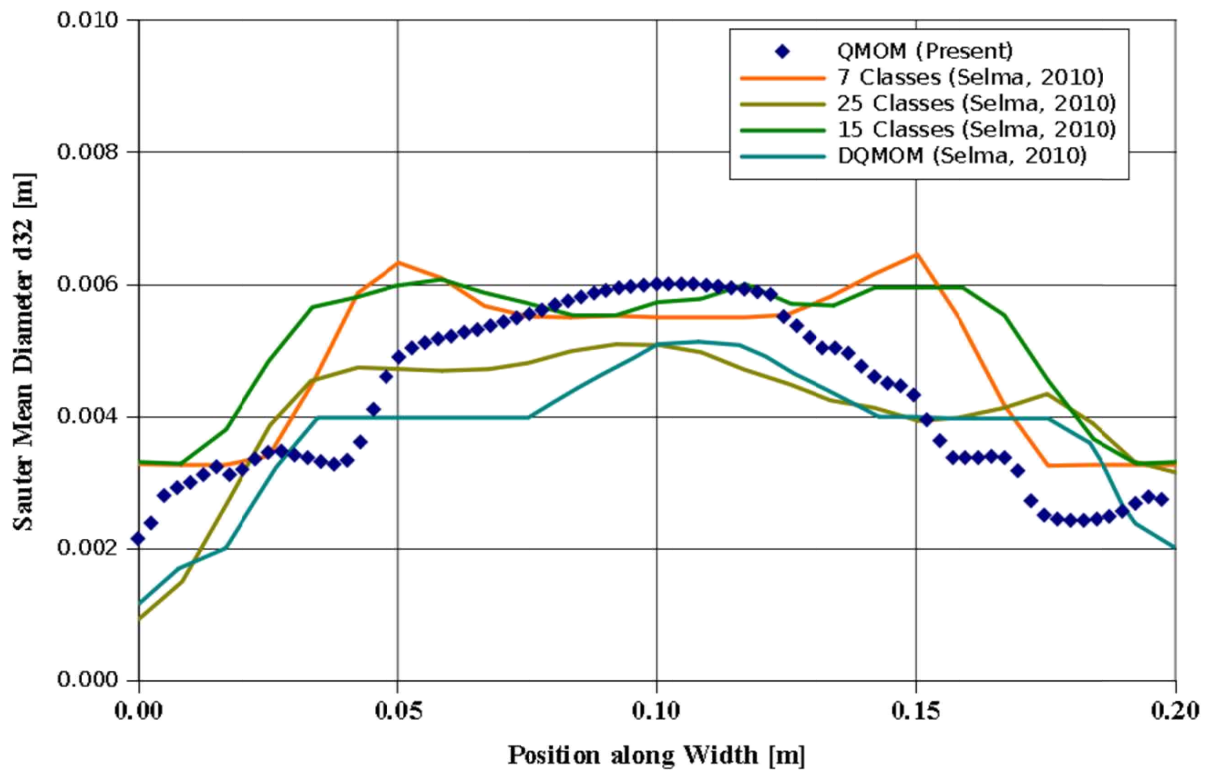


Figure 5.9 Comparison of simulations results for different PBM methods taken from Selma et al. (2010). The present result of QMOM is average of four data files. The Sauter mean diameter data is taken along horizontal line at height 0.37 m from bottom.

Chapter 6

Mass Transfer and Chemical Reaction in Bubble Column Reactor

6.1 Introduction

In this chapter, we will model the chemisorption of pure CO₂ gas in a caustic solution in a rectangular bubble column reactor (BCR) using FLUENT13 package. In previous chapters, we have established the benchmark for all the possible simulation parameters and schemes for hydrodynamics study and these will be helpful in understanding the complex mechanism of gas-liquid flow reaction in BCR. The study of overall performance of the gas-liquid BCR systems mainly depends on these mechanisms, the hydrodynamics of flow field, mass transfer, chemical reactions and their mutual interactions. Although many studies were carried out to understand these mechanisms together or separately for a system but still the complete understandings for these are limited. The computational cost with large memory is the main hindering factors for CFD modelling of BCR with reaction due to increases in complexity of the system.

For the numerical study of gas-liquid flow in BCR, two approaches are frequently used, Euler-Euler (E-E) (Mudde and Simonin, 1999; Pflieger et al., 1999; Joshi, 2001; Sokolichin et al., 2004; Dhotre and Joshi, 2004; Tabib et al., 2008) and Euler-Lagrange (E-L) Models (Lapin and Lübbert, 1994, Delnoij et al.; Devanathan et al., 1995; Lain et al., 1999; Buwa et al., 2006). When we are considering the mass transfer from gas to liquid, in the E-L approach, the bubble shrinkage due to mass transfer can be calculated for each individual bubble with account on properties of bubble. On the other hand, in the Euler-Euler approach, the size of bubbles is not accounted as gas-liquid mass transfer results to a decrease in bubble size or decrease in the number of bubbles. This suggests that the E-E model, in the absence of population balance models, may only be implemented if the rate of mass transfer is relatively low or, in case the change in the bubble size is small. It seems that it is easier to study the bubble size change in the E-L model but it requires high computational costs, and it is not suitable to study gas-liquid flow in case of high gas volume fraction or the

case of large-scale BCRs. In present study, the E-E model is preferred to study the mass transfer in gas-liquid flows of BCR.

When a gas-liquid system with a chemical reaction is considered, the couplings between the relevant phenomena are very complex as schematically illustrated in Figure 6.1. The rate of chemical reaction depends on the concentration of the species, which is calculated by the inter-phase mass transfer process and the mixing is caused by the bubbles. The mass transfer rate depends on the mass transfer coefficient k_L , the specific interfacial area ' a ' and the chemical reaction rate; the mass transfer coefficient is a function of the local hydrodynamics, which itself is influenced by the bubble shrinkage due to physical or chemical absorption and the inhomogeneous distributions of the chemical species.

In presence of these complex interactions, the prediction of the performance and scale-up of such kind of reactor is very tough. This can be one of the reasons that most CFD studies of gas-liquid flow have been mainly focused on the simulation of the hydrodynamics and improvement in the closures required by the models to attain a better prediction of the hydrodynamics. Many authors tried to simulate the system by decoupling the interaction between phenomena hydrodynamics, mass transfer, and chemical reactions and simulate each phenomenon with a separate model. In those models, CFD is applied only for the hydrodynamic simulation, while the chemical reactions are modelled for in a custom-built compartmental model (Bauer and Eigenberger, 1999, 2001; Rigopoulos and Jones, 2003). However, this method does not include feedback from the mass transfer and chemical reaction phenomena to the hydrodynamics. A full 3D modelling, by accounting for all relevant phenomena such as hydrodynamics, mass transfer and chemical reaction in a single model so far is only limited to a study of the effect of mass transfer on hydrodynamics during a limited time interval (Mewes and Wiemann, 2003). Recently Darmana et al., (2007) developed a method that can handle the hydrodynamics, mass transfer and chemical reactions in a bubble column based on the E-L approach model developed previously by Delnoij et al. (1997, 1999).

The chemisorption of CO₂ into caustic solution is chosen as the test case for present work as the reaction mechanism and kinetics of this are well understood. We have assumed constant bubble diameter of 5.5 mm. In case of shrinkage of bubble, we are assuming that the bubble size is not much changing and will remain in the range of (2-10 mm) and the drag coefficient is almost will remain constant according to the bubble terminal velocity in this range of

bubble sizes (2-10 mm) remained constant. In E-E approach the consideration of change in the bubble size is not directly considered. Therefore, in initial test cases, we are not considering the feedback of chemical reaction on the mass transfer. Therefore, in E-E approach for modelling of chemisorption of the gas bubbles into liquid reacting mixtures; it is assumed that the change in bubble size is negligible that it will not greatly affect other simulation parameters. In later cases we will not consider the above assumptions and will account the change in bubble sizes through bubble population balance approach of QMOM in order to attain valid simulation results.

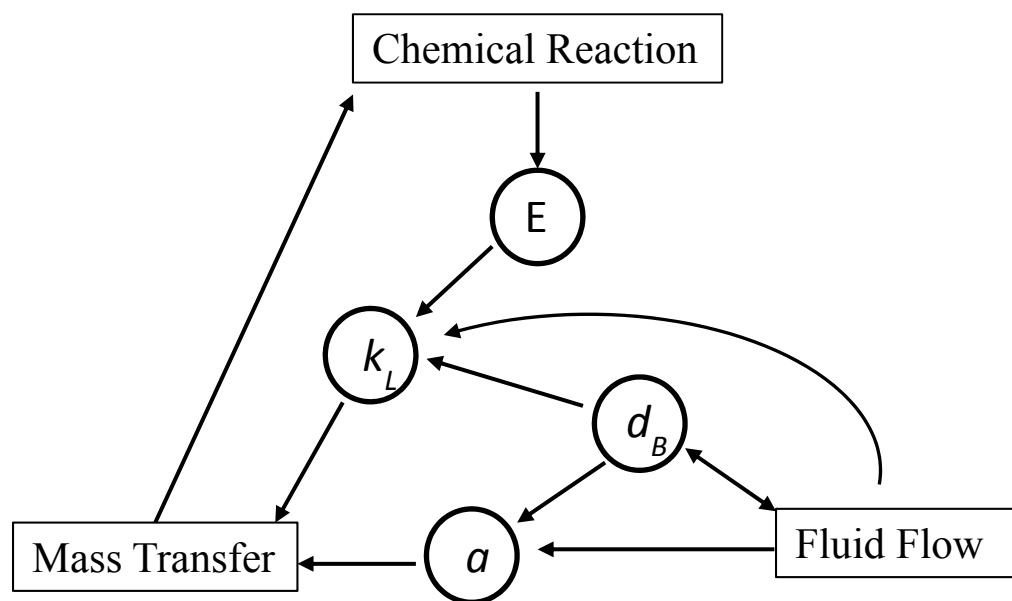


Figure 6.1 Representation of inter-dependent phenomena of chemical reaction, mass transfer and fluid flow Illustrated from Darmana et al. (2007), where the k_L is the mass transfer coefficient, ' a ' is the interfacial area, d_B is the bubble diameter and E is the mass transfer enhancement factor.

The present work is divided in three parts, in first part; we have validated the proposed chemisorption model of CO_2 in NaOH aqueous solution by assuming a perfectly mixed liquid phase and using MATLAB code for the solution. In second part; we have numerically modelled the proposed work with FLUENT13 package for rectangular shape bubble column using E-E approach and with fixed bubble size. In third part, we will model the same work with account on change in bubble size through population balance equation of QMOM approach. The information about column size and operating conditions are given in Table 6.1. The detail of governing equations and simulations are discussed in coming sections.

6.2 Governing Equations and Reactions

In the Chapter 2 we have discussed in detail the multi fluid model obtained by ensemble averaging technique of the local transport instantaneous equations. Final set of equations are (2.75)-(2.80). Here we are just presenting the conservation equations for the generic phase k for mass and momentum, respectively:

$$\frac{\partial}{\partial t}(\alpha_k \rho_k) + \nabla \cdot (\alpha_k \rho_k \mathbf{u}_k) = -\dot{M}_{k \rightarrow l} \quad (6.1)$$

$$\begin{aligned} \frac{\partial}{\partial t}(\alpha_k \rho_k \mathbf{u}_k) + \nabla \cdot (\alpha_k \rho_k \mathbf{u}_k \mathbf{u}_k) = & \alpha_k \rho_k \mathbf{g} - \nabla \cdot \alpha_k \boldsymbol{\tau}_k - \alpha_k \nabla p_k \\ & + \mathbf{M}_k - \dot{M}_{k \rightarrow l} \mathbf{u}_k \end{aligned} \quad (6.2)$$

The term $\dot{M}_{k \rightarrow l}$ is mass transfer rate from phase k to l and last term of (6.2) is the momentum transfer induced by mass transfer. The other parameters in the above equations (6.1) and (6.2) were discussed and defined in Chapter 2. Based on our proposed system, when we have volumetric reactions in bulk of liquid mixture, the following is the relation for transport of chemical species A for the liquid phase:

$$\frac{\partial}{\partial t}(\alpha_L \rho_L Y_L^A) + \nabla \cdot (\alpha_L \rho_L Y_L^A \mathbf{u}_L - \alpha_L \Gamma_L^A \nabla Y_L^A) = S_A \quad (6.3)$$

Where the Y_L^A is the mass fraction of chemical species A in bulk liquid, S_A is the source term for species A and Γ_L^A is the species diffusion coefficient. Similarly for gas phase in case of CO_2 gas, the following transport equation can be written:

$$\frac{\partial}{\partial t}(\alpha_G \rho_G Y_G^{\text{CO}_2}) + \nabla \cdot (\alpha_G \rho_G Y_G^{\text{CO}_2} \mathbf{u}_G - \alpha_G \Gamma_G^{\text{CO}_2} \nabla Y_G^{\text{CO}_2}) = S_G^{\text{CO}_2} \quad (6.4)$$

The chemisorption of CO_2 in caustic solution is composed of two reactions. In the first step the CO_2 is physically absorbed in water



The following reactions then take place:





Where k_{11} and k_{12} are the rate constants of forward and backward reactions of (6.5), respectively; similarly, the k_{21} and k_{22} are rate constants of reaction of (6.6), respectively. The rate equations of above reactions can be written as:

$$R_{11} = k_{11} [\text{CO}_2] [\text{OH}^-], \quad (6.8)$$

$$R_{12} = k_{12} [\text{HCO}_3^-], \quad (6.9)$$

$$R_{21} = k_{21} [\text{HCO}_3^-] [\text{OH}^-], \quad (6.10)$$

$$R_{22} = k_{22} [\text{CO}_3^{2-}]. \quad (6.11)$$

The detailed expressions for rate constants are discussed in Appendix A.

The mass transfer rate of CO_2 to the liquid phase per unit volume is defined as:

$$\dot{M}_{\text{CO}_2 \rightarrow L} = k_L a E \rho_L (Y_{\text{int}}^{\text{CO}_2} - Y_L^{\text{CO}_2}) \quad (6.12)$$

where k_L is the mass transfer coefficient for the source of CO_2 in the bulk liquid, 'a' is the interfacial area and is defined as; $a = 6\alpha_G/d_b$, E is the enhancement factor and $Y_{\text{int}}^{\text{CO}_2}$ is the CO_2 mass fraction in the liquid at the interphase in equilibrium with the concentration of gas phase. In the case we will study the gas phase is made of pure CO_2 . For such a condition $Y_{\text{int}}^{\text{CO}_2}$ can be calculated as :

$$Y_{\text{int}}^{\text{CO}_2} = H \frac{\rho_G}{\rho_L} \quad (6.13)$$

where H is the Henry constant. The enhancement factor E is calculated from following expression proposed by Westerterp et al. (1984):

$$E = \begin{cases} -\frac{Ha^2}{2(E_\infty - 1)} + \sqrt{\frac{Ha^4}{4(E_\infty - 1)^2} + \frac{E_\infty Ha^2}{E_\infty - 1} + 1} & E_\infty > 1 \\ 1 & E_\infty \leq 1 \end{cases} \quad (6.14)$$

where

$$E_{\infty} = \left(1 + \frac{D_{\text{OH}^-} [\text{OH}^-]}{2D_{\text{CO}_2} H [\text{CO}_2(\text{g})]} \right) \sqrt{\frac{D_{\text{CO}_2}}{D_{\text{OH}^-}}}, \quad (6.15)$$

and

$$Ha = \frac{\sqrt{k_{11} D_{\text{CO}_2} [\text{OH}^-]}}{k_L} \quad (6.16)$$

The k_L is defined by the following expression of Brauer (1981):

$$Sh = \frac{k_L d_b}{D_{\text{CO}_2}} = 2 + 0.015 \text{Re}^{0.89} Sc^{0.7} \quad (6.17)$$

All others parameter relations and adopted values for test cases are given in Table 6.1.

Table 6.1 Differences in cases studied and definition of parameters and values.

Test Case	Definition
Test Case 1	Verification of available physical and kinetic data on MATLAB
Test Case 2	E-E approach, simulation with mass transfer and chemical reaction with fixed bubble size.
Test Case 3	E-E approach, simulation with mass transfer and chemical reaction with change in bubble size is adopted through PBE QMOM approach.
Parameters Involved	
Solubility of CO ₂ , Weisenberger and Schumpe (1996); Darmana (2006)	$\log\left(\frac{H_w}{H}\right) = \sum (h_i + h_g) c_i$ and $H_w = 3.59 \times 10^{-7} RT \exp(2044/T)$ H_w is the solubility coefficient of CO ₂ in pure water.
Diffusivity of CO ₂ ,	$D_{\text{CO}_2}^w = 2.35 \times 10^{-6} \exp(-2119/T)$, Versteeg and van Swaaij (1998), is for pure water and in electrolyte solution: $\frac{D_{\text{CO}_2}}{D_{\text{CO}_2}^w} = 1 - 1.29 \times 10^{-4} [\text{OH}^-]$, Ratcliff and Holdcroft (1963).

Parameters ValuesBubble size, $d_b = 5.5$ mmGas flow rate = 46.2×10^{-6} , m³/sDensities, $\rho_G = 1.29$, $\rho_L = 998$, kg/m³Viscosities, $\mu_G = 1.812 \times 10^{-5}$, $\mu_L = 0.001$, kg/m/s $\sigma = 0.728$, N/m

Initial pH of solution = 12.5

 $\mathbf{u}_{rel} = \mathbf{u}_G - \mathbf{u}_L = 0.2$ m/s,**6.3 Applicability of the physical data**

In this test case, we have verified our kinetics and physical data for chemisorption of CO₂ gas in caustic solution using MATLAB. For this we consider a column, in which CO₂ is entering from bottom and leaving from top. The liquid inside the 1 m³ column is caustic solution with pH of 12.5. The initial bubble size is taken as 5.5 mm and gas holdup as 1.6% and we consider that system as homogeneous. The chemical reactions in the system are given in (6.5)-(6.7) and the corresponding reactions rates in equations (6.8)-(6.11). The chemical species present in the liquid are, CO₂ (aq), OH⁻, HCO₃⁻ and CO₃²⁻. The assumed column is shown in Figure 6.2. Physical parameters values are given in Table 6.1.

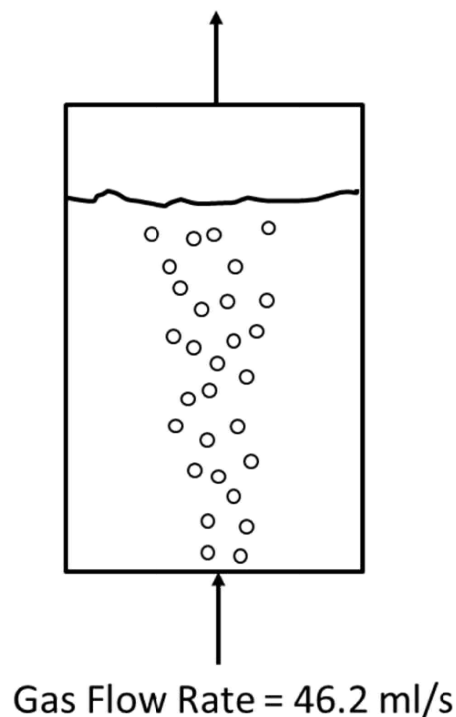


Figure 6.2 Proposed schemes for test case 1.

We developed four differential equations for the balance of chemical species for the proposed system:

$$\frac{d[\text{CO}_2(\text{aq})]}{dt} = Ek_L a([\text{CO}_2, \text{int}] - [\text{CO}_2(\text{aq})]) - k_{11}[\text{CO}_2(\text{aq})][\text{OH}^-] + k_{12}[\text{HCO}_3^-] \quad (6.18)$$

$$\frac{d[\text{OH}^-]}{dt} = -k_{11}[\text{CO}_2(\text{aq})][\text{OH}^-] + k_{12}[\text{HCO}_3^-] - k_{21}[\text{HCO}_3^-][\text{OH}^-] + k_{22}[\text{CO}_3^{2-}] \quad (6.19)$$

$$\frac{d[\text{HCO}_3^-]}{dt} = k_{11}[\text{CO}_2(\text{aq})][\text{OH}^-] - k_{12}[\text{HCO}_3^-] - k_{21}[\text{HCO}_3^-][\text{OH}^-] + k_{22}[\text{CO}_3^{2-}] \quad (6.20)$$

$$\frac{d[\text{CO}_3^{2-}]}{dt} = k_{21}[\text{HCO}_3^-][\text{OH}^-] - k_{22}[\text{CO}_3^{2-}] \quad (6.21)$$

where $[\text{CO}_2, \text{int}]$ is the concentration of CO_2 gas at interphase and $[\text{CO}_2(\text{aq})]$ is the concentration of CO_2 absorbed in bulk liquid. The initial conditions applied for the above system of differential equations when $t = 0$, then initial concentrations (kmol.m^{-3}) of species and conditions:

$$\begin{aligned} [\text{CO}_2(\text{aq})] &= 0, \\ [\text{OH}^-] &= 0.031623, \\ [\text{HCO}_3^-] &= 0, \\ [\text{CO}_3^{2-}] &= 0. \end{aligned} \quad (6.22)$$

Bubble size = 0.0055 m
Gas holdup = 0.016

6.3.1 Results and Discussion

The chemisorption process of CO_2 gas with flow rate 46.2 ml/s through liquid with initial pH 12.5 was studied. In this test case, we solve the developed concentration differential equation and estimation of the species concentration with respect to time is shown in Figure 6.3. In start of reaction, all the absorbed CO_2 reacts with hydroxide ions (OH^-) and produce the carbonate ions (CO_3^{2-}), while the concentration of bicarbonate ions (HCO_3^-) in start of reactions is negligible. At about 45s after the reactions start, the concentration of carbonate attains a maximum value and after then starts to decrease. Meanwhile the concentration of bicarbonate ions starts to increase and is also observable in

pH profile. The variation in pH of the system as reactions proceeded is shown in Figure 6.4. In addition of these species reactions, we also plot the rate of variation of CO_2 gas absorbed in the bulk liquid from its initial concentration entering into the column. The obtained profiles of evaluation of concentration and pH are similar to Darmana et al. (2007) concentration and pH profiles at a point in the bubble column with respect to time. Consequently we can say that the available kinetics and physical data is applicable to predict the chemical evaluation for our next case of studies.

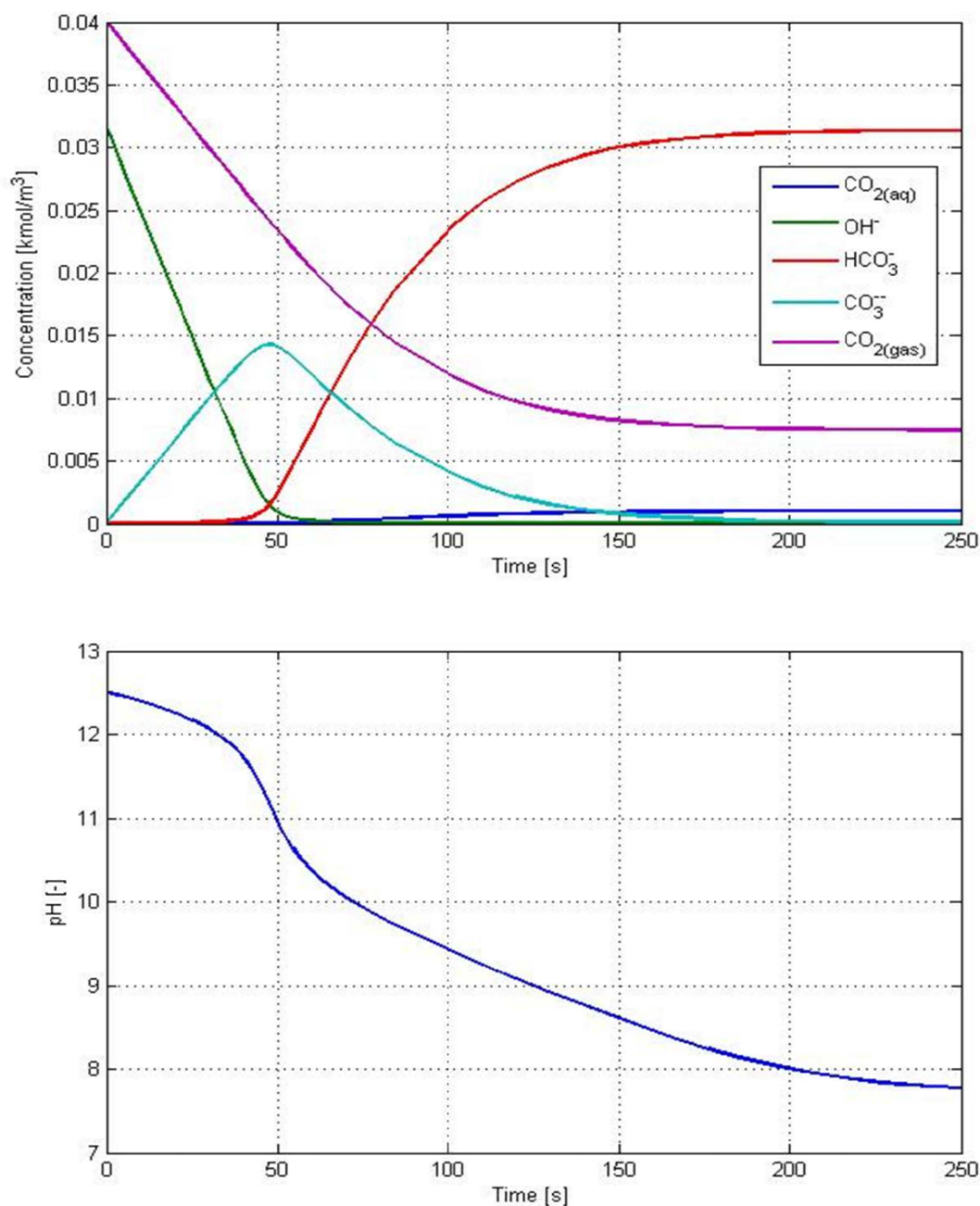


Figure 6.3 Time history of species concentration history and corresponding pH profile at bottom for our proposed system.

The mass transfer coefficient relation given in (6.17) can be written as:

$$k_L = \frac{D_{\text{CO}_2} (2 + 0.015 \text{Re}^{0.89} \text{Sc}^{0.7})}{d_b} \quad (6.23)$$

or

$$k_L = \frac{D_{\text{CO}_2} \left(2 + 0.015 \left(\frac{\rho_L \mathbf{u}_{rel} d_b}{\mu_L} \right)^{0.89} \left(\frac{\mu_L}{\rho_L D_{\text{CO}_2}} \right)^{0.7} \right)}{d_b} \quad (6.24)$$

It was found that the variation of OH^- concentration doesn't much affect the diffusivity of CO_2 as per the proposed model for diffusivity of Ratcliff and Holdcroft (1963) so we assumed the constant diffusivity. One more assumption of constant relative velocity of 0.2 m/s for the bubble sizes from [4-5.5] as in this range the relative velocity of gas bubble and liquid phase remain constant. The rate of shrinkage of bubble with time due to mass transfer of CO_2 to liquid phase, for this we adopted the relation as given by Zhang (2007):

$$\frac{dd_b}{dt} = -2H \frac{D_{\text{CO}_2} \left(2 + 0.015 \left(\frac{\rho_L \mathbf{u}_{rel} d_b}{\mu_L} \right)^{0.89} \left(\frac{\mu_L}{\rho_L D_{\text{CO}_2}} \right)^{0.7} \right)}{d_b} \quad (6.25)$$

The plots of mass transfer coefficient with varying the bubble size and the shrinkage bubble rate due to mass transfer to liquid phase are shown in Figure 6.4. From the above discussion, we can simulate the BCR with discussed kinetics, physical data and assumptions of constant bubble diameter for next test case 2. However, we will consider the rate of change of bubble size in next case through PBE QMOM.

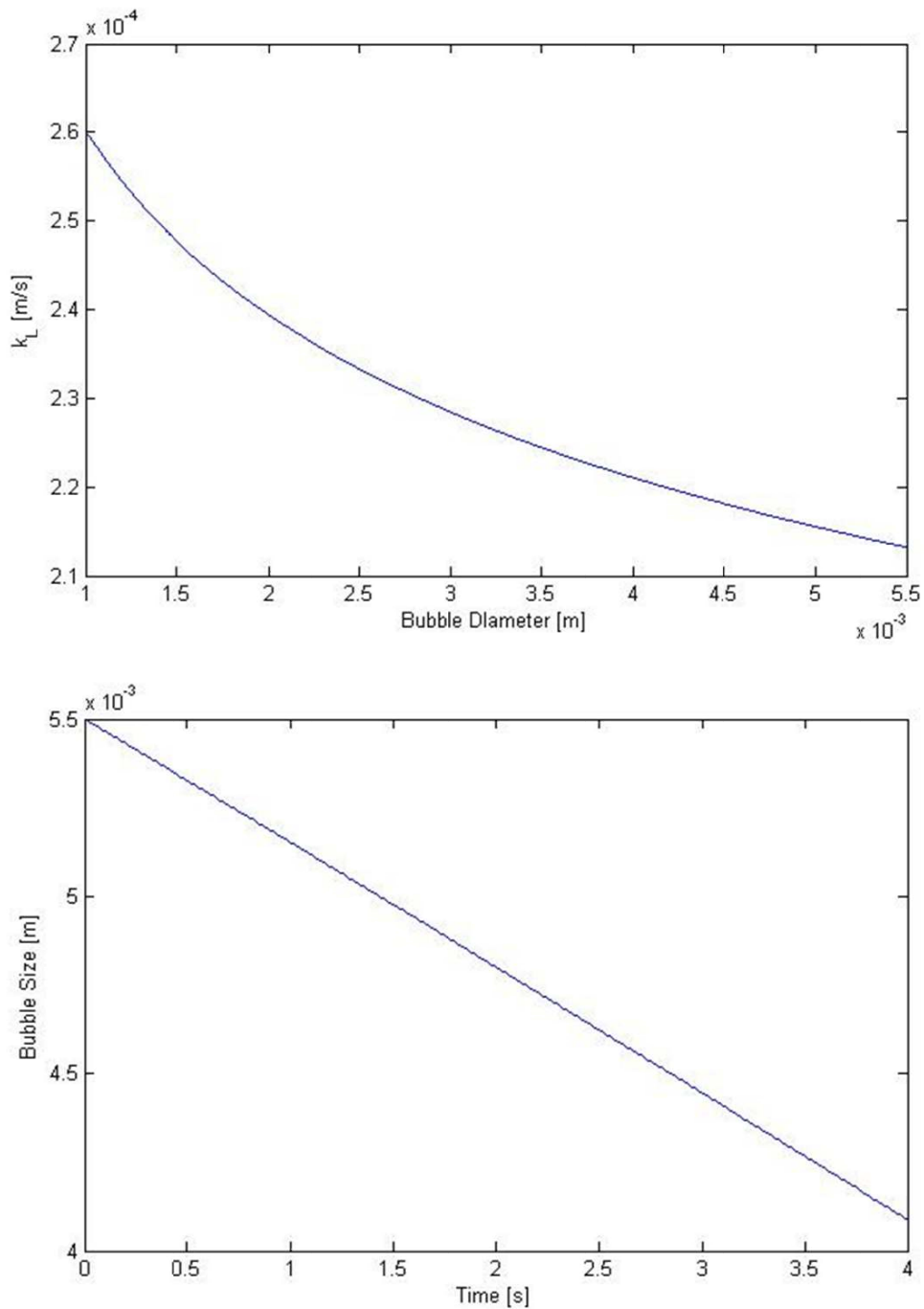


Figure 6.4 The variation of k_L with bubble diameter and lower one is the shrinkage rate of bubble size due to mass transfer with time.

6.4 CFD simulation with mass transfer and chemical reaction

In this section, we simulated the rectangular shape BCR using E-E approach, with uniform bubble size. A geometric representation of the column taken from work of Darmana et al. (2007) is shown in Figure 6.5. The column is filled with stagnant aqueous NaOH solution with initial pH 12.5 up to level of 1000 mm.

Pure CO₂ is sparged through sparger with flow rate of 46.2 ml/s. The dimensions and physical conditions of the bubble column reactor (BCR) are given in, Table 6.2. For detailed experimental setup and geometry layout, refer to the papers by Darmana et al. (2007).

Table 6.2 Bubble column used in simulation: Geometry and physical conditions.

Parameter	Definition
Size of BCR	$L \times W \times H = 200 \times 30 \times 1500$, in mm
Liquid Level	1000 mm
Gas Flow Rate	46.2 ml/s (2.2 ml/s per needle)
Sparger and its dimensions	21 needle tubes with diameter 1 mm each, installed in centre of bottom of column. Sparger size: $L \times W = 35 \times 15$ (mm)
Phases	Continuous Phase: Aqueous NaOH with initial pH = 12.5 Dispersed Phase: pure CO ₂
Bubble Diameter	5.5 mm, assumed uniform

In this section we will show the results obtained by assuming uniform bubble size in the simulations, while the study of the role of the actual bubble size distribution, originated by coalescence, breakage and mass transfer, is left to a subsequent section.

6.4.1 Simulation Setup

The commercial CFD software FLUENT (ANSYS, Version 13) is used to numerically model the hydrodynamics of the BCR. The inlet boundary is defined as velocity inlet. The inlet velocity of the CO₂ gas is defined according to the volumetric gas flow rate GFR (3.14). Inlet velocity of liquid solution was taken as zero. The initial level of liquid was always set to 1000 mm. The outlet boundary is defined as pressure outlet with back flow volume fraction of 1 of CO₂ gas. The species transport model with volumetric bulk liquid reactions is applied to estimate the mass fractions of CO₂ (aq), OH⁻, HCO₃⁻, CO₃²⁻ and H₂O.

The initial mass fraction of OH^- was calculated from initial pH taken 12.5 and all other species as zero except water and calculated as follows:

$$Y_{\text{H}_2\text{O}} = 1 - (Y_{\text{CO}_2(\text{aq})} + Y_{\text{OH}^-} + Y_{\text{HCO}_3^-} + Y_{\text{CO}_3^{2-}}) \quad (6.26)$$

The details of other simulation parameters are given in Table 6.3.

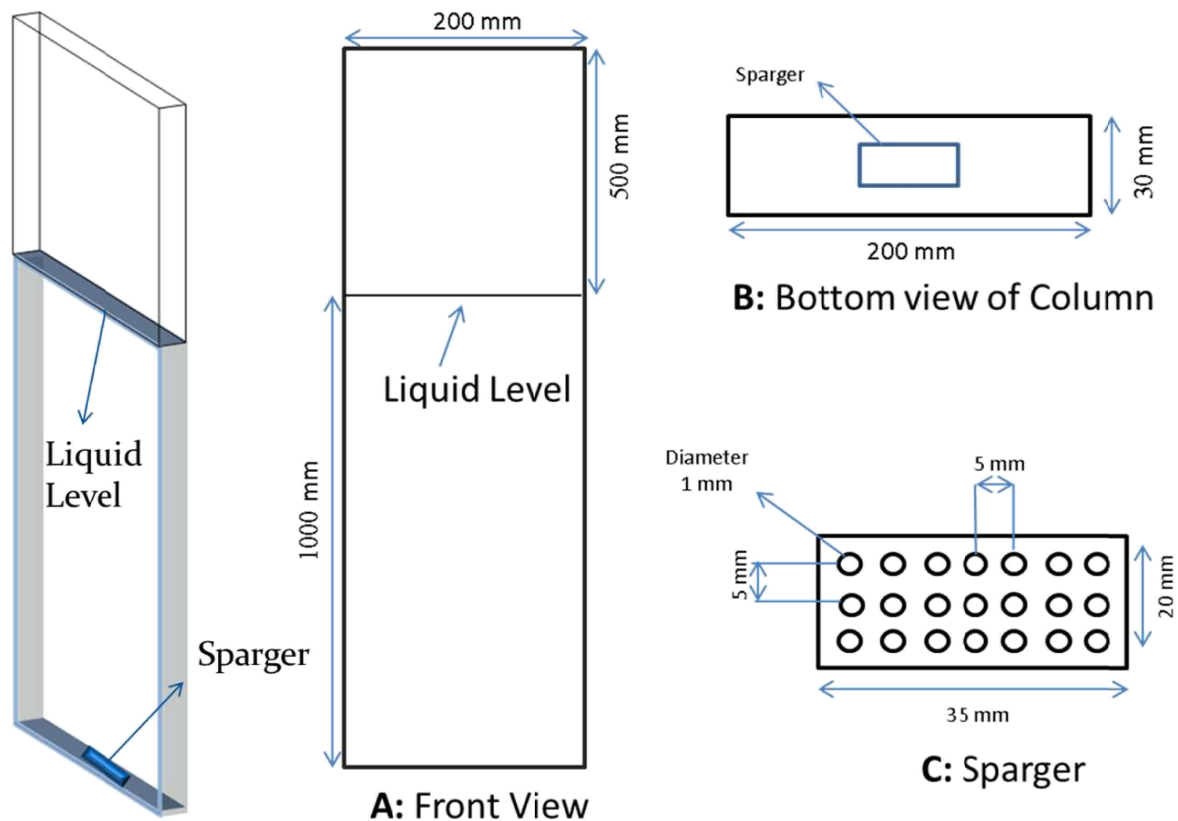


Figure 6.5 Geometric layout of the bubble column used in test case 1, (A) is the front view, (B) is the bottom view of the column with sparger in middle of the base, (C) is sparger dimensions with 21 needle tubes with diameter of 1 mm each.

6.4.2 Results and discussion

The results for chemisorption of CO_2 gas in aqueous NaOH solution are obtained and compared with experimental data. The CO_2 gas is sparged in the BCR filled with NaOH solution through sparger with a flow rate of 46.2 ml/s. The initial pH of the liquid solution was taken as 12.50. When gas move upward through the liquid, some of CO_2 is absorbed in the liquid with mass transfer mechanism (6.5) and subsequently start the reversible reactions presented in (6.6) and (6.7). Figure 6.6a, represented the instantaneous contours of the CO_2 gas volume fraction at different times. The meandering plume behaviour of the

gas bubbles appeared after simulation of 10 s and due to snake-like motion of gas, vortical structure of flow is observed in liquid vector velocity picture and these vortices are separated by oscillating plume in axial direction (Figure 6.6b). We cannot observed the bubble size change as we have applied E-E multiphase model, however the lowering gas VF in the contours along the height in the column is due to the chemical absorption of the CO₂ in the liquid. Time averaged profile of gas VF also shows the similar behaviour due to mass transfer mechanism of CO₂ to the liquid, high gas VF in lower region and low gas VF in upper portion. The observed flow structure of simulation is resembled to the experimental one.

Table 3.3 Definition of Simulation parameters for cases for interfacial forces closure.

Parameter	Definition
Inlet gas velocity V_{in}	2.802548 m/s defined according to (3.14) with GFR 4.62×10^{-5} m ³ /s and inlet gas volume fraction 0.0314.
Gas Volume Fraction	0.0314, based on sparger holes area A_p per sparger cross sectional area A_t , A_p/A_t .
Mass Transfer	Defined by UDF, CO ₂ absorption in bulk liquid as per equation (6.12)
Multiphase Model	Eulerian two phase
Viscous Model	Standard $k-\varepsilon$ per phase
Drag Coefficient	Defined on constant terminal velocity, 20cm/s
Surface Tension	Constant: 0.0728 N/m
Pressure-Velocity coupling	Phase coupled SIMPLE
Discretization Scheme	QUICK except volume fraction, first order Upwind scheme for volume fraction
Transient formulation	First order implicit
Time Step	1×10^{-5} s
Grid Size (L×W×H)	Grid developed according to previous studies, Test case 1 = 80×12×300 cells.
Lift Coefficient (if applied)	Defined by Tomiyama relation (Tomiyama, 2004) (3.7)
Virtual mass force (if applied)	As defined in FLUENT theory guide (Fluent, 2009) (3.15).

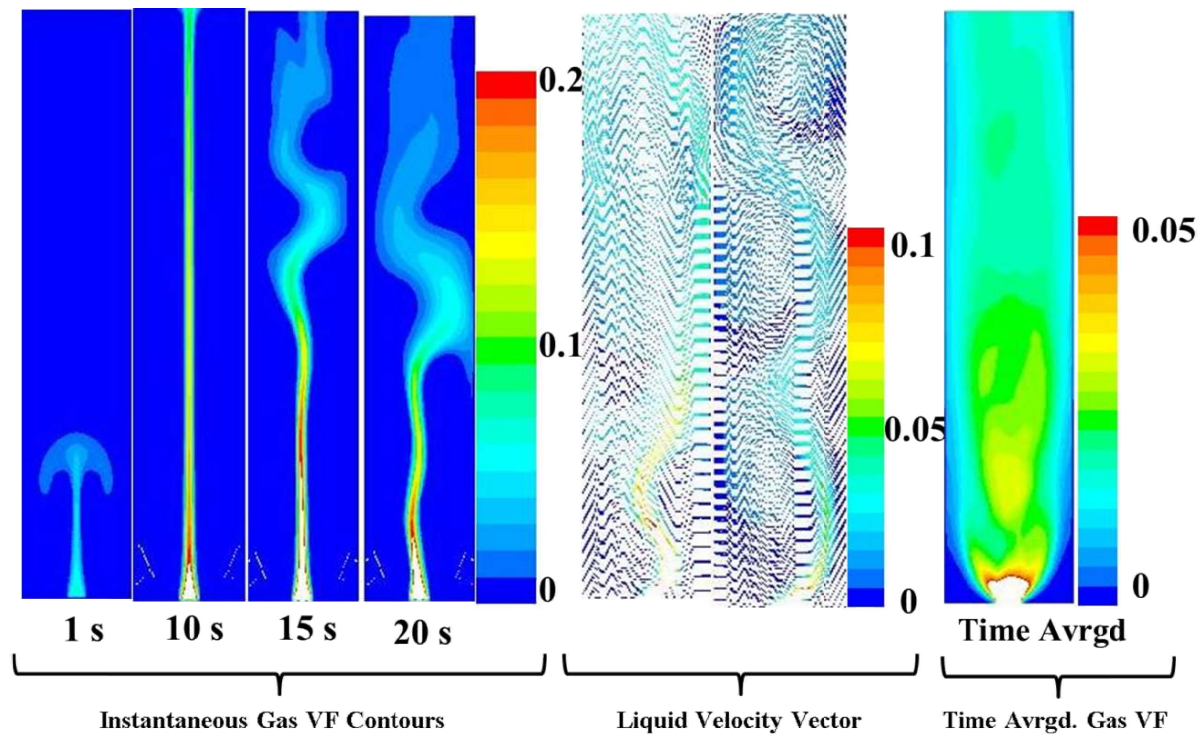


Figure 6.6a Instantaneous contours of CO_2 gas volume fraction and time is given in the bottom, liquid velocity vector with colour of gas volume fraction, on the left, the time averaged contours of CO_2 gas volume fraction for 80-220 s.

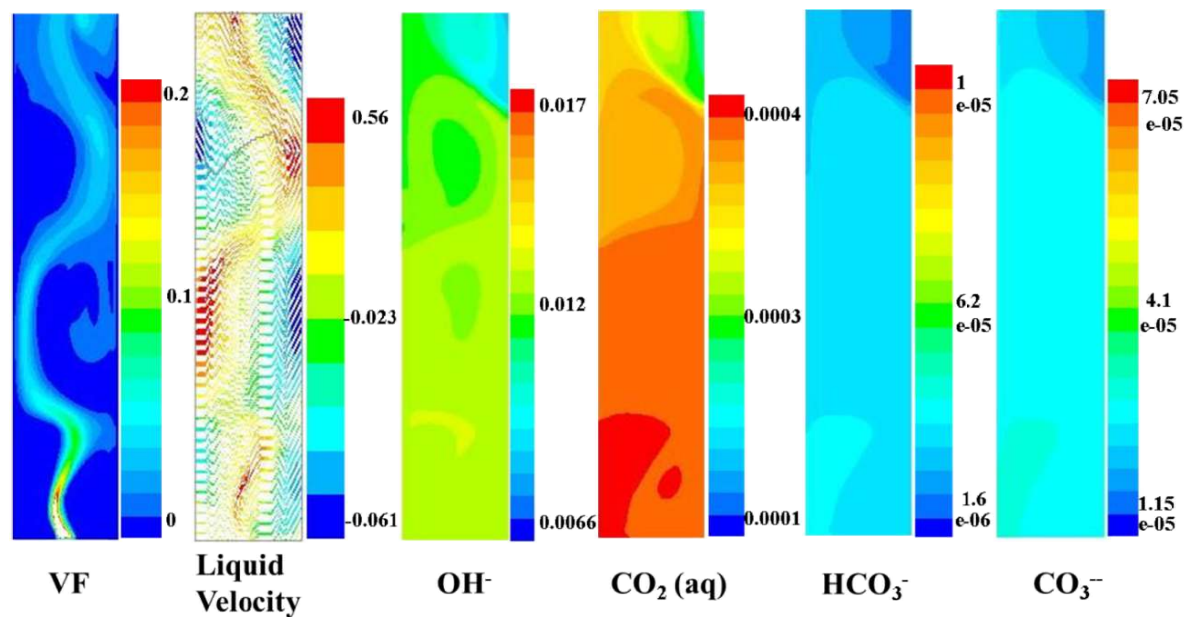


Figure 6.6b Instantaneous gas holdup contour, liquid velocity vector with colour of gas volume fraction and contours of species concentration in column.

The time history profiles of molar concentration of OH^- ion and pH of the liquid at point in column in central position and height of 0.95 m are shown in

Figure 6.7. The profile shows the rate of reaction of OH^- ion with absorbed CO_2 gas. The consumption rate of OH^- ion is linear with respect to time and the lower profile shows how the pH of the liquid changes with time at a point due to OH^- ion consumption, however these results of rate of OH^- ion consumption and pH of liquid are not as per expected. Further, improvement in these results and simulation of test case 3 are not included in this dissertation and are left for future work.

The time averaged liquid and bubbles velocities and gas holdup profiles are given in Figure 6.8 and 6.9, respectively. Gas bubbles velocity profile shows the higher upward motion of bubble in central region as compared to wall regions. The profile “Exp 1” is representing the experimental results without mass transfer and profile “Exp 2” representing the results with mass transfer. The results are in good agreement with the experimental results of bubbles velocity. The difference between bubbles velocity and liquid velocity is the slip velocity and is 0.2 m/s in our case as per their obtained profiles in Figure 6.8. The time averaged profile of liquid velocity is indicated the upward velocity in central region and downward velocity near the walls. The profile “Sim 1” is representing the simulation results without mass transfer and profile “Sim 2” representing the results with mass transfer. The averaged liquid velocity profile is in good agreement with simulation results of Darmana et al. (2007).

The time-averaged gas holdup profile is almost symmetric with larger values in the central region of the column as compared to near wall region. The profile is in good agreement with the averaged simulation results of Darmana et al. (2007).

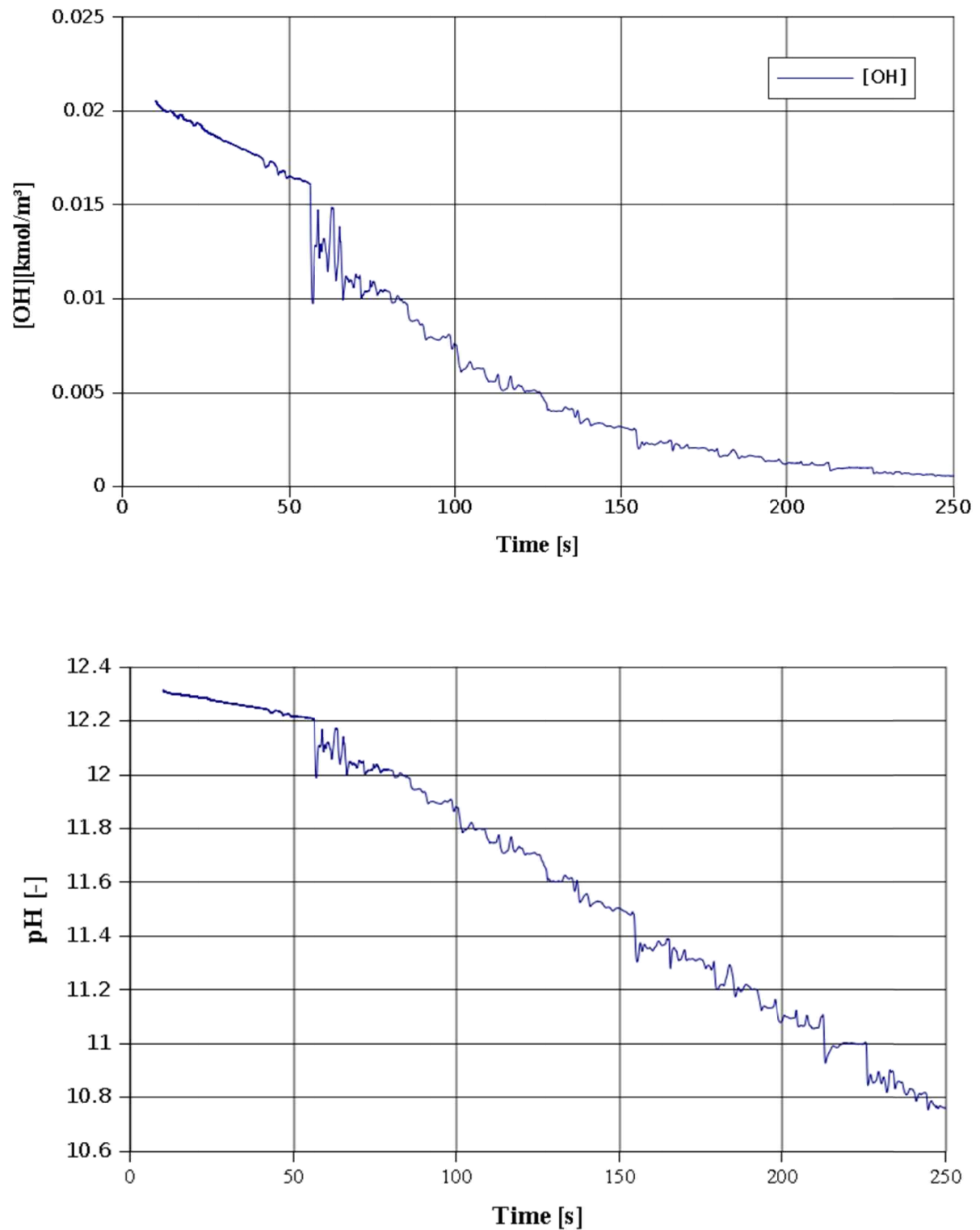


Figure 6.7 The time history evolution of OH ion molar concentration with time in BCR (upper part). The lower part is showing the evolution of pH of the liquid with consumption of OH ions.

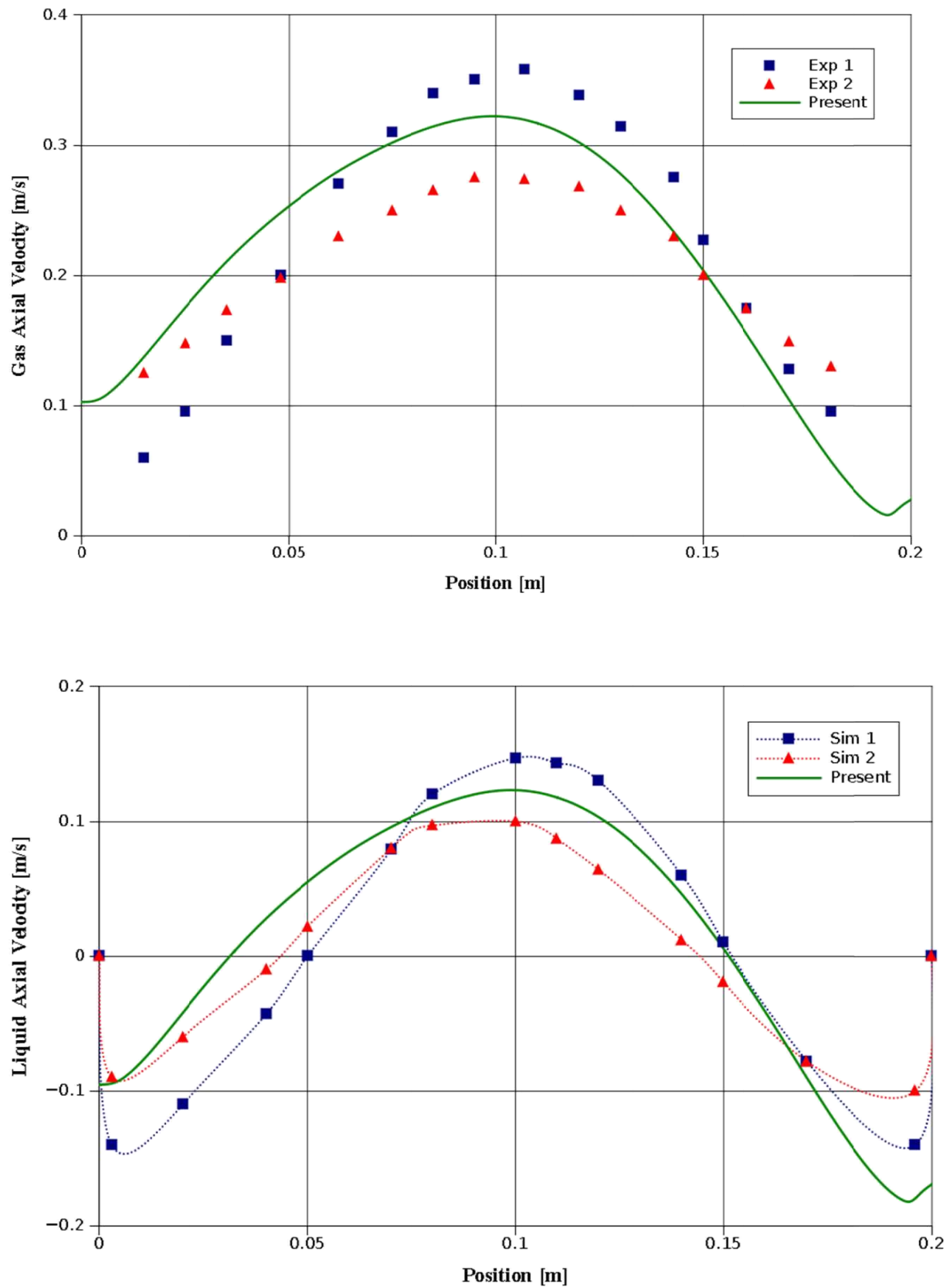


Figure 6.8 Time averaged gas bubbles and liquid velocities profile along the horizontal line at height 0.75 m from bottom. The experimental results, “Exp1” and “Exp 2” and simulation results “Sim 1” and “Sim 2” are taken from Darmana et al. (2007).

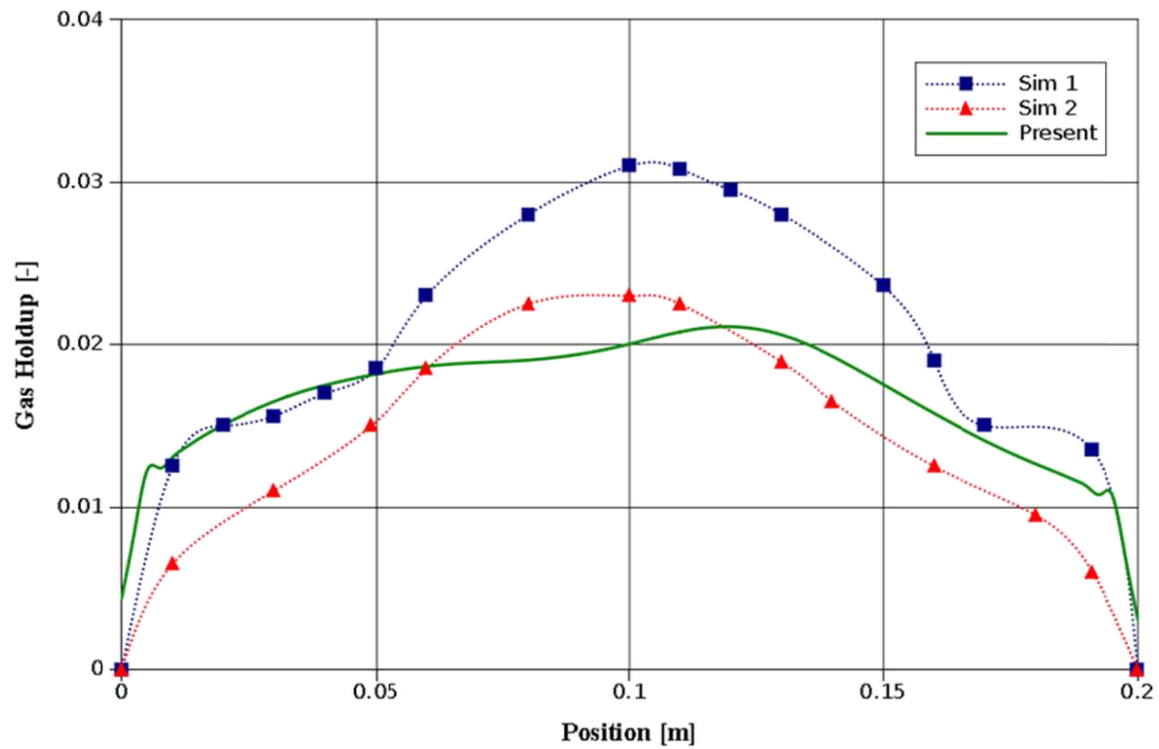


Figure 6.9 Time averaged gas holdup profile along the horizontal line at height 0.75 m from bottom. The simulation results “Sim 1” and “Sim 2” are taken from Darmana et al. (2007).

Chapter 7

Conclusions

Numerical simulations of bubble column reactors were presented in this dissertation starting from preliminary simulation aimed at identifying proper simulation parameters for a given system and resulting up to the numerical simulation with mass transfer and chemical reactions. In Chapter 2, an overview of the bubble column reactor, the probable flow regimes and different CFD methods are discussed. The generalized two fluid model (E-E) is described for gas liquid systems, beginning from the governing equations that are obtained from the local and instantaneous balance equations for each phase and then by implementing the averaging technique, consequently we got the general multifluid model. For the closure of the governing equations, interfacial forces and turbulence and their empirical correlations are presented.

Chapter 3 showed the simulation results after applying the methodology for numerical simulation of BCR by assuming a uniform bubble size. The results obtained for a system with low gas flow rate (48 L/h) indicated that we need enough fine mesh grid and appropriate closure of interfacial forces to predict reliably plume oscillation period, liquid axial velocity and gas holdup profiles. In the second section with high flow rate (260 L/h), we compared the results for the effect of different interfacial closure forces and change in inlet boundary condition for gas volume fraction. There was no change in results when there is change in gas volume fraction at inlet boundary condition. The effect of virtual mass interfacial force on the simulation results was also negligible. However, the major effects of applying lift force on results of plume oscillation period, liquid axial velocity and gas holdup was predicted. For comparable simulation results to experimental data, it was necessary to have enough fine grids and appropriate correlations for interfacial forces, especially the combination of drag and lift forces.

In Chapter 4, we discussed the population balance equation model (PBE) with main focus on gas-liquid systems, solution methods for PBE, and the quadrature methods of moments (QMOM) in detail. For modelling of bubble distributions

the number density function (NDF) was used which accounts for the bubble population.

The Chapter 5 presented the numerical simulation BCR with QMOM population balance technique for air-water fluid system. The work is divided in two sections; in the first section we carried out simulations with PBM using QMOM without breakage and coalescence phenomena to finalize the generic moments boundary conditions. In second section we simulated system with breakage and coalescence and eventually, the simulation results are compared with experimental and simulation data taken from the scientific literature. Our simulations results indicated that in case of just transportation of moments without breakage and coalescence of bubbles, the suitable boundary conditions for generic moments for QMOM is moments values at inlet defined as per with volume fraction correlation and at outlet as zero flux/value. However, as we have had observed also in the results of Chapter 3, the interfacial lift force with combination of drag force was necessary for better hydrodynamics results for QMOM. However the discretization scheme of first order upwind provided the expected results of uniform bubble size with the finalized boundary conditions. The simulation result of QMOM with breakage and coalescence models were also in good agreement with hydrodynamics experimental results and for bubble size distribution results, simulation results of class methods and DQMOM.

In Chapter 6, we modelled the reactive absorption of pure CO₂ gas in caustic solution in a rectangular BCR with the simulation parameters settings identified in previous chapters. For applicability of available kinetic and physical data we developed concentration differential equation and estimation of the species concentration with respect to time in MATLAB code. The obtained profiles of evaluation of concentration and pH were in similar fashion as compared to available simulated concentration and pH profiles at a point in the bubble column with respect to time. Consequently we can say that the available kinetics and physical data is applicable to predict the chemical evaluation for further numerical simulations. CFD simulation taking into account the mass transfer and chemical reaction, the E-E approach is used with assumption of uniform bubble size for modelling of chemisorption of the CO₂ gas bubbles into NaOH aqueous solution. The adopted model successfully predicted the hydrodynamics of bubble column reactor and results are in good agreement with experimental and simulation results, however, reaction processes results

were not as per expectation. The improvements in the results of reaction processes are not included in this dissertation and are left for future work.

References

- Alopaeus, V., Koskinen, J., Keskinen, K., and Majander, J. (2002). Simulation of the population balances for liquid–liquid systems in a nonideal stirred tank. part 2-- parameter fitting and the use of the multiblock model for dense dispersions. *Chemical Engineering Science*, 57(10):1815–1825.
- AN, C. M.-B. (1999). On the breakup of an air bubble injected into a fully developed turbulent flow. part 1. breakup frequency. *J. Fluid Mech*, 401:157–182.
- Aris, R. (1962). Vectors, tensors and the basic equations of fluid dynamics. *Englewood Cliffs, J. Prentice–Hall*.
- Auton, T. (1987). The lift force on a spherical body in a rotational flow. *J. Fluid Mech*, 183:199–218.
- Bauer, M. and Eigenberger, G. (1999). A concept for multi-scale modeling of bubble columns and loop reactors. *Chemical Engineering Science*, 54(21):5109–5117.
- Behzadi, A., Issa, R., and Rusche, H. (2004). Modelling of dispersed bubble and droplet flow at high phase fractions. *Chemical Engineering Science*, 59(4):759–770.
- Bertola, F., Vanni, M. & Baldi, G. (2002). Application of computational fluid dynamics to multiphase flow in bubble columns. *International Journal of Chemical Reactor Engineering*, 1(1):1–13.
- Biesheuvel, A. and Spoelstra, S. (1989). The added mass coefficient of a dispersion of spherical gas bubbles in liquid. *International Journal of Multiphase Flow*, 15(6):911–924.
- Bird, R. B., Stewart, W. E., & Lightfoot, E. N. (2002). Transport phenomena. *JohnWiley & Sons, New York USA*. second edition.

- Bouaifi, M., Hebrard, G., Bastoul, D., and Roustan, M. (2001). A comparative study of gas hold-up, bubble size, interfacial area and mass transfer coefficients in stirred gas–liquid reactors and bubble columns. *Chemical Engineering and Processing: Process Intensification*, 40(2):97–111.
- Bruce Stewart, H. and Wendroff, B. (1984). Two-phase flow: models and methods. *Journal of Computational Physics*, 56(3):363–409.
- Buffo, A. (2012). *Multivariate population balance for turbulent gas-liquid flows*. PhD thesis, Politecnico di Torino.
- Buwa, V. V., Deo, D. S., and Ranade, V. V. (2006). Eulerian–Lagrangian simulations of unsteady gas–liquid flows in bubble columns. *International Journal of Multiphase Flow*, 32(7):864–885.
- Buwa, V. V. and Ranade, V. V. (2002). Dynamics of gas–liquid flow in a rectangular bubble column: experiments and single/multi-group cfd simulations. *Chemical Engineering Science*, 57(22):4715–4736.
- Chen, C. and Fan, L.-S. (2004). Discrete simulation of gas-liquid bubble columns and gas-liquid-solid fluidized beds. *AIChE journal*, 50(2):288–301.
- Chen, P. (2004). *Modeling the fluid dynamics of bubble column flows*. PhD thesis, Washington University, 2004. Department of Chemical Engineering.
- Chen, P., Sanyal, J., and Dudukovic, M. (2005). Numerical simulation of bubble columns flows: effect of different breakup and coalescence closures. *Chemical Engineering Science*, 60(4):1085–1101.
- Clift, R., Grace, J., and Weber, M. (1978). Bubbles. *Drops and Particles (Academic, New York, 1978)*, page 1870.
- Coulaloglou, C. and Tavlarides, L. (1977). Description of interaction processes in agitated liquid-liquid dispersions. *Chemical Engineering Science*, 32(11):1289–1297.
- Crowe, C., Troutt, T., and Chung, J. (1996). Numerical models for two-phase turbulent flows. *Annual Review of Fluid Mechanics*, 28(1):11–43.
- Crowe, C. T., Stock, D., and Sharma, M. (1977). The particle-source-in cell/psi-cell/model for gas-droplet flows. *ASME Transactions Journal of Fluids Engineering*, 99:325–332.

- Darmana, D. (2006). *On the multiscale modelling of hydrodynamics, mass transfer and chemical reactions in bubble columns*. University of Twente.
- Darmana, D., Deen, N., and Kuipers, J. (2005). Detailed modeling of hydrodynamics, mass transfer and chemical reactions in a bubble column using a discrete bubble model. *Chemical Engineering Science*, 60(12):3383–3404.
- Darmana, D., Henket, R., Deen, N., and Kuipers, J. (2007). Detailed modelling of hydrodynamics, mass transfer and chemical reactions in a bubble column using a discrete bubble model: Chemisorption of CO₂ into NaOH solution, numerical and experimental study. *Chemical engineering science*, 62(9):2556–2575.
- Deckwer, W.-D. and Field, R. W. (1992). *Bubble column reactors*, volume 200. Wiley Chichester.
- Deen, N., Mudde, R., Kuipers, J., Zehner, P., and Kraume, M. (2010). Bubble columns. *Ullmann's Encyclopedia of Industrial Chemistry*.
- Deen, N. G., Solberg, T., and Hjertager, B. H. (2001). Large eddy simulation of the gas–liquid flow in a square cross-sectioned bubble column. *Chemical Engineering Science*, 56(21):6341–6349.
- Delnoij, E., Kuipers, J., and Van Swaaij, W. (1999). A three-dimensional cfd model for gas–liquid bubble columns. *Chemical Engineering Science*, 54(13):2217–2226.
- Delnoij, E., Lammers, F., Kuipers, J., and Van Swaaij, W. M.(1997). Dynamic simulation of dispersed gas–liquid two-phase ow using a discrete bubble model. *Chemical Engineering Science*, 52:1429–1458.
- Delnoij, E., Lammers, F., Kuipers, J., and Van Swaaij, W. (1997). Dynamic simulation of dispersed gas-liquid two-phase flow using a discrete bubble model. *Chemical Engineering Science*, 52(9):1429–1458.
- Derksen, J. and Van den Akker, H. E. (1999). Large eddy simulations on the flow driven by a rushton turbine. *AIChE Journal*, 45(2):209–221.
- Devanathan, N., Dudukovic, M., Lapin, A., and Lübbert, A. (1995). Chaotic flow in bubble column reactors. *Chemical Engineering Science*, 50(16):2661–2667.

- Dhotre, M. and Joshi, J. (2004). Two-dimensional CFD model for the prediction of flow pattern, pressure drop and heat transfer coefficient in bubble column reactors. *Chemical engineering research and design*, 82(6):689–707.
- Diáz, M. E., Iranzo, A., Cuadra, D., Barbero, R., Montes, F. J., and Galán, M. A. (2008). Numerical simulation of the gas–liquid flow in a laboratory scale bubble column: influence of bubble size distribution and non-drag forces. *Chemical Engineering Journal*, 139(2):363–379.
- Drew, D. and Lahey, R. (1987). The virtual mass and lift force on a sphere in rotating and straining inviscid flow. *International Journal of Multiphase Flow*, 13(1):113–121.
- Drew, D. A. and Passman, S. L. (1999). *Theory of multicomponent fluids*, volume 135. Springer.
- Enwald, H., Peirano, E., and Almstedt, A.-E. (1996). Eulerian two-phase flow theory applied to fluidization. *International Journal of Multiphase Flow*, 22:21–66.
- Fluent, A. (2009). 12.0 theory guide. *Ansys Inc*, 5.
- Fregapane, G., Rubio-Fernández, H., Nieto, J., and Salvador, M. (1999). Wine vinegar production using a noncommercial 100-litre bubble column reactor equipped with a novel type of dynamic sparger. *Biotechnology and bioengineering*, 63(2):141–146.
- Gautschi, W., FRIEDMAN, R. S., BURNS, J., DARJEE, R., and MCINTOSH, A. (2004). *Orthogonal Polynomials: Computation and Approximation, Numerical Mathematics and Scientific Computation Series*. Oxford University Press, Oxford.
- Geary, N. W. and Rice, R. G. (1991). Bubble size prediction for rigid and flexible spargers. *AIChE journal*, 37(2):161–168.
- Godin, F. B., Cooper, D. G., and Rey, A. D. (1999). Numerical methods for a population-balance model of a periodic fermentation process. *AIChE journal*, 45(6):1359–1364.
- Gordon, R. G. (1968). Error bounds in equilibrium statistical mechanics. *Journal of Mathematical Physics*, 9(5):655–663.

- Gunawan, R., Fusman, I., and Braatz, R. D. (2004). High resolution algorithms for multidimensional population balance equations. *AIChE Journal*, 50(11):2738–2749.
- Gupta, A. and Roy, S. (2012). Euler-Euler simulation of bubbly flow in a rectangular bubble column: Experimental validation with radioactive particle tracking. *Chemical Engineering Journal*.
- Haberman, W. L. and Morton, R. K. (1956). An experimental study of bubbles moving in liquids. *Transactions of the American Society of Civil Engineers*, 121(1):227–250.
- Hartmann, H., Derksen, J., Montavon, C., Pearson, J., Hamill, I., and Van den Akker, H. (2004). Assessment of large eddy and rans stirred tank simulations by means of lda. *Chemical Engineering Science*, 59(12):2419–2432.
- Hesketh, R. P., Etchells, A. W., and Russell, T. F. (1991). Experimental observations of bubble breakage in turbulent flow. *Industrial & Engineering Chemistry Research*, 30(5):835–841.
- Hibiki, T. and Ishii, M. (2007). Lift force in bubbly flow systems. *Chemical Engineering Science*, 62(22):6457–6474.
- Hills, J. (1976). The operation of a bubble column at high throughputs: I. gas holdup measurements. *The Chemical Engineering Journal*, 12(2):89–99.
- Hirt, C. W. and Nichols, B. D. (1981). Volume of fluid (vof) method for the dynamics of free boundaries. *Journal of computational physics*, 39(1):201–225.
- Hjertager, B. H. (2007). Multi-fluid CFD analysis of chemical reactors. In *Multiphase Reacting Flows: Modelling and Simulation*, pages 125–179. Springer.
- Hulburt, H. and Katz, S. (1964). Some problems in particle technology: A statistical mechanical formulation. *Chemical Engineering Science*, 19(8):555–574.
- Hunt, J., Auton, T., Sene, K., Thomas, N., and Kowe, R. (1987). Ichmt international seminar on transient phenomena in multiphase flow. In *Dubrovnik, Yugoslavia*, pages 103–125.

- Hyndman, C. L., Larachi, F., and Guy, C. (1997). Understanding gas-phase hydrodynamics in bubble columns: a convective model based on kinetic theory. *Chemical engineering science*, 52(1):63–77.
- Ishii, M. (1975). Thermo-fluid dynamic theory of two-phase flow. *NASA STI/Recon Technical Report A*, 75:29657.
- Ishii, M. and Mishima, K. (1984). Two-fluid model and hydrodynamic constitutive relations. *Nuclear Engineering and design*, 82(2):107–126.
- Ishii, M. and Zuber, N. (1979). Drag coefficient and relative velocity in bubbly, droplet or particulate flows. *AIChE Journal*, 25(5):843–855.
- Jakobsen, H. A. (2008). *Chemical reactor modeling: multiphase reactive flows*. Springer.
- Johansen, S. and Boysan, F. (1988). Fluid dynamics in bubble stirred ladles: Part ii. mathematical modeling. *Metallurgical Transactions B*, 19(5):755–764.
- Joshi, J. (2001). Computational flow modelling and design of bubble column reactors. *Chemical Engineering Science*, 56(21):5893–5933.
- Kataoka, I. and Serizawa, A. (1989). Basic equations of turbulence in gas-liquid two-phase flow. *International Journal of Multiphase Flow*, 15(5):843–855.
- Kostoglou, M. and Karabelas, A. (1994). Evaluation of zero order methods for simulating particle coagulation. *Journal of colloid and interface science*, 163(2):420–431.
- Krishna, R. and Ellenberger, J. (1996). Gas holdup in bubble column reactors operating in the churn-turbulent flow regime. *AIChE journal*, 42(9):2627–2634.
- Krishna, R. and Van Baten, J. (1999). Simulating the motion of gas bubbles in a liquid. *Nature*, 398(6724):208–208.
- Krishna, R. and Van Baten, J. (2001). Eulerian simulations of bubble columns operating at elevated pressures in the churn turbulent flow regime. *Chemical engineering science*, 56(21):6249–6258.
- Kuipers, J. and Van Swaaij, W. (1997). Application of computational fluid dynamics to chemical reaction engineering. *Reviews in Chemical Engineering*, 13(3):1–118.

- Kumar, J., Peglow, M., Warnecke, G., and Heinrich, S. (2008). The cell average technique for solving multi-dimensional aggregation population balance equations. *Computers & Chemical Engineering*, 32(8):1810–1830.
- Laakkonen, M., Alopaeus, V., and Aittamaa, J. (2006). Validation of bubble breakage, coalescence and mass transfer models for gas–liquid dispersion in agitated vessel. *Chemical engineering science*, 61(1):218–228.
- Laakkonen, M., Moilanen, P., Alopaeus, V., and Aittamaa, J. (2007). Modelling local bubble size distributions in agitated vessels. *Chemical Engineering Science*, 62(3):721–740.
- Lain, S., Bröder, D., and Sommerfeld, M. (1999). Experimental and numerical studies of the hydrodynamics in a bubble column. *Chemical Engineering Science*, 54(21):4913–4920.
- Lapin, A. and Lübbert, A. (1994). Numerical simulation of the dynamics of two-phase gas-liquid flows in bubble columns. *Chemical Engineering Science*, 49(21):3661–3674.
- Lauder, B. E., Rodi, W., Launder, B. E., Reynolds, W. C., and Rodi, W. (1984). *Turbulence models and their applications*. Editions Eyrolles.
- Lauder, B. E. and Spalding, D. (1974). The numerical computation of turbulent flows. *Computer methods in applied mechanics and engineering*, 3(2):269–289.
- Lee, C.-H., Erickson, L., and Glasgow, L. (1987a). Bubble breakup and coalescence in turbulent gas-liquid dispersions. *Chemical Engineering Communications*, 59(1-6):65–84.
- Lee, C.-H., Erickson, L., and Glasgow, L. (1987b). Dynamics of bubble size distribution in turbulent gas-liquid dispersions. *Chemical Engineering Communications*, 61(1-6):181–195.
- Lehr, F. and Mewes, D. (2001). A transport equation for the interfacial area density applied to bubble columns. *Chemical Engineering Science*, 56(3):1159–1166.
- Lehr, F., Millies, M., and Mewes, D. (2002). Bubble-size distributions and flow fields in bubble columns. *AIChE Journal*, 48(11):2426–2443.

- Li, Y., Zhang, J., and Fan, L.-S. (1999). Numerical simulation of gas–liquid–solid fluidization systems using a combined CFD-VOF-DPM method: bubble wake behavior. *Chemical Engineering Science*, 54(21):5101–5107.
- Lopez de Bertodano, M. A. and Saif, A. A. (1997). Modified k - ϵ model for two-phase turbulent jets. *Nuclear engineering and design*, 172(1):187–196.
- Luo, H. and Svendsen, H. F. (1996). Theoretical model for drop and bubble breakup in turbulent dispersions. *AIChE Journal*, 42(5):1225–1233.
- Marchisio, D. L. and Fox, R. O. (2005). Solution of population balance equations using the direct quadrature method of moments. *Journal of Aerosol Science*, 36(1):43–73.
- Marchisio, D. L. and Fox, R. O. (2013). *Computational Models for Polydisperse Particulate and Multiphase Systems*. Cambridge University Press.
- Marchisio, D. L., Vigil, R. D., and Fox, R. O. (2003a). Quadrature method of moments for aggregation–breakage processes. *Journal of Colloid and Interface Science*, 258(2):322–334.
- Marchisio, D. L., Dennis Vigil, R., and O Fox, R. (2003b). Implementation of the quadrature method of moments in CFD codes for aggregation–breakage problems. *Chemical Engineering Science*, 58(15):3337–3351.
- McGraw, R. (1997). Description of aerosol dynamics by the quadrature method of moments. *Aerosol Science and Technology*, 27(2):255–265.
- Mewes, D. and Wiemann, D. (2003). Two-phase flow with mass transfer in bubble columns. *Chemical engineering & technology*, 26(8):862–868.
- Migdal, D. and Agosta, V. (1967). A source flow model for continuum gas-particle flow. *Journal of Applied Mechanics*, 34:860.
- Miller, D. N. (1980). Gas holdup and pressure drop in bubble column reactors. *Industrial & Engineering Chemistry Process Design and Development*, 19(3):371–377.
- Molerus, O. (1980). A coherent representation of pressure drop in fixed beds and of bed expansion for particulate fluidized beds. *Chemical Engineering Science*, 35(6):1331–1340.

- Mudde, R. F. and Simonin, O. (1999). Two-and three-dimensional simulations of a bubble plume using a two-fluid model. *Chemical Engineering Science*, 54(21):5061–5069.
- Nambiar, D., Kumar, R., Das, T., and Gandhi, K. (1992). A new model for the breakage frequency of drops in turbulent stirred dispersions. *Chemical engineering science*, 47(12):2989–3002.
- Nandanwar, M. N. and Kumar, S. (2008). A new discretization of space for the solution of multi-dimensional population balance equations. *Chemical Engineering Science*, 63(8):2198–2210.
- Narsimhan, G., Gupta, J., and Ramkrishna, D. (1979). A model for transitional breakage probability of droplets in agitated lean liquid-liquid dispersions. *Chemical Engineering Science*, 34(2):257–265.
- Nigar, K., Borak, F., and Ulgen, K. (2005). Bubble column reactors. *Process biochemistry*, 40(7):2263–2283.
- Patruno, L., Dorao, C., Svendsen, H., and Jakobsen, H. (2009). Analysis of breakage kernels for population balance modelling. *Chemical Engineering Science*, 64(3):501–508.
- Peebles, F. N. and Garber, H. J. (1953). Studies on the motion of gas bubbles in liquids. *Chem. Eng. Prog*, 49(2):88–97.
- Petitti, M., Nasuti, A., Marchisio, D. L., Vanni, M., Baldi, G., Mancini, N., and Podenzani, F. (2010). Bubble size distribution modeling in stirred gas–liquid reactors with qmom augmented by a new correction algorithm. *AIChE Journal*, 56(1):36–53.
- Pfleger, D. and Becker, S. (2001). Modelling and simulation of the dynamic flow behaviour in a bubble column. *Chemical Engineering Science*, 56(4):1737–1747.
- Pfleger, D., Gomes, S., Gilbert, N., and Wagner, H.-G. (1999). Hydrodynamic simulations of laboratory scale bubble columns fundamental studies of the eulerian–eulerian modelling approach. *Chemical Engineering Science*, 54(21):5091–5099.

Picart, A., Berlemont, A., Gouesbet, G., and Barrère, M. (1982). *De l'influence du terme de Basset sur la dispersion de particules discrètes dans le cadre de la théorie de Tchen*. Gauthier-Villars.

Pino, L., Solari, R., Siquier, S., Antonio Estevez, L., Yopez, M., and Saez, A. (1992). Effect of operating conditions on gas holdup in slurry bubble columns with a foaming liquid. *Chemical Engineering Communications*, 117(1):367–382.

Press, W. H. (2007). *Numerical recipes 3rd edition: The art of scientific computing*. Cambridge university press.

Prince, M. J. and Blanch, H. W. (1990). Bubble coalescence and break-up in air-sparged bubble columns. *AIChE Journal*, 36(10):1485–1499.

Ramkrishna, D. (2000). *Population balances: Theory and applications to particulate systems in engineering*. Access Online via Elsevier.

Ranade, V. V. (2002). *Computational flow modelling for chemical reactor engineering*. Academic Press.

Ratcliff, G. and Holdcroft, J. (1963). Diffusivities of gases in aqueous electrolyte solutions. *Trans. Inst. Chem. Eng*, 41:315–319.

Rigopoulos, S. and Jones, A. (2003). A hybrid CFD reaction engineering framework for multiphase reactor modelling: basic concept and application to bubble column reactors. *Chemical Engineering Science*, 58(14):3077–3089.

Sato, Y. and Sekoguchi, K. (1975). Liquid velocity distribution in two-phase bubble flow. *International Journal of Multiphase Flow*, 2(1):79–95.

Schiller, L. and Naumann, A. (1935). A drag coefficient correlation. *Vdi Zeitung*, 77:318–320.

Schumpe, A. and Grund, G. (1986). The gas disengagement technique for studying gas holdup structure in bubble columns. *The Canadian Journal of Chemical Engineering*, 64(6):891–896.

Selma, B., Bannari, R., and Proulx, P. (2010). Simulation of bubbly flows: Comparison between direct quadrature method of moments (DQMOM) and method of classes (CM). *Chemical Engineering Science*, 65(6):1925–1941.

- Shah, Y., Kelkar, B. G., Godbole, S., and Deckwer, W.-D. (1982). Design parameters estimations for bubble column reactors. *AIChE Journal*, 28(3):353–379.
- Shaikh, A. and Al-Dahhan, M. H. (2007). A review on flow regime transition in bubble columns. *International Journal of Chemical Reactor Engineering*, 5(1).
- Simonnet, M., Gentric, C., Olmos, E., and Midoux, N. (2007). Experimental determination of the drag coefficient in a swarm of bubbles. *Chemical Engineering Science*, 62(3):858–866.
- Sokolichin, A. and Eigenberger, G. (1994). Gas–liquid flow in bubble columns and loop reactors: Part i. detailed modelling and numerical simulation. *Chemical Engineering Science*, 49(24):5735–5746.
- Sokolichin, A. and Eigenberger, G. (1999). Applicability of the standard $k-\epsilon$ turbulence model to the dynamic simulation of bubble columns: Part i. detailed numerical simulations. *Chemical Engineering Science*, 54(13):2273–2284.
- Sokolichin, A., Eigenberger, G., and Lapin, A. (2004). Simulation of buoyancy driven bubbly flow: established simplifications and open questions. *AIChE Journal*, 50(1):24–45.
- Tabib, M. V., Roy, S. A., and Joshi, J. B. (2008). Cfd simulation of bubble column—analysis of interphase forces and turbulence models. *Chemical Engineering Journal*, 139(3):589–614.
- Thakre, S. and Joshi, J. (1999). CFD simulation of bubble column reactors: importance of drag force formulation. *Chemical Engineering Science*, 54(21):5055–5060.
- Tomiyama, A. (2004). Drag, lift and virtual mass force acting on a single bubble. In *3rd International Symposium on Two-Phase Flow Modelling and Experimentation, 2004*.
- Tomiyama, A., Kataoka, I., Zun, I., and Sakaguchi, T. (1998). Drag coefficients of single bubbles under normal and micro gravity conditions. *JSME international journal. Series B, fluids and thermal engineering*, 41(2):472–479.
- Tomiyama, A., Tamai, H., Zun, I., and Hosokawa, S. (2002). Transverse migration of single bubbles in simple shear flows. *Chemical Engineering Science*, 57(11):1849–1858.

- Tsuji, Y., Morikawa, Y., and Shiomi, H. (1984). LDV measurements of an air-solid two-phase flow in a vertical pipe. *J. Fluid Mech*, 139:417–434.
- Van Sint Annaland, M., Deen, N., and Kuipers, J. (2005). Numerical simulation of gas–liquid–solid flows using a combined front tracking and discrete particle method. *Chemical engineering science*, 60(22):6188–6198.
- Van Wachem, B. and Almstedt, A.-E. (2003). Methods for multiphase computational fluid dynamics. *Chemical Engineering Journal*, 96(1):81–98.
- Van Wijngaarden, L. (1976). Hydrodynamic interaction between gas bubbles in liquid. *J. Fluid Mech*, 77(1):27–44.
- Vanni, M. (2000). Approximate population balance equations for aggregation–breakage processes. *Journal of Colloid and Interface Science*, 221(2):143–160.
- Versteeg, G. F. and Van Swaalj, W. (1988). Solubility and diffusivity of acid gases (carbon dioxide, nitrous oxide) in aqueous alkanolamine solutions. *Journal of Chemical and Engineering Data*, 33(1):29–34.
- Weisenberger, S. and Schumpe, A. (1996). Estimation of gas solubilities in salt solutions at temperatures from 273 k to 363 k. *AIChE Journal*, 42(1):298–300.
- Westerterp, K. R., Van Swaaij, W., Beenackers, A., and Kramers, H. (1984). *Chemical reactor design and operation*.
- Wheeler, J. C. (1974). Modified moments and gaussian quadratures. *Rocky Mountain Journal of Mathematics*, 4(2):287–296.
- Wilf, H. (2011). *Mathematics for the physical sciences*. DoverPublications.com.
- Yeoh, G. H. and Tu, J. (2009). *Computational techniques for multiphase flows*. Access Online via Elsevier.
- Zhang, D. (2007). *Eulerian modeling of reactive gas-liquid flow in a bubble column*. University of Twente.
- Zhang, D., Deen, N., and Kuipers, J. (2006). Numerical simulation of the dynamic flow behavior in a bubble column: a study of closures for turbulence and interface forces. *Chemical Engineering Science*, 61(23):7593–7608.

Zhao, H., Maisels, A., Matsoukas, T., and Zheng, C. (2007). Analysis of four monte carlo methods for the solution of population balances in dispersed systems. *Powder technology*, 173(1):38–50.

Zucca, A., Marchisio, D. L., Vanni, M., and Barresi, A. A. (2007). Validation of bivariate DQMOM for nanoparticle processes simulation. *AIChE journal*, 53(4):918–931.

Zun, I. (1980). The transverse migration of bubbles influenced by walls in vertical bubbly flow. *International Journal of Multiphase Flow*, 6(6):583–588.

Acknowledgement

With the name of Almighty Allah and His countless blessings on us, I would like to express my sincere gratitude to my main supervisor, Prof. Marco Vanni for his special guidance and discussions on the work, great patience during the transition phases for awaiting the outcome of research work and making my last four years memorable and fruitful in Politecnico di Torino.

A special thanks to my second supervisor Prof. Daniele Marchisio for analysing my work and advising me in presenting better results of work. In addition to my supervising professors, I would like to thank my senior colleague, Dr. Antonio Buffo, for discussions, guidance in research and helping me in adjusting in Torino and university. I would like to extend my thanks to the PhD coordinator, Prof. Vito Specchia, staff of DISAT and other university persons who helped me in research and made my time comfortable in Torino.

I would like to express my appreciations to a lot of friends (especially, Muntazir) who facilitated me during my stay in Torino. Grateful to my eldest brother Munim, he is always ready to support me and my other brothers, Usman, Kamran and Zishan, for their love and efforts in resolving different matters on my behalf. My cousin and friend, Junaid assisted me a lot especially in initial days with boarding and lodging in Torino.

I am thankful to Higher Education Commission of Pakistan (HEC) for their economic support for the research work.

Very special thanks to my family. Words only cannot express explicitly how grateful I am to my mother, father, mother-in-law and father-in-law, for all of their hardships bearing on my behalf. You have always been a steadfast source of encouragement and determination for me.

At the end I would like to assert my gratefulness to my beloved wife Maria Khurram, standing with me and is always my firm source of encouragement in the tough moments when there is no one to help me out.

In the love of my family, I would like to dedicate my work to my parents and wife.

Khurram Imran Khan
January, 2014, Torino

اظہارِ تشکر

تحقیقاتی کام کی منظوری کے اعتراف میں

شروع ذاتِ باری تعالیٰ کے نام سے، میں نے جو تحقیقاتی کام کیا ہے اس کے لیے میں اپنے پروفیسر مارکو وانی کا تہیٰ دل سے شکریہ ادا کرتا ہوں، انہوں نے اس کام کو جس طریقے سے مجھے سمجھایا اور لگاتار محنت کے ساتھ جس نہج تک پہنچایا، وہ اپنے اندر ایک مثال ہے۔

میں ہائر ایجوکیشن کمیشن پاکستان کا شکریہ ادا کرنا چاہوں گا جنہوں نے مجھ پر اعتماد کرتے ہوئے تعلیمی وظیفہ سے نوازا اور بھرپور طریقے سے ہر لحاظ سے مدد کی۔

تحقیقاتی کام کے مکمل ہونے میں میرے والدین تعریف کے مستحق ہیں جن کی گوناگوں خداداد صلاحیتوں کی بدولت میں اس پائے تک پہنچا، اور اس کے ساتھ اس کام کی تکمیل میں میری بیگم ماریہ کا بھی ایک بڑا حصہ ہے، جس نے بڑی خندہ پیشانی سے اس کام میں میرا ہر دم ساتھ دیا۔

اللہ تعالیٰ سے دعا ہے کہ وہ مجھے ایسے ہی کامیابیوں سے نوازتا رہے، آمین۔

خرم عمران خان

جنوری ۲۰۱۴ء، تورینو، اٹلی۔

THE END